Effects of Compressibility, Pitch Rate and Reynolds Number on Unsteady Incipient Leading-Edge Boundary Layer Separation Over a Pitching Airfoil

Final Report (RU-TR-MAE-190-F)

Prof. D. D. Knight and P. Ghosh Choudhuri and N. Okong'o

April 1996

U. S. Army Research Office

ARO Grant DAAL03-91-G-0096

Department of Mechanical and Aerospace Engineering

Rutgers, The State University of New Jersey

DISCLAIMER NOTICE

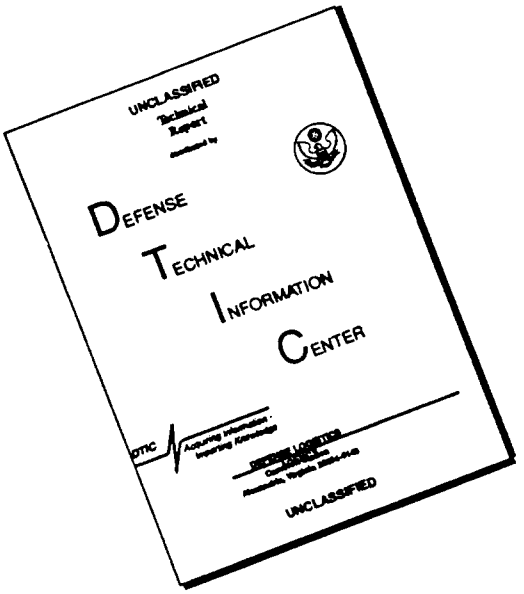

THIS DOCUMENT IS BEST QUALITY AVAILABLE. THE COPY FURNISHED TO DTIC CONTAINED A SIGNIFICANT NUMBER OF PAGES WHICH DO NOT REPRODUCE LEGIBLY.

REPORT DOCUMENTATION PAGE

Form Approved
OMB No. 0704-0188

1. AGENCY USE ONLY (Leave blank)	2. REPORT DATE	3. REPORT TYPE AND DATES COVERED
	30 Apr 96	Final; 1 April '91-30 March '96

4. TITLE AND SUBTITLE
Effects of Compressibility, Pitch Rate and Reynolds Number on Unsteady Incipient Leading-Edge Boundary Layer Separation Over a Pitching Airfoil.

5. FUNDING NUMBERS
Grant Number
DAAL03-91-G-0096

6. AUTHOR(S)
Professor Doyle D. Knight
Pushkar Ghosh Choudhuri, Nora Okong'o

7. PERFORMING ORGANIZATION NAME(S) AND ADDRESS(ES)
Department of Mechanical and Aerospace Engineering
Rutgers, The State University of New Jersey
P.O. Box 909,
Piscataway, NJ 08855-0909

8. PERFORMING ORGANIZATION REPORT NUMBER

9. SPONSORING/MONITORING AGENCY NAME(S) AND ADDRESS(ES)
U. S. Army Research Office
P. O. Box 12211
Research Triangle Park, NC 27709-2211

10. SPONSORING/MONITORING AGENCY REPORT NUMBER
ARO 28651.9-EG

11. SUPPLEMENTARY NOTES
The view, opinions and/or findings contained in this report are those of the author(s) and should not be construed as an official Department of the Army position, policy, or decision, unless so designated by other documentation.

12a. DISTRIBUTION/AVAILABILITY STATEMENT
Approved for public release; distribution unlimited.

12b. DISTRIBUTION CODE

13. ABSTRACT (Maximum 200 words)
The effects of compressibility, pitch rate and Reynolds number on the initial stages of 2-D unsteady separation of laminar subsonic flow over a pitching NACA-0012 airfoil have been studied numerically. Computations have been performed using two separate algorithms (structured grid algorithm of Beam and Warming, and unstructured grid algorithm employing flux-difference splitting method of Roe) for the compressible laminar Navier-Stokes equations. The simulations show the appearance of a primary recirculating region near the leading edge, followed by a secondary and tertiary recirculating regions. The primary and secondary recirculating regions interact with each other to give rise to the unsteady separation of the boundary layer. Increasing the Mach number from 0.2 to 0,5 causes a delay in the formation of the primary recirculating region. Increasing the pitch rate also delays the formation. Increasing the Reynolds number hastens the appearance of the primary recirculating region and leads to the appearance of a shock on the top surface along with the formation of multiple recirculating regions near the leading edge. A linear stability analysis has shown that the appearance of the primary recirculating region is related to the inviscid instability of the flow.

14. SUBJECT TERMS	15. NUMBER OF PAGES
pitching airfoil, boundary-layer separation, effect of compressibility, effect of pitch rate effect of Reynolds number, linear stability analysis	142
	16. PRICE CODE

17. SECURITY CLASSIFICATION OF REPORT	18. SECURITY CLASSIFICATION OF THIS PAGE	19. SECURITY CLASSIFICATION OF ABSTRACT	20. LIMITATION OF ABSTRACT
UNCLASSIFIED	UNCLASSIFIED	UNCLASSIFIED	UL

The views, opinions, and/or findings contained in this report are those of the author and should not be construed as an official Department of the Army position, policy, or decision, unless so designated by other documentation.

Table of Contents

List of Figures

List of Tables

1 INTRODUCTION

1.1 Motivation

The aerodynamic characteristics (e.g., lift, drag and moment) of an airfoil in unsteady motion are significantly affected by the viscous boundary layer. Under certain conditions, the boundary layer on an airfoil in pitching motion separates from the airfoil surface, forming a large concentrated region of vorticity known as the dynamic stall vortex. This phenomenon is characterized by dramatic changes in the aerodynamic performance (e.g., a rapid change in the moment) of the airfoil, and is of significant interest to rotorcraft, for example. However, the complex unsteady effects have not yet been completely understood, and there is a need for more fundamental research in this field.

Boundary layer separation is an integral part of the dynamic stall. Qualitatively, boundary layer separation is the *breakdown* of the boundary layer model which divides the flow into two weakly interacting regions (*i.e.*, an irrotational flow occupying most of the fluid volume and a thin viscous region adjacent to the solid boundary). For 2-D steady flows, the criterion for boundary layer separation is well known, and indicated by the appearance of zero shear stress at the surface. For a pitching airfoil, the breakdown of the boundary layer (separation) is preceded by the formation of a large scale recirculating region[1] above the airfoil surface. The recirculating region grows in size in both transverse and normal directions and at a later stage detaches from the airfoil surface (separation) to give rise to the phenomenon of dynamic stall.

The focus of the present research is the understanding of the initial ("incipient") stages of boundary layer separation over a pitching airfoil, with particular emphasis on the details of the separation phenomenon near the leading edge. Improved understanding of the incipient stages of boundary layer separation may lead to methods for modification

[1]A recirculating region can be defined as a flow possessing vorticity with closed streamlines.

or control of the separation process.

1.2 Literature Survey

A number of recent research activities have focused on the study of the processes leading to the dynamic stall and the dynamic stall phenomenon itself. Experimental studies have continued to provide very important insights into the physics of the dynamic stall process. McCroskey *et al* [24] studied incompressible boundary layer separation using oil smoke visualization and described the three different types of boundary layer separation observed in the case of an oscillating airfoil. Acharya and Metwally [1] categorized and quantified the sources of vorticity and identified the key mechanisms in the initiation, development, growth and movement of the dynamic stall vortex. Chandrasekhara and Ahmed [8] obtained the instantaneous velocity measurements over an oscillating airfoil in a compressible medium which showed the formation of the separation bubble over the airfoil that persists until angles close to when the dynamic stall vortex forms and convects. Carr *et al* [5] studied dynamic stall using real time interferometry and the measurements of the flow near the leading edge of an oscillating airfoil offered the detailed experimental quantification of the locally compressible flow field that surrounds an oscillating airfoil at moderate subsonic Mach numbers and also revealed significant characteristics of the complex, and rapidly varying locally supersonic flow. Karim [18] experimentally studied the evolution of the dynamic stall vortex in the vicinity of leading edge of a 2-D pitching airfoil using smoke-wires and studied the pitch rate effects on the growth of the dynamic stall vortex. He also investigated the control of dynamic stall using suction. Chandrasekhara *et al* [9] used real-time point diffraction interferometry to study the compressible dynamic stall over a airfoil pitching at a constant rate and observed the appearance of small multiple shocks near the leading edge above the shear layer for free stream Mach numbers above 0.4. Crisler *et al* [11] investigated the unsteady flow over a airfoil pitching at a constant rate using a Particle Image Velocimetry (PIV) system and identified the role of absolute instability of a separating shear layer in the dynamic stall process.

Computational studies have long been used to improve the understanding of the

unsteady flow behavior. Mehta [26] computed the laminar flow past an oscillating airfoil at Reynolds numbers (based on the airfoil chord) of 5×10^3 and 10^4 to gain insight into the mechanism of dynamic stall. He qualitatively compared his computed instantaneous streamlines with the trajectories of air bubbles[2] observed in water tunnel experiments. Shih *et al* [37] observed that the leading edge boundary layer separation leads to the formation of a vortical structure which dominates the aerodynamic performance. Ghia *et al* [15] and Yang *et al* [58] analyzed the effect of modulated suction or injection in delaying the onset of dynamic stall over pitching NACA airfoils and also successfully compared their computational results with the previous computations of Mehta [26] and the experimental results for $Re_c = 10^4$ and $Re_c = 4.5 \times 10^4$. They monitored the separation and through numerical experimentation devised suitable leading-edge suction and equal mass of trailing edge injection (necessary to maintain zero net normal mass addition and to keep the boundary condition at infinity unchanged, due to the use of streamfunction-vorticity formulation and constant vorticity boundary condition around the airfoil) to manage the evolution of the dynamic stall vortex, and depicted the role of separation in the formation of the stall vortex. Visbal [52] presented investigations of flow control by boundary layer suction and a moving wall. He also investigated the effect of compressibility on dynamic stall and determined that an increase in Mach number reduces the stall delay [51]. Currier and Fung [12] found that with increasing unsteadiness the delay between static stall angle and dynamics stall onset decreases. Shida *et al* [36] computed the flowfield around an oscillating NACA-0012 airfoil by solving the two-dimensional compressible Navier-Stokes equations employing a block pentadiagonal matrix scheme and were able to capture the lift stall and lift restoration in the downstroke of the airfoil motion.

Analytical studies have been very helpful in the fundamental understanding of unsteady separation and linking the physics with the experimental and numerical observations. Doligalski *et al* [13] have reviewed some of the important studies conducted on vortex interactions and separation including dynamic stall. Smith [38, 39, 41] described the instability of a leading edge separation bubble and finite time breakup of the boundary layer. He found that initially unsteady developments take place over a relatively

[2]Air bubble trajectories are not instantaneous streamlines in an unsteady flow.

slow time scale but then the corresponding solution breaks down with a singularity, forcing a switch to a faster and more nonlinear process. Peridier *et al* [28, 29] examined the interaction of a vortex with a boundary layer. Some additional research has also focused on some geometrically simpler configurations such as a circular cylinder set into motion impulsively [47, 40]. Improved understanding of the temporal and spatial scales associated with the dynamic stall process have been obtained from these studies.

Comprehensive reviews of advances in the field of computational and experimental studies of dynamic stall have been presented by Carr [4] and Carr and McCroskey [6].

1.3 Present Research

The main objective of the present paper is improved understanding of the effects of compressibility, pitch rate and Reynolds number on the initial stages of unsteady leading edge boundary layer separation for a pitching airfoil. An NACA-0012 airfoil has been selected, consistent with previous computational and experimental studies. Figure 1 shows schematically the typical stages in the pitch up motion of an airfoil, where the instantaneous streamlines are displayed in a reference frame attached to the airfoil. At low angles of attack, the flow is attached to the airfoil surface and there is no reversed flow present in the flowfield. With increase in the angle of attack, a reverse flow region forms over the airfoil top surface and finally extends up to the leading edge. A leading edge vortex forms over the airfoil which eventually moves away from the airfoil surface to give rise to dynamic stall. The present research deals with the understanding of the stages from (b) (attached flow) through (e) (dynamic stall), but not including dynamic stall itself.

The three-dimensional parameter space of Mach number, pitch rate and Reynolds number has been investigated (where the Reynolds number is based on the chord length c and the non-dimensional pitch rate is $\Omega_o^+ = \Omega c/U_\infty$, where Ω is the pitch rate in rad/s and U_∞ is the freestream velocity). The seven points studied in the three-dimensional space are indicated by solid circles in figure 2. Some of the previous laminar Navier-Stokes simulations of a pitching airfoil due to other researchers have also been indicated on the figure. Computations have been performed using two different

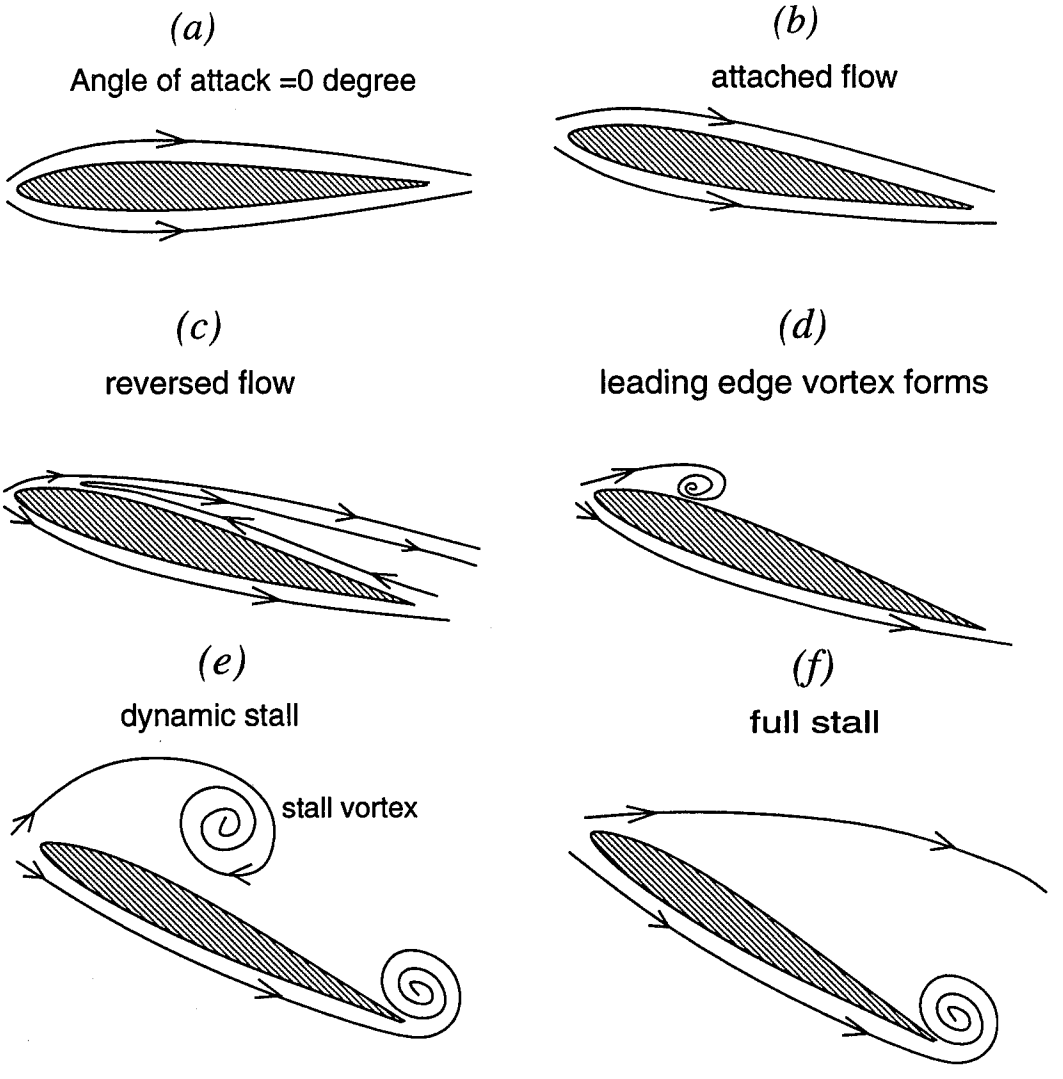

Figure 1: Stages in the pitching of an airfoil

numerical algorithms. The first algorithm, denoted the *structured grid algorithm*, is an approximate-factorization implementation of Beam-Warming's method [2] using a structured, boundary-fitted grid system. The second algorithm [20], denoted the *unstructured grid algorithm*, employs an unstructured grid of triangles and utilizes the flux-differencing splitting method of Roe [34] for the inviscid fluxes and a discrete representation of Gauss' Theorem for the viscous fluxes and heat transfer. The structured grid algorithm is implicit, while the unstructured grid algorithm (as employed in this study) is explicit. Both algorithms are second order accurate in space and time. The structured grid solver has been employed to compute all the seven cases. The unstruc-

tured grid solver has been employed to compute one of the cases in order to provide an independent examination of the accuracy of the computations. The airfoil is pitched about the quarter chord axis. The flow conditions for the seven computed cases were chosen on the basis of simplicity and feasibility. The Reynolds numbers were selected to ensure laminar flow. The Mach numbers were chosen to obtain subsonic flow in one case and regions of supersonic flow in the other case. The studies were conducted with special emphasis on understanding the leading edge separation, of course. The boundary layer separates near the trailing edge very early in the pitch up motion, but for most of the cases it is the separation of the boundary layer near the leading edge which is responsible for the eventual dynamic stall process.

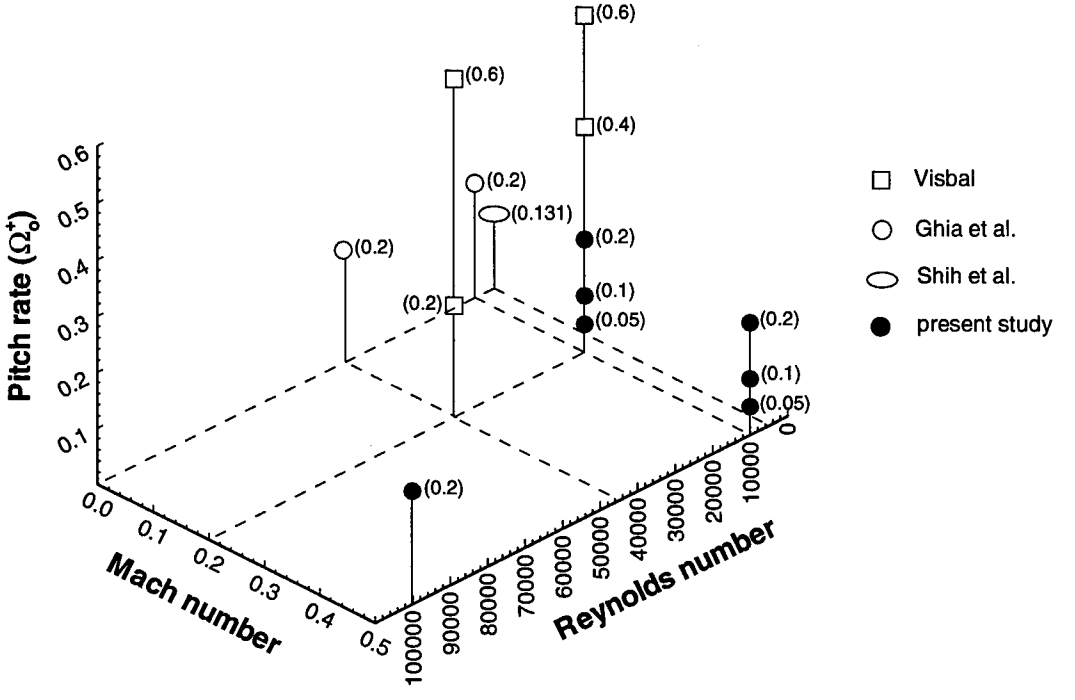

Figure 2: Points investigated in the three-dimensional parameter space (pitch rate value is indicated by the number in the bracket)

The early study of Ghosh Choudhuri *et al* [16] at $Re_c = 10^4$, $M_\infty = 0.2$, and non-dimensional pitch rate $\Omega_o^+ = 0.2$ reported the appearance of the primary recirculating region (a flow structure possessing vorticity with closed streamlines) to be a very important development leading to the separation process. The primary recirculating region eventually separates from the airfoil surface to give rise to the dynamic stall vortex.

Therefore, the appearance of the primary recirculating region has been closely monitored. A linear stability analysis has also been conducted to determine whether the appearance of the primary recirculating region is related to the instability of the flowfield.

This study differs from previous computational studies in the following aspects :

- This is a comprehensive study of an expanded three-dimensional parametric space of Mach number, pitch rate and Reynolds number.
- The initial stages of the development of the boundary layer leading to the development of the dynamic stall vortex has been studied.
- A linear stability analysis has been performed to understand the reason for the formation of the primary recirculating region.

The governing equations for the numerical simulations utilizing structured and unstructured grid algorithms have been presented in sections 2 and 4, respectively. The algorithms have been described in detail in sections 3 and 5. These sections also contain details about the boundary conditions used for the numerical simulations. Sections 6 and 7 discuss the code validation study for a number of cases through comparison with analytical or previous computations. Section 8 specifies the problem itself. Section 9 consists of the results for the present study. Section 10 provides a summary of the important results and future work.

2 GOVERNING EQUATION (STRUCTURED GRID)

The governing equations employed for the numerical simulation of unsteady flow past an airfoil utilizing a structured grid are presented in this chapter. The equations are the two-dimensional, unsteady, compressible, laminar Navier-Stokes equations written in strong conservation form for general curvilinear coordinates.

2.1 Equations in Cartesian Coordinates

The unsteady, compressible, two-dimensional Navier-Stokes equations in strong conservation form can be expressed in the Cartesian coordinates in the following form :

$$\frac{\partial U}{\partial t} + \frac{\partial \widehat{F}}{\partial x} + \frac{\partial \widehat{G}}{\partial y} = \frac{\partial \widehat{R}}{\partial x} + \frac{\partial \widehat{S}}{\partial y} \tag{1}$$

where

$$U = \begin{pmatrix} \rho \\ \rho u \\ \rho v \\ \rho e \end{pmatrix} ; \widehat{F} = \begin{pmatrix} \rho u \\ \rho u^2 + p \\ \rho uv \\ u(p + \rho e) \end{pmatrix} ; \widehat{G} = \begin{pmatrix} \rho v \\ \rho uv \\ \rho v^2 + p \\ v(p + \rho e) \end{pmatrix} ; \widehat{R} = \begin{pmatrix} 0 \\ \tau_{xx} \\ \tau_{xy} \\ R_4 \end{pmatrix} ; \widehat{S} = \begin{pmatrix} 0 \\ \tau_{xy} \\ \tau_{yy} \\ S_4 \end{pmatrix} \tag{2}$$

and

$\tau_{xx} = (\lambda + 2\mu)u_x + \lambda v_y$

$\tau_{xy} = \mu(u_y + v_x)$

$\tau_{yy} = (\lambda + 2\mu)v_y + \lambda u_x$

$R_4 = u\tau_{xx} + v\tau_{xy} + \frac{C_p \mu}{P_r} T_y$

$S_4 = u\tau_{xy} + v\tau_{yy} + \frac{C_p \mu}{P_r} T_y$

The density, ρ, static pressure, p, and the absolute temperature, T, obey the equation of state :

$$p = \rho RT = \rho(\gamma - 1)\{e - \frac{1}{2}(u^2 + v^2)\} \tag{3}$$

where R is the Universal gas constant, e is the total energy per unit mass, λ is the second coefficient of viscosity ($\lambda = -2/3\mu$), and γ is the ratio of specific heats.

The dynamic molecular viscosity is assumed to satisfy Sutherland's relation [56]:

$$\frac{\mu}{\mu_o} = \left(\frac{T}{T_o}\right)^{\frac{3}{2}} \frac{T_o + S_1}{T + S_1} \tag{4}$$

where S_1 is the Sutherland's reference temperature ($198°R$ for air), and $\mu_o = \mu(T_o)$.

The molecular Prandtl number, Pr (0.73 for air), and the specific heat at constant pressure, C_p, are assumed constant.

2.2 Equations in General Curvilinear Coordinates

The aerodynamic flow over an airfoil is characterized by a relatively complex configuration. It is very difficult to describe such configurations in the standard cartesian or polar coordinates. Writing the governing equations in terms of general "boundary-conforming" curvilinear coordinates helps in simplifying the numerical simulation of aerodynamic flows. The physical boundaries of the flow are mapped into constant transformed coordinate lines, and this eliminates the inaccuracies and the need for interpolation in the numerical implementation of the boundary conditions. It also allows a more efficient resolution of the features of the flow when high gradients are associated.

A time dependent non-singular transformation is introduced : $(x, y) \rightarrow (\xi, \eta)$, where $\xi = \xi(x, y, t)$, and $\eta = \eta(x, y, t)$. With this transformation the Navier-Stokes equations (Eqn. (1)) can be written as [43]:

$$\frac{\partial q}{\partial t} + \frac{\partial F}{\partial \xi} + \frac{\partial G}{\partial \eta} = \frac{\partial}{\partial \xi} V_1(q, q_\xi) + \frac{\partial}{\partial \xi} V_2(q, q_\eta) + \frac{\partial}{\partial \eta} W_1(q, q_\xi) + \frac{\partial}{\partial \eta} W_2(q, q_\eta) \tag{5}$$

where

$$q = \frac{1}{J}\begin{pmatrix} \rho \\ \rho u \\ \rho v \\ \rho e \end{pmatrix}; F = \frac{1}{J}\begin{pmatrix} \rho \mathcal{U} \\ \rho u \mathcal{U} + \xi_x p \\ \rho v \mathcal{U} + \xi_y p \\ (p + \rho e)\mathcal{U} - \xi_t p \end{pmatrix}; G = \frac{1}{J}\begin{pmatrix} \rho \mathcal{V} \\ \rho u \mathcal{V} + \eta_x p \\ \rho v \mathcal{V} + \eta_y p \\ (p + \rho e)\mathcal{V} - \eta_t p \end{pmatrix}$$

$$V_1 = \frac{1}{J}\begin{pmatrix} 0 \\ b_1 u_\xi + b_2 v_\xi \\ b_2 u_\xi + b_3 v_\xi \\ b_1 u u_\xi + b_2(v u_\xi + u v_\xi) + b_3 v v_\xi + b_4 T_\xi \end{pmatrix}$$

$$V_2 = \frac{1}{J}\begin{pmatrix} 0 \\ c_1 u_\eta + c_2 v_\eta \\ c_3 u_\eta + c_4 v_\eta \\ c_1 u u_\eta + c_2 u v_\eta + c_3 v u_\eta + c_4 v v_\eta + c_5 T_\eta \end{pmatrix}$$

$$W_1 = \frac{1}{J}\begin{pmatrix} 0 \\ c_1 u_\xi + c_2 v_\xi \\ c_3 u_\xi + c_4 v_\xi \\ c_1 u u_\xi + c_2 v u_\xi + c_3 u v_\xi + c_4 v v_\xi + c_5 T_\xi \end{pmatrix}$$

$$W_2 = \frac{1}{J}\begin{pmatrix} 0 \\ d_1 u_\eta + d_2 v_\eta \\ d_2 u_\eta + d_3 v_\eta \\ d_1 u u_\eta + d_2(v u_\eta + u v_\eta) + d_3 v v_\eta + d_4 T_\eta \end{pmatrix}$$

The Jacobian (J) of the transformation from (x, y) to (ξ, η), and the contravariant velocities, $\mathcal{U}$ and $\mathcal{V}$, are defined as

$$J = \xi_x \eta_y - \xi_y \eta_x = \frac{1}{x_\xi y_\eta - x_\eta y_\xi} \tag{6}$$

$$\mathcal{U} = \xi_t + \xi_x u + \xi_y v; \quad \mathcal{V} = \eta_t + \eta_x u + \eta_y v \tag{7}$$

The coefficients b_i, c_j, d_i (i=1,..,4; j=1,...,5) appearing in the viscous term of eqn. (5) are defined as follows

$$\begin{aligned} b_1 &= \mu\left(\frac{4}{3}\xi_x^2 + \xi_y^2\right) \\ b_2 &= \frac{1}{3}\mu \xi_x \xi_y \\ b_3 &= \mu\left(\xi_x^2 + \frac{4}{3}\xi_y^2\right) \\ b_4 &= C_p \frac{\mu}{Pr}\left(\xi_x^2 + \xi_y^2\right) \end{aligned} \tag{8}$$

$$
\begin{aligned}
c_1 &= -\mu\left(\frac{4}{3}\xi_x\eta_x + \xi_y\eta_y\right) \\
c_2 &= -\mu\left(\frac{2}{3}\xi_x\eta_y - \xi_y\eta_x\right) \\
c_3 &= \mu\left(\xi_x\eta_y - \frac{2}{3}\xi_y\eta_x\right) \\
c_4 &= -\mu\left(\xi_x\eta_x + \frac{4}{3}\xi_y\eta_y\right) \\
c_5 &= -C_p\frac{\mu}{Pr}\left(\xi_x\eta_x + \xi_y\eta_y\right)
\end{aligned} \tag{9}
$$

$$
\begin{aligned}
d_1 &= \mu\left(\frac{4}{3}\eta_x^2 + \eta_y^2\right) \\
d_2 &= \frac{1}{3}\mu\eta_x\eta_y \\
d_3 &= \mu\left(\eta_x^2 + \frac{4}{3}\eta_y^2\right) \\
d_4 &= C_p\frac{\mu}{Pr}\left(\eta_x^2 + \eta_y^2\right)
\end{aligned} \tag{10}
$$

The transformation metrics ξ_t, ξ_x, ξ_y, η_t, η_x, and η_y appearing in the above equations can be defined in terms of x_ξ, x_η, y_ξ, and y_η, which can be computed numerically by applying a finite-difference formula to the body-conforming grid.

$$\xi_t = (-x_t y_\eta + y_t x_\eta)J \tag{11}$$

$$\eta_t = (x_t y_\xi - y_t x_\xi)J \tag{12}$$

$$\xi_x = y_\eta J \tag{13}$$

$$\eta_x = -y_\xi J \tag{14}$$

$$\xi_y = -x_\eta J \tag{15}$$

$$\eta_y = x_\xi J \tag{16}$$

The Beam-Warming algorithm has been applied to the set of equations presented in this section and the details of the algorithm are presented in the next section.

3 NUMERICAL ALGORITHM (STRUCTURED GRID)

Unsteady aerodynamic flow problems require the temporal accuracy along with the spatial accuracy in the solution of the unsteady Navier-Stokes equations. Numerical integration in time is performed to solve the governing equations and the transients are of prime importance. It is also desirable to employ a time-marching, finite difference algorithm that is unconditionally stable and therefore allows the use of a large time increment, to solve the steady part of the problem.

Beam and Warming [2] have developed a fully implicit, unconditionally stable, non-iterative finite-difference scheme for the solution of hyperbolic and mixed hyperbolic-parabolic systems of partial difference equations. The Beam-Warming scheme employs a time-linearization procedure which eliminates the need for an iterative method at each time step and utilizes the ADI technique, which results in the solution of block-tridiagonal linear systems for each coordinate direction. It utilizes a structured boundary-fitted grid. The Beam-warming algorithm in its "delta" formulation with Trapezoidal implicit time differencing and centered spatial approximations is second order accurate in time and space. This section presents the numerical implementation of Beam-Warming algorithm. The boundary conditions and grid generation are also discussed.

3.1 Beam-Warming Algorithm

The governing equations are solved in an inertial frame of reference. Trapezoidal temporal discretization of the Navier-Stokes equations (eqn. (5)) gives

$$\begin{aligned}\Delta q^n &= \frac{1}{2}\Delta t\left[\frac{\partial}{\partial\xi}(-\Delta F+\Delta V_1+\Delta V_2)+\frac{\partial}{\partial\eta}(-\Delta G+\Delta W_1+\Delta W_2)\right]^n + \\ &\quad \Delta t\left[\frac{\partial}{\partial\xi}(-F+V_1+V_2)+\frac{\partial}{\partial\eta}(-G+W_1+W_2)\right]^n+\mathcal{O}(\Delta t^3) \qquad (17)\end{aligned}$$

where n indicates the temporal index and Δt is the time increment. Therefore, $q^n = q(n\Delta t) = q(t)$. Also,

$$\begin{aligned} \Delta q^n &= q^{n+1} - q^n; \quad \Delta F^n = F^{n+1} - F^n; \quad \Delta G^n = G^{n+1} - G^n; \quad \Delta V_1^n = V_1^{n+1} - V_1^n \\ \Delta V_2^n &= V_2^{n+1} - V_2^n; \quad \Delta W_1^n = W_1^{n+1} - W_1^n; \quad \Delta W_2^n = W_2^{n+1} - W_2^n \end{aligned} \tag{18}$$

The delta-form of Beam-Warming algorithm results in several advantages, including a steady state solution independent of Δt and a more direct derivation of the factored scheme. The flux-vectors are non-linear functions of q, and therefore a linearization procedure which retains the same temporal accuracy of eqn. (17) has to be introduced in order to develop a non-iterative algorithm. A linear equation with the same temporal accuracy as eqn. (17) can be obtained if Taylor series expansion is used :

$$F^{n+1} = F^n + \left(\frac{\partial F}{\partial q}\right)^n (q^{n+1} - q^n) + \mathcal{O}(\Delta t^2) \tag{19}$$

$$or, \quad \Delta F^n = A^n \Delta q^n + \mathcal{O}(\Delta t^2) \tag{20}$$

where

$$A = \frac{\partial F}{\partial q} \qquad (Jacobian \quad matrix) \tag{21}$$

Similarly,

$$\Delta G^n = B^n \Delta q^n + \mathcal{O}(\Delta t^2) \tag{22}$$

$$\Delta V_1^n = (P - R_\xi)^n \Delta q^n + \frac{\partial}{\partial \xi}(R\Delta q)^n + \mathcal{O}(\Delta t^2) \tag{23}$$

$$\Delta W_2^n = (Q - S_\eta)^n \Delta q^n + \frac{\partial}{\partial \eta}(S\Delta q)^n + \mathcal{O}(\Delta t^2) \tag{24}$$

where

$$B = \frac{\partial G}{\partial q} \tag{25}$$

$$P = \frac{\partial V_1}{\partial q} \tag{26}$$

$$R = \frac{\partial V_1}{\partial q_\xi} \tag{27}$$

$$Q = \frac{\partial W_2}{\partial q} \tag{28}$$

$$S = \frac{\partial W_2}{\partial q_\eta} \tag{29}$$

The constituents of the Jacobian matrices are given in Appendix A.

A difficulty arises from the spatial cross-derivative terms $\frac{\partial}{\partial\xi}(\Delta V_2)^n$ and $\frac{\partial}{\partial\eta}(\Delta W_1)^n$. If these terms were treated in the same manner as eqn (19), considerable difficulty will be encountered in constructing an efficient spatially factored algorithm. In order to facilitate the approximate factorization procedure it is appropriate and consistent to treat the spatial cross-derivative terms mentioned above explicitly or eliminate them altogether in eqn (17). Studies [2] on the effect of the cross derivative terms in the algorithm have indicated that there is very little change if the spatial cross derivative terms are dropped altogether.

Substitution of eqns. (20) to (24) into eqn. (17), and dropping the spatial cross-derivative terms yields

$$\left\{I+\frac{\Delta t}{2}\left[\frac{\partial}{\partial\xi}(A-P+R_\xi)^n-\frac{\partial^2 R^n}{\partial\xi^2}+\frac{\partial}{\partial\eta}(B-Q+S_\eta)^n-\frac{\partial^2 S^n}{\partial\eta^2}\right]\right\}\Delta q^n=$$
$$\Delta t\left[\frac{\partial}{\partial\xi}(-F+V_1+V_2)^n+\frac{\partial}{\partial\eta}(-G+W_1+W_2)^n\right]+\mathcal{O}(\Delta t^3) \qquad (30)$$

where the notations of the form

$$\left[\frac{\partial}{\partial\xi}(A-P+R_\xi)^n\right]\Delta q^n=\frac{\partial}{\partial\xi}[(A-P+R_\xi)\Delta q]^n$$
$$\textit{and}\quad \left[\frac{\partial}{\partial\eta}(B-Q+S_\eta)^n\right]\Delta q^n=\frac{\partial}{\partial\eta}[(B-Q+S_\eta)\Delta q]^n$$

have been used for convenience.

Equation (30) is linear, but still would result in a very large matrix inversion problem when the spatial derivatives are replaced by finite-difference formulas. To make the problem simple, the left hand side operator in eqn. (30) is factored as follows without disrupting the formal accuracy of the algorithm.

$$\left\{I+\frac{\Delta t}{2}\left[\frac{\partial}{\partial\xi}(A-P+R_\xi)^n-\frac{\partial^2 R^n}{\partial\xi^2}\right]\right\}\left\{I+\frac{\Delta t}{2}\left[\frac{\partial}{\partial\eta}(B-Q+S_\eta)^n-\frac{\partial^2 S^n}{\partial\eta^2}\right]\right\}\Delta q^n$$
$$=\Delta t\left[\frac{\partial}{\partial\xi}(-F+V_1+V_2)^n+\frac{\partial}{\partial\eta}(-G+W_1+W_2)^n\right]+\mathcal{O}(\Delta t^3) \qquad (31)$$

The factored scheme (eqn. (31)) is implemented in the following alternating direction fashion

$$\left\{I+\frac{\Delta t}{2}\left[\frac{\partial}{\partial\xi}(A-P+R_\xi)^n-\frac{\partial^2 R^n}{\partial\xi^2}\right]\right\}\Delta q^c=$$
$$\Delta t\left[\frac{\partial}{\partial\xi}(-F+V_1+V_2)^n+\frac{\partial}{\partial\eta}(-G+W_1+W_2)^n\right] \qquad (32)$$

$$\left\{I + \frac{\Delta t}{2}\left[\frac{\partial}{\partial \eta}(B - Q + S_\eta)^n - \frac{\partial^2 S^n}{\partial \eta^2}\right]\right\}\Delta q^n = \Delta q^c \tag{33}$$

$$q^{n+1} = q^n + \Delta q^n \tag{34}$$

where Δq^c is a dummy intermediate vector.

The spatial derivatives appearing in eqns. (32) and (33) have to be approximated by appropriate finite difference quotients. Figure (3) shows a part of the transformed uniform rectangular grid, employed for solving the equations, where

$$\xi_i = (i-1)\Delta\xi; \quad 1 \le i \le IL; \qquad \eta_j = (j-1)\Delta\eta; \quad 1 \le j \le JL \tag{35}$$

where the subscripts i and j refer to the ξ and η direction respectively. For convenience $\Delta\xi$ and $\Delta\eta$ are selected to be 1.0, and hence have been omitted in rest of the equations. The transformed derivatives x_ξ, x_η, y_ξ and y_η are all computed using centered finite differences at all the interior points, and one-sided, second-order accurate approximations along the boundaries.

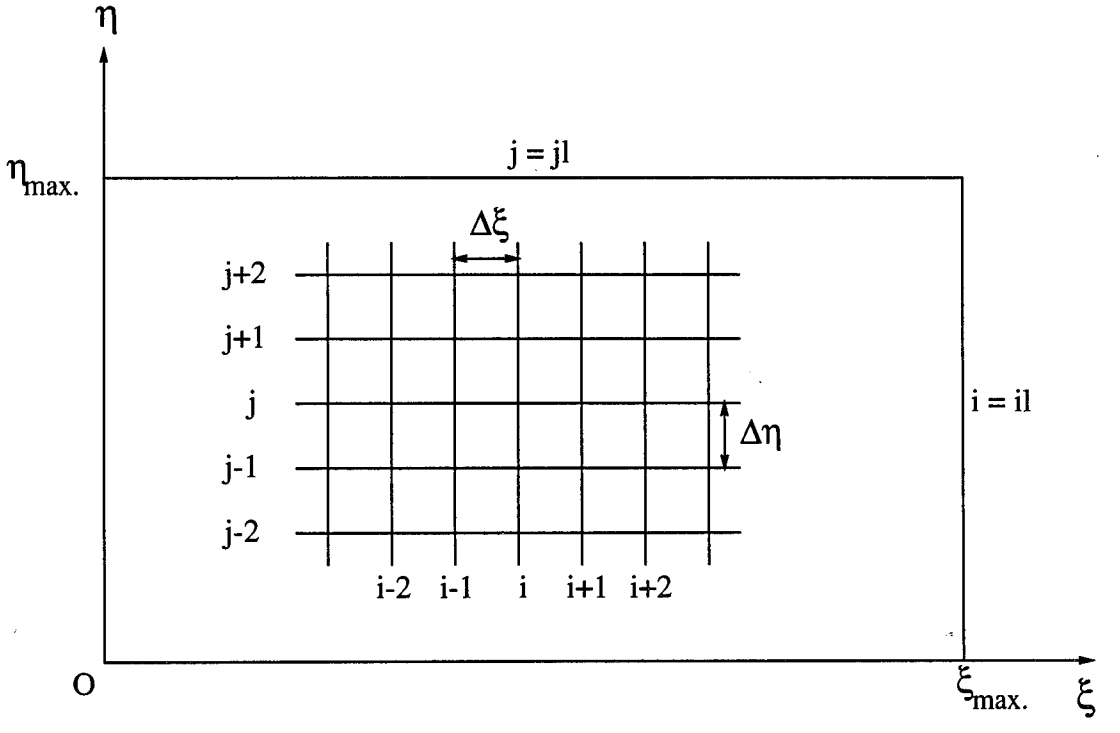

Figure 3: Transformed plane.

Centered finite difference discretization is applied to the spatial derivatives in eqns. (32) and (33)

$$\left\{I + \frac{\Delta t}{2}\left[\mu_\xi A_{i,j} + \delta_\xi(-P + R_\xi)_{i,j} - \delta_\xi^2 R_{i,j}\right]^n\right\}\Delta q^c_{i,j} = -\Delta t\left[\mu_\xi(F - V_2)_{i,j} + \mu_\eta(G - W_1)_{i,j} - \delta_\xi V_{1i,j} - \delta_\eta W_{2i,j}\right]^n \tag{36}$$

$$\{I + \Delta t[\mu_j B_{i,j} + \delta_j(-Q + S_\eta)_{i,j} - \delta_j^2 S_{i,j}]^n\}\Delta q^n_{i,j} = \Delta q^c_{i,j} \tag{37}$$

where the finite-difference operators used are

$$\delta_\xi F_{i,j} = F_{i+\frac{1}{2},j} - F_{i-\frac{1}{2},j}; \qquad \mu_\xi F_{i,j} = \frac{1}{2}(F_{i+1,j} - F_{i-1,j})$$
$$\delta_\eta F_{i,j} = F_{i,j+\frac{1}{2}} - F_{i,j-\frac{1}{2}}; \qquad \mu_\eta F_{i,j} = \frac{1}{2}(F_{i,j+1} - F_{i,j-1}) \tag{38}$$

Beam-Warming algorithm is implemented in a standard ADI sequence. Equation (36) is solved first for the vector Δq^c for all constant η lines ($2 \leq j \leq JL - 1$). This step involves the solution of a block-tridiagonal linear system for each constant η line. Similarly, eqn. (37) is solved next for the vector Δq^n using the available values of the intermediate vector Δq^c for each constant ξ line. The vector q is updated at time $(n+1)$ using eqn. (34). The updated q vector gives the new flow variables at time step $(n+1)$.

3.2 Numerical Damping

A linear stability analysis of Beam-Warming algorithm indicates that the high frequency components of the solution are not damped when central spatial finite differences are employed [55]. Violation of stability condition produces an amplification of the various forms of error that are present in the numerical solution. These include truncation errors (due to inexact differentials), round-off errors (due to truncated arithmetics), and errors due to slightly inconsistent boundary conditions. The solution becomes stable when some artificial dissipation is added to the algorithm. The artificial dissipation term also provides smoothing for the capturing of embedded shocks. The present study employs fourth order explicit and second order implicit dissipation terms [32]. The fourth order explicit dissipation term removes the small wavelength oscillations ($2\Delta x$ oscillation) in the flowfield. The second order implicit dissipation term actually stabilizes the system by increasing the diagonal dominance of the block tridiagonal matrix

formed in the algorithm. The fourth-order explicit artificial dissipation term is appended to the right hand side of eqn. (36). The implicit dissipation term is added to the left hand side of eqn. (36). The addition of the artificial dissipation terms results in the following algorithm :

$$\left\{I + \frac{\Delta t}{2}\Big[\mu_\xi A_{i,j} + \delta_\xi(-P + R_\xi)_{i,j} - \delta_\xi^2 R_{i,j} - \omega_i J^{-1}\delta_\xi^2 J\Big]^n\right\}\Delta q^c_{i,j} = -\omega_e J^{-1}(\delta_\xi^4 + \delta_\eta^4)J q^n_{i,j}$$
$$-\Delta t\Big[\mu_\xi(F - V_2)_{i,j} + \mu_\eta(G - W_1)_{i,j} - \delta_\xi V_{1i,j} - \delta_\eta W_{2i,j}\Big]^n \quad (39)$$

$$\{I + \Delta t[\mu_j B_{i,j} + \delta_j(-Q + S_\eta)_{i,j} - \delta_j^2 S_{i,j} - \omega_i J^{-1}\delta_\eta^2 J]^n\}\Delta q^n_{i,j} = \Delta q^c_{i,j} \quad (40)$$

where ω_i and ω_e are the coefficients of implicit and explicit artificial dissipation terms, respectively. Addition of the second-order implicit damping term extends the linear stability bound of the fourth-order explicit damping term.

3.3 Geometric Conservation Law

The numerical simulation of unsteady flow past a moving airfoil involves the movement of the computational grid. Maintenance of global conservation of mass, momentum, and energy is an important part of numerical simulation. Use of boundary-conforming coordinate transformations and the subsequent application of finite-difference formulas to the moving boundaries or grids lead to grid-movement related errors in the solution. To remove the grid-movement related errors, the Geometric Conservation Law (GCL) is implemented in the algorithm [44]. Details of Geometric Conservation Law is presented in Appendix B. The following term is added to the right hand side of the algorithm to satisfy the global conservation (GCL).

$$GCL\ \ term = \Delta t\left\{\frac{\partial}{\partial\xi}\left(\frac{\xi_t}{J}\right) + \frac{\partial}{\partial\eta}\left(\frac{\eta_t}{J}\right)\right\}\frac{q^n}{J} \quad (41)$$

where

$$\xi_t = (-x_t y_\eta + y_t x_\eta)J; \qquad \eta_t = (x_t y_\xi - y_t x_\xi)J \quad (42)$$

3.4 Computational Grid

Nearly orthogonal boundary-fitted grids have been employed for the present study. For numerical simulation of flow past an airfoil, three types of boundary-fitted grids can be used : O-grid, C-grid and H-grid. In the present study, C-type grids have been utilized for the simulation. An advantage of the C-grid is improved grid resolution near the trailing edge. A schematic diagram of a C-grid has been shown in Fig. (4). The grids employed in the present study have been generated by the hyperbolic grid generation code developed by Kinsey and Barth [19]. The grid generation code needs the distribution of points on the airfoil surface and wake as input and gives the coordinates of the nodes of the C-grid as output. Figure (5) shows a part of the C-grid near the airfoil.

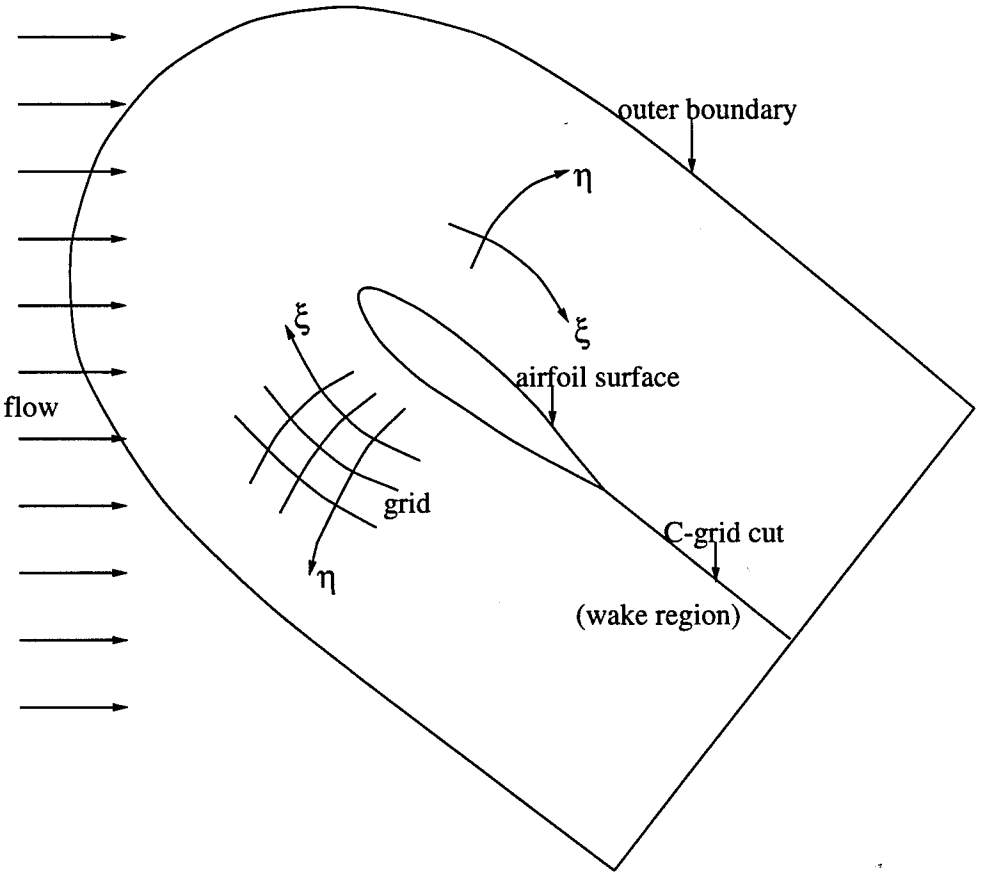

Figure 4: C-grid topology and computational boundaries.

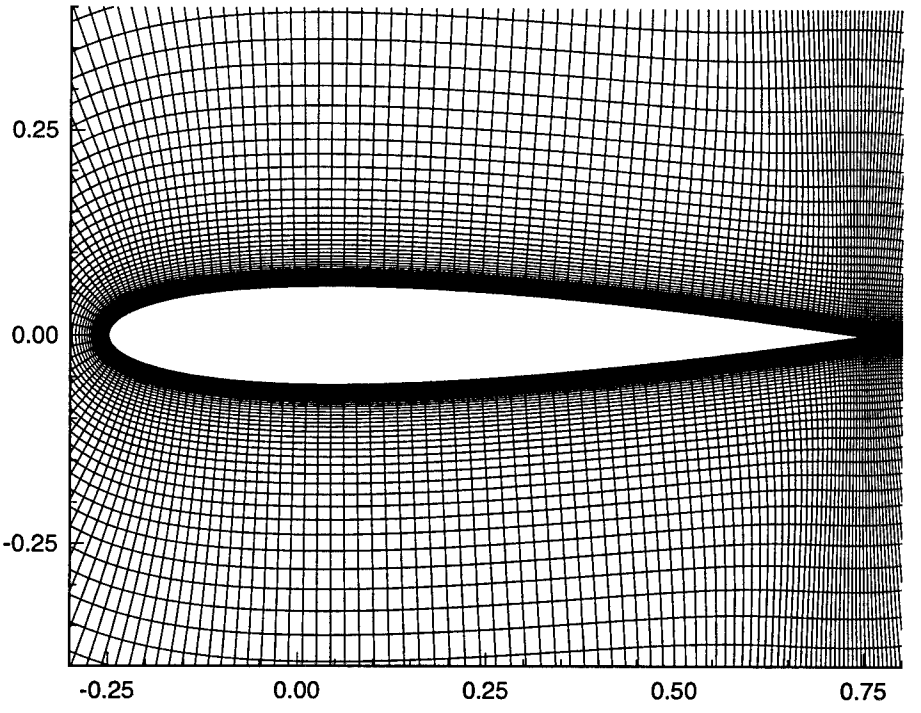

Figure 5: C-grid for NACA-0012 airfoil.

3.5 Boundary Conditions

Suitable boundary conditions have to be specified to completely define the problem. The boundary conditions are based on the particular problem being considered. In the present study, a C-grid has been employed. A C-grid has numerical boundaries at the airfoil surface, the outer boundary (inflow and outflow), and C-grid cut in the wake region. The boundary condition at all boundaries except at the C-grid cut in wake region are imposed explicitly.

On the airfoil surface, the following adiabatic, no-slip condition is applied :

$$\vec{U} = \vec{U}_B \tag{43}$$

$$\frac{\partial T}{\partial n} = 0 \tag{44}$$

The normal pressure gradient incorporates the effect of the airfoil motion.

$$\frac{\partial p}{\partial n} = -\rho \vec{a}_B \cdot \hat{n} \tag{45}$$

where $\vec{U}_B$ and $\vec{a}_B$ are the velocity and acceleration of the airfoil surface, respectively. For the rotation of the airfoil about a fixed axis with a pitch rate $\vec{\Omega}$, $\vec{U}_B$ and $\vec{a}_B$ can be defined as :

$$\vec{U}_B = \vec{\Omega} \times (\vec{r}_B - \vec{r}_O) \tag{46}$$

$$\vec{a}_B = \frac{d\vec{\Omega}}{dt} \times (\vec{r}_B - \vec{r}_O) - \Omega^2(\vec{r}_B - \vec{r}_O) \tag{47}$$

$\vec{r}_O$ is the position vector of the point of rotation and $\vec{r}_B$ is the position vector of the point on the airfoil where the velocity and the acceleration has to be determined.

At the inflow and outflow boundaries, a one-dimensional Method of Characteristics boundary condition [45] is applied. The Method of Characteristics is described in detail in Appendix C. A local coordinate system ($\overline{x}$, $\overline{y}$) is constructed orthogonal to the outer boundary with $\overline{x}$ normal to and directed outward from the boundary and $\overline{y}$ directed along the boundary. Assuming that the derivatives along the boundary can be neglected (one-dimensional), the following characteristic equations and corresponding characteristic variables have been found :

$$Characteristic\ equation\ 1\ (\mathcal{C}^1)\ :\ \overline{u} + \frac{2a}{\gamma - 1} = constant \quad along \quad \frac{d\overline{x}}{dt} = \overline{u} + a \tag{48}$$

$$Characteristic\ equation\ 2\ (\mathcal{C}^2)\ :\ \overline{u} - \frac{2a}{\gamma - 1} = constant \quad along \quad \frac{d\overline{x}}{dt} = \overline{u} - a \tag{49}$$

$$Characteristic\ equation\ 3\ (\mathcal{C}^3)\ :\ s = constant \quad along \quad \frac{d\overline{x}}{dt} = \overline{u} \tag{50}$$

$$Characteristic\ equation\ 4\ (\mathcal{C}^4)\ :\ \overline{v} = constant \quad along \quad \frac{d\overline{x}}{dt} = \overline{u} \tag{51}$$

where s is the entropy, a is the speed of sound, and $\overline{u}$ and $\overline{v}$ are velocities in $\overline{x}$ and $\overline{y}$ directions respectively.

All of the Riemann variables corresponding to the characteristics moving out of the computational domain have to be interpolated from the values available inside the domain. All other Riemann variables are set as boundary conditions. The outer boundary is defined at a sufficiently large distance from the airfoil to insure accuracy of this boundary condition (see section 4.2).

(i) Transformed domain

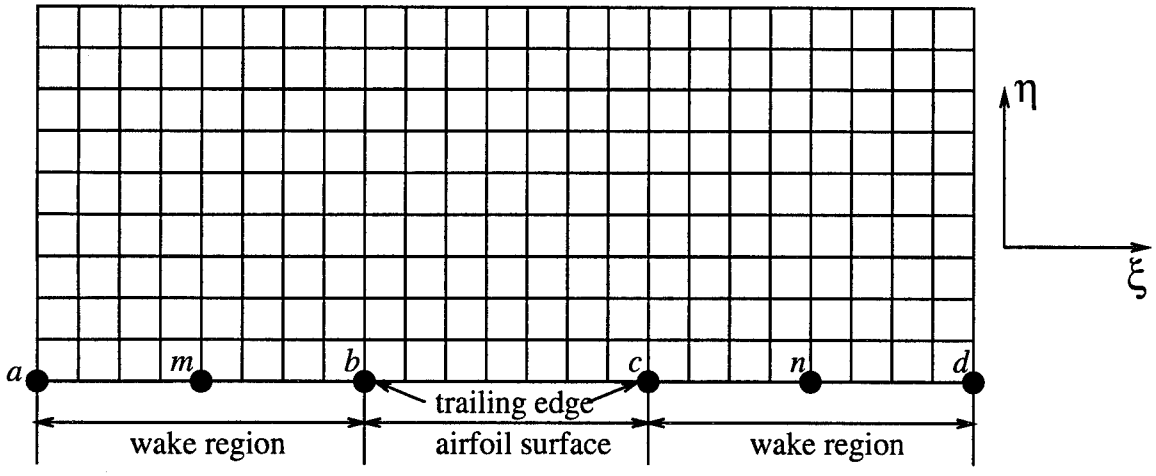

(ii) Wake region of computational domain

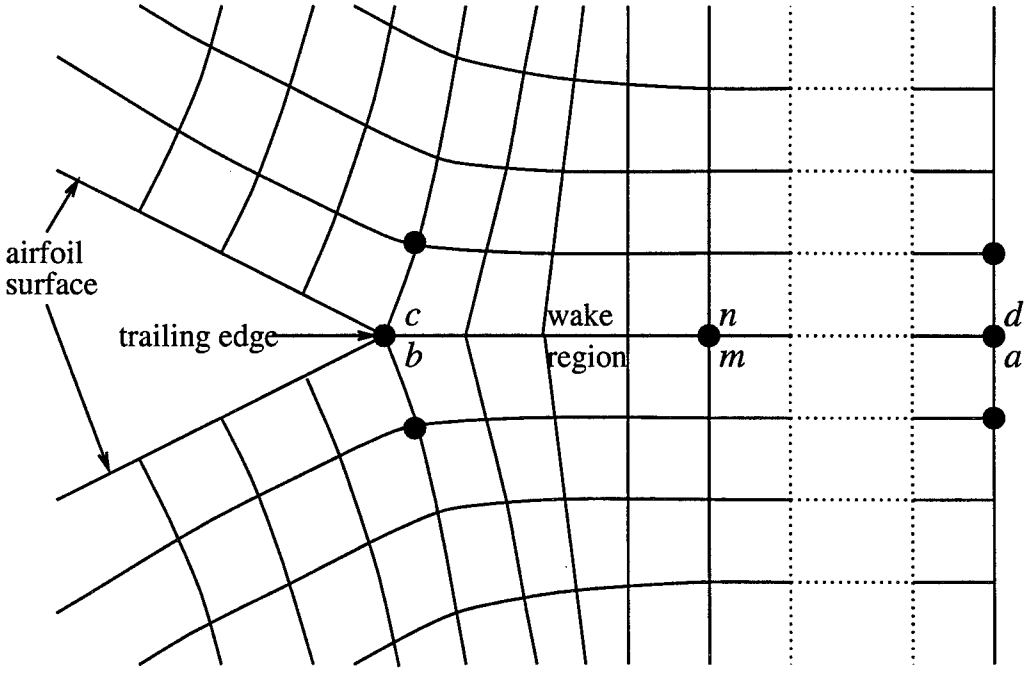

Figure 6: Computational and corresponding transformed domain of the region near the trailing edge showing the usage of periodic condition at the C-grid cut.

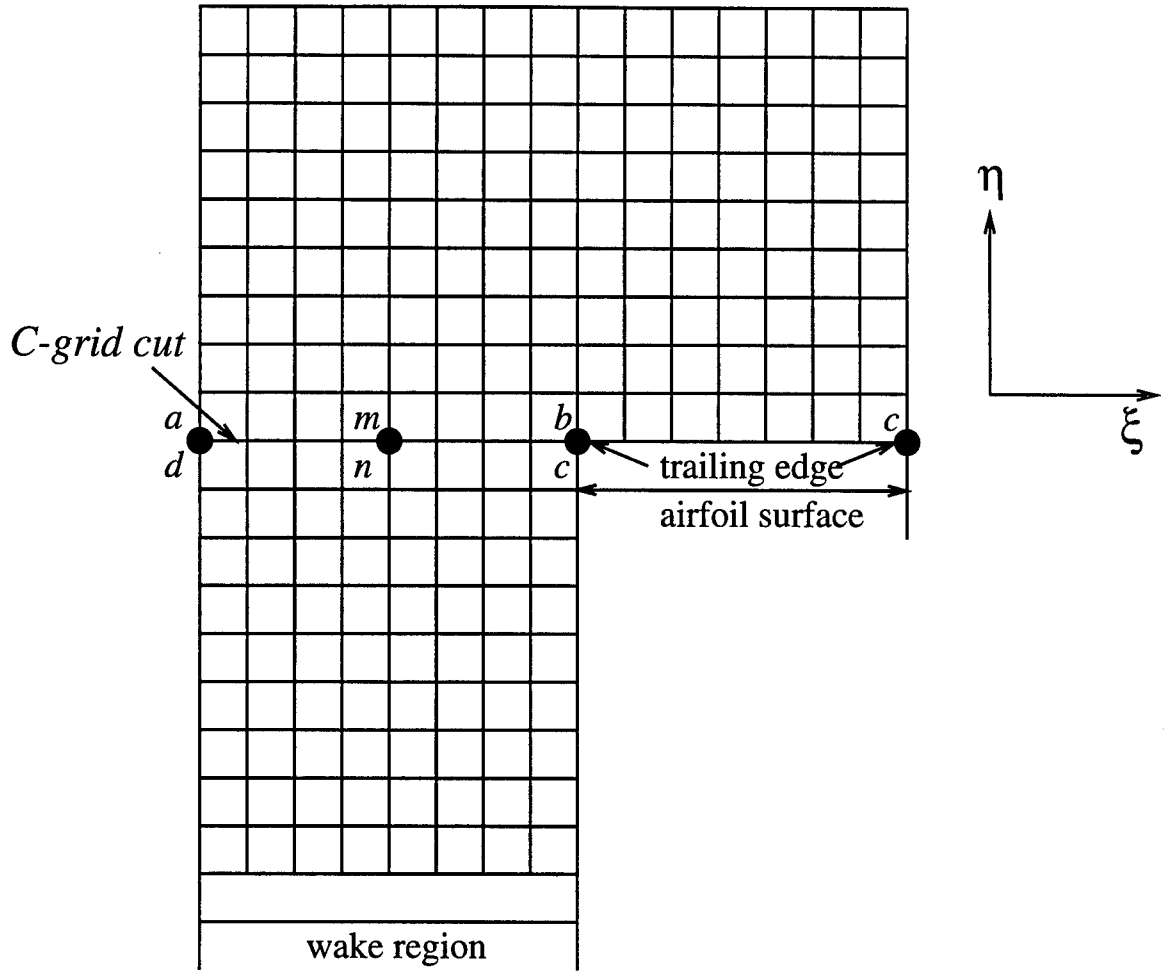

Figure 7: Transformed domain during the η-sweep.

At the C-grid cut (wake region), the flow variables are solved implicitly by imposing the periodicity condition. Figure (6) shows the region near the trailing edge and the transformed domain. The transformed domain is obtained by unwrapping the computational grid from around the airfoil. In the transformed domain the value of the flow variables at point 'a' are the same as at point 'd'. Similarly, values at 'm' and 'n' are equal, and at 'b' and 'c' (trailing edge) are equal and so on. This periodicity condition is used to solve for the flow variables implicitly at the C-grid cut. The Beam-Warming algorithm is solved utilizing the ADI scheme. The transformed domain looks like Fig. (6 (i)) during the ξ-sweep. But during the η-sweep, the transformed domain looks like fig. (7). This way the variables at the C-grid cut can be solved implicitly.

4 GOVERNING EQUATIONS (UNSTRUCTURED GRID)

The governing equations are the 2-D compressible laminar Navier-Stokes equations. For an arbitrary deformable control volume of volume V (per unit depth) and surface ∂V, the nondimensional equations are

$$\frac{d}{dt}\int_V Q dx dy + \int_{\partial V}(F dy - G dx) = 0 \tag{52}$$

where Q is the vector of dependent variables

$$Q = (\rho, \rho u, \rho v, \rho e)^T \tag{53}$$

where ρ is the density, u and v are the velocity components in the $x-$ and $y-$directions, and e is the total energy per unit mass,

$$e = \frac{T}{\gamma(\gamma-1)} + \tfrac{1}{2}(u^2+v^2) \tag{54}$$

where T is the static temperature and $\gamma = c_p/c_v$ is the ratio of specific heats. The flow variables are nondimensionalized using the dimensional reference quantities L (length), ρ_∞ (density), a_∞ (speed of sound) and T_∞ (static temperature). The superscript "T" denotes the vector transpose. The flux vectors are

$$F = \left\{ \begin{array}{c} \rho U \\ \rho u U + p - \tau_{xx} \\ \rho v U - \tau_{xy} \\ \rho e U + p u + \beta_x \end{array} \right\} \tag{55}$$

$$G = \left\{ \begin{array}{c} \rho V \\ \rho u V - \tau_{xy} \\ \rho v V + p - \tau_{yy} \\ \rho e V + p v + \beta_y \end{array} \right\} \tag{56}$$

where

$$U = u - u_s, \quad V = v - v_s \tag{57}$$

where u_s and v_s are the $x-$ and $y-$components of the velocity of the surface of the control volume. The components of the viscous stress tensor are

$$\begin{aligned} \tau_{xx} &= \frac{M_\infty}{Re_\infty}\mu\left(\frac{4}{3}\frac{\partial u}{\partial x} - \frac{2}{3}\frac{\partial v}{\partial y}\right) \\ \tau_{xy} &= \frac{M_\infty}{Re_\infty}\mu\left(\frac{\partial u}{\partial y} + \frac{\partial v}{\partial x}\right) \\ \tau_{yy} &= \frac{M_\infty}{Re_\infty}\mu\left(\frac{4}{3}\frac{\partial v}{\partial y} - \frac{2}{3}\frac{\partial u}{\partial x}\right) \end{aligned} \tag{58}$$

where M_∞ is the reference Mach number, Re_∞ is the reference Reynolds number, and μ is the molecular viscosity normalized by a suitable reference value μ_∞. The static pressure p is normalized by $\rho_\infty a_\infty^2$ and satisfies the Ideal Gas Equation

$$p = \frac{\rho T}{\gamma} \tag{59}$$

Furthermore,

$$\begin{aligned} \beta_x &= q_x - \tau_{xx}u - \tau_{xy}v \\ \beta_y &= q_y - \tau_{xy}u - \tau_{yy}v \end{aligned} \tag{60}$$

where the heat flux is

$$\begin{aligned} q_x &= -\mu\frac{M_\infty}{Re_\infty}\frac{1}{Pr\,(\gamma-1)}\frac{\partial T}{\partial x} \\ q_y &= -\mu\frac{M_\infty}{Re_\infty}\frac{1}{Pr\,(\gamma-1)}\frac{\partial T}{\partial y} \end{aligned} \tag{61}$$

where Pr is the Prandtl number.

It is convenient to decompose the flux vectors into their inviscid and viscous contributions

$$F_{inv} = \begin{Bmatrix} \rho U \\ \rho u U + p \\ \rho v U \\ \rho e U + p u \end{Bmatrix}$$

$$F_{vis} = \begin{Bmatrix} 0 \\ -\tau_{xx} \\ -\tau_{xy} \\ \beta_x \end{Bmatrix} \tag{62}$$

and

$$G_{inv} = \begin{Bmatrix} \rho V \\ \rho u V \\ \rho v V + p \\ \rho e V + p v \end{Bmatrix}$$

$$G_{vis} = \begin{Bmatrix} 0 \\ -\tau_{xy} \\ -\tau_{yy} \\ \beta_y \end{Bmatrix} \tag{63}$$

5 NUMERICAL ALGORITHM (UNSTRUCTURED GRID)

5.1 Implicit Algorithm

An unstructured grid of triangles is employed (Fig. 8). A cell-centered storage architecture is assumed where i denotes the cell index. The cell-averaged value of the vector of dependent variables Q is

$$Q_i \equiv \frac{1}{V_i} \int_V Q dx dy \tag{64}$$

where V_i is the volume (per unit depth) of the cell. The governing equations (52) are therefore

$$\frac{d}{dt}(Q_i V_i) + C_i = 0 \tag{65}$$

where C_i is the net flux across the cell faces

$$C_i = \int_{\partial V_i} (F dy - G dx) \tag{66}$$

It is furthermore assumed that V_i is constant, although this restriction can be easily relaxed.

A family of implicit algorithms for eqn. (65) is

$$\left\{ I + \frac{\beta}{1+\alpha} \frac{\Delta t}{V_i} \frac{\partial C_i}{\partial Q_i} \right\} \Delta Q_i^n + \frac{\beta}{1+\alpha} \frac{\Delta t}{V_i} \sum_{j \in \star} \frac{\partial C_i}{\partial Q_j} \Delta Q_j^n = -\frac{1}{1+\alpha} \frac{\Delta t}{V_i} C_i^n + \frac{\alpha}{1+\alpha} \Delta Q_i^{n-1} \tag{67}$$

where Δt is the time increment, and

$$\Delta Q_i^n = Q_i^{n+1} - Q_i^n \tag{68}$$

and $\sum_{j \in \star}$ denotes the summation over all cells constituting the numerical domain of dependence ("star") in the application of eqn. (65) at cell i with the exception of the

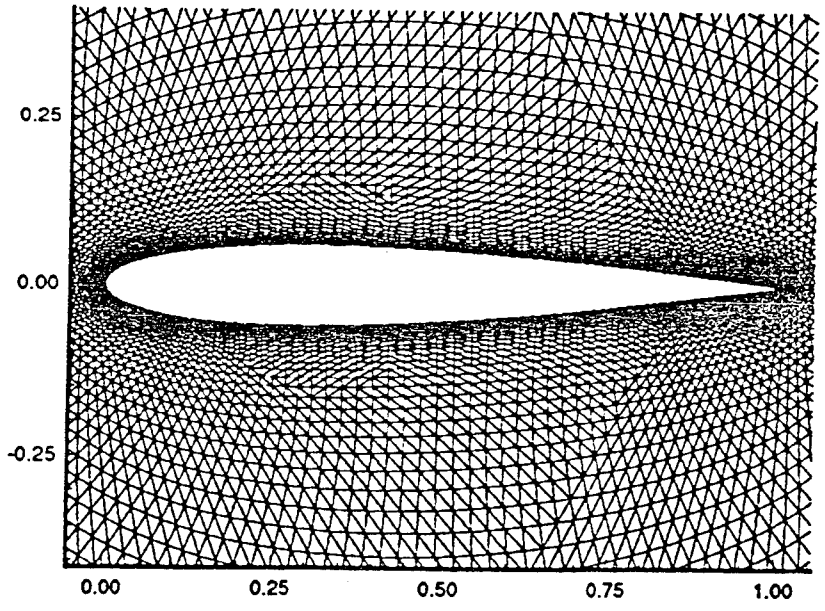

Figure 8: Unstructured grid of triangles

Table 1: Family of Implicit Algorithms

Type	*Accuracy*	α	β
Euler	$\mathcal{O}(\Delta t)$	0	1
Trapezoidal	$\mathcal{O}(\Delta t^2)$	0	$\frac{1}{2}$
3-point	$\mathcal{O}(\Delta t^2)$	$\frac{1}{2}$	1

cell i. Note that the Einstein summation convention is *not* employed in eqn. (67). The family of algorithms and the associated temporal accuracy is indicated in Table 1.

The increments ΔQ_i for the N cells can be concatenated

$$\Delta \mathcal{Q} = (\Delta Q_1, \Delta Q_2, \ldots, \Delta Q_N)^T \tag{69}$$

based on an assumed ordering of the cells. Application of eqn. (67) to each cell, together with suitable boundary conditions, yields the linear system of equations,

$$\mathcal{A}\,\Delta \mathcal{Q} = \mathcal{R} \tag{70}$$

where $\mathcal{A}$ is the generalized Jacobian matrix, and $\mathcal{R}$ is the residual. The Jacobian $\mathcal{A}$ is

sparse and banded.

5.2 Inviscid Fluxes

The contribution to C_i from the inviscid fluxes is obtained from flux difference split method of Roe [34]

$$\int_{\partial V_i} (F_{inv}\, dy - G_{inv}\, dx) = \sum_{k=1}^{k=3} T^{-1} H \Delta s \tag{71}$$

where the rotation matrix is

$$T^{-1}\Delta s = \begin{Bmatrix} \Delta x & 0 & 0 & 0 \\ 0 & \Delta y & \Delta x & 0 \\ 0 & -\Delta x & \Delta y & 0 \\ 0 & 0 & 0 & \Delta s \end{Bmatrix} \tag{72}$$

where Δx and Δy are the $x-$ and $y-$ projections of side k of cell i and $\Delta s^2 = \Delta x^2 + \Delta y^2$. The flux vector is

$$H = \begin{Bmatrix} \rho \bar{U} \\ \rho \bar{U} \bar{u} + p \\ \rho \bar{v} \bar{U} \\ \rho e \bar{U} + p \bar{u} \end{Bmatrix} \tag{73}$$

where

$$\begin{aligned} \bar{u} &= u\frac{\Delta y}{\Delta s} - v\frac{\Delta x}{\Delta s} \\ \bar{v} &= u\frac{\Delta x}{\Delta s} + v\frac{\Delta y}{\Delta s} \\ \bar{U} &= U\frac{\Delta y}{\Delta s} - V\frac{\Delta x}{\Delta s} \end{aligned} \tag{74}$$

The flux vector H on a face k of a triangle is approximated by

$$H = \tfrac{1}{2}\left(H_l + H_r + \tilde{S}|\tilde{\Lambda}|\tilde{S}^{-1}\Delta R\right) \tag{75}$$

The terms H_l and H_r denote the "left" and "right" reconstructed values of the flux vector corresponding to the inside surface (*i.e.*, inside the triangle) and outside surface

of face k. These values are obtained by a spatially second-order accurate reconstruction of Q using the cell-centered values [57]

$$Q = Q_i + \Phi \nabla Q \cdot \vec{r} \tag{76}$$

where Q_i denotes the value of Q at the cell centroid, $\vec{r}$ is the vector from the cell centroid to the midpoint on the face, and Φ is a limiter function [57] which is determined by the requirement that the reconstructed value of Q at the cell face is within the range of values of Q for those cells employed in the reconstruction. The gradient ∇Q at the cell centroid is obtained from Green's Theorem using the dual triangle abc whose vertices are the centroids of the cells adjacent to cell i (Fig. 9). Thus,

$$Q = Q_i + \Phi \left(\Delta Q_a + \Delta Q_b + \Delta Q_c \right) \tag{77}$$

where

$$\begin{aligned}
\Delta Q_a &= \frac{1}{2V_{abc}} \left(Q_b + Q_c \right) \vec{n}_a \cdot \vec{r} ds \\
\Delta Q_b &= \frac{1}{2V_{abc}} \left(Q_a + Q_c \right) \vec{n}_b \cdot \vec{r} ds \\
\Delta Q_c &= \frac{1}{2V_{abc}} \left(Q_b + Q_a \right) \vec{n}_c \cdot \vec{r} ds
\end{aligned} \tag{78}$$

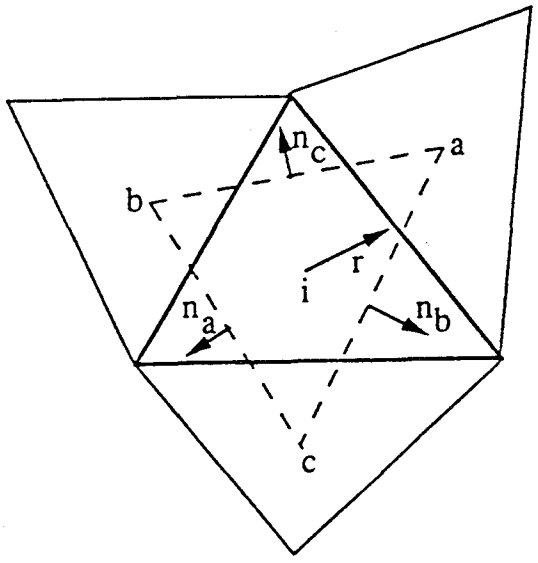

Figure 9: Triangle used to construct ∇Q

The additional term in eqn. (75) represents the contribution to the flux vector from the waves originating within the adjacent cells and may be written,

$$\tilde{S}|\tilde{\Lambda}|\tilde{S}^{-1}\Delta R = \sum_{j=1}^{j=4} \tilde{\alpha}_j |\tilde{\lambda}_j| \tilde{e}_j \tag{79}$$

where $|\tilde{\lambda}_j|$ are the absolute values of the eigenvalues

$$\begin{aligned} \tilde{\lambda}_1 &= \tilde{\bar{U}} \\ \tilde{\lambda}_2 &= \tilde{\bar{U}} \\ \tilde{\lambda}_3 &= \tilde{\bar{U}} + \tilde{a} \\ \tilde{\lambda}_4 &= \tilde{\bar{U}} - \tilde{a} \end{aligned} \tag{80}$$

The Roe-averaged variables are

$$\begin{aligned} \tilde{\bar{U}} &= \frac{\sqrt{\rho_l}\,\bar{U}_l + \sqrt{\rho_r}\,\bar{U}_r}{\sqrt{\rho_l} + \sqrt{\rho_r}} \\ \tilde{\bar{u}} &= \frac{\sqrt{\rho_l}\,\bar{u}_l + \sqrt{\rho_r}\,\bar{u}_r}{\sqrt{\rho_l} + \sqrt{\rho_r}} \\ \tilde{\bar{v}} &= \frac{\sqrt{\rho_l}\,\bar{v}_l + \sqrt{\rho_r}\,\bar{v}_r}{\sqrt{\rho_l} + \sqrt{\rho_r}} \\ \tilde{H} &= \frac{\sqrt{\rho_l}\,H_l + \sqrt{\rho_r}\,H_r}{\sqrt{\rho_l} + \sqrt{\rho_r}} \\ \tilde{a}^2 &= (\gamma - 1)\left(\tilde{H} - \tilde{q}\right) \\ \tilde{q} &= \tfrac{1}{2}\left(\tilde{\bar{u}}^2 + \tilde{\bar{v}}^2\right) \end{aligned} \tag{81}$$

The eigenvectors are

$$\tilde{e}_1 = \begin{Bmatrix} 0 \\ 0 \\ \tilde{\bar{v}} \\ \tilde{\bar{v}}^2 \end{Bmatrix}, \tilde{e}_2 = \begin{Bmatrix} 1 \\ \tilde{\bar{u}} \\ \tilde{\bar{v}} \\ \tilde{q} \end{Bmatrix}$$

$$\tilde{e}_3 = \begin{Bmatrix} 1 \\ \tilde{\bar{u}} + \tilde{a} \\ \tilde{\bar{v}} \\ \tilde{H} + \tilde{\bar{u}}\tilde{a} \end{Bmatrix}, \tilde{e}_4 = \begin{Bmatrix} 1 \\ \tilde{\bar{u}} - \tilde{a} \\ \tilde{\bar{v}} \\ \tilde{H} - \tilde{\bar{u}}\tilde{a} \end{Bmatrix} \tag{82}$$

The coefficients are

$$\begin{aligned}
\tilde{\alpha}_1 &= -\Delta\rho + \frac{1}{\tilde{\bar{v}}}\Delta\rho\bar{v} \\
\tilde{\alpha}_2 &= \left\{1 - \frac{\gamma-1}{2\tilde{a}^2}\left(\tilde{\bar{u}}^2 + \tilde{\bar{v}}^2\right)\right\}\Delta\rho + \\
&\quad (\gamma-1)\frac{\tilde{\bar{u}}}{\tilde{a}^2}\Delta\rho\bar{u} + (\gamma-1)\frac{\tilde{\bar{v}}}{\tilde{a}^2}\Delta\rho\bar{v} \\
&\quad -\frac{\gamma-1}{\tilde{a}^2}\Delta\rho e \\
\tilde{\alpha}_3 &= \left\{\frac{\gamma-1}{4\tilde{a}^2}\left(\tilde{\bar{u}}^2 + \tilde{\bar{v}}^2\right) - \frac{\tilde{\bar{u}}}{2\tilde{a}}\right\}\Delta\rho \\
&\quad + \left\{-\frac{\gamma-1}{2}\frac{\tilde{\bar{u}}}{\tilde{a}^2} + \frac{1}{2\tilde{a}}\right\}\Delta\rho\bar{u} \\
&\quad -\frac{\gamma-1}{2}\frac{\tilde{\bar{v}}}{\tilde{a}^2}\Delta\rho\bar{v} + \frac{\gamma-1}{2\tilde{a}^2}\Delta\rho e \\
\tilde{\alpha}_4 &= \tilde{\alpha}_3 + \frac{\tilde{\bar{u}}}{\tilde{a}}\Delta\rho - \frac{1}{\tilde{a}}\Delta\rho\bar{u}
\end{aligned} \tag{83}$$

where, for example, $\Delta\rho\bar{u} = \rho\bar{u}_l - \rho\bar{u}_r$.

An entropy cut-off is employed to eliminate unphysical expansion shocks which can occur when one or more of the eigenvalues $\tilde{\lambda}_j$ are zero. In eqn. (79), $|\tilde{\lambda}_j|$ is replaced by $\| \tilde{\lambda}_j \|$ where

$$\| \tilde{\lambda}_j \| = \begin{cases} |\tilde{\lambda}_j| & \text{if } |\tilde{\lambda}_j| > \delta \\ \left(|\tilde{\lambda}_j|^2 + \delta^2\right)/2\delta & \text{if } |\tilde{\lambda}_j| \leq \delta \end{cases} \tag{84}$$

where δ is a small quantity (typically, $\delta \leq 0.1$).

The individual elements of the additional flux term $\tilde{S}|\tilde{\Lambda}|\tilde{S}^{-1}\Delta R$ are given in Appendix D.

5.3 Viscous Fluxes

The contribution to C_i from the viscous fluxes and heat transfer on face k is obtained from application of Gauss' Theorem [22] to the quadrilateral defined by the cell centroids of the cells adjacent to face k and the two nodes defining the endpoints (Fig. 10). For any function $f(x, y)$,

$$\frac{\partial f}{\partial x} = \frac{1}{V}\int_{\partial V} f n_x dA \tag{85}$$

where V and ∂V are the volume and surface of the quadrilateral $abcd$, respectively, and n_x is the component of the outwards normal in the $x-$direction. A similar equation is obtained for $\partial f/\partial y$. The molecular viscosity is evaluated at the midpoint of surface k using the formula

$$\mu = \tfrac{1}{2}(\mu_b + \mu_d) \tag{86}$$

where μ_b and μ_d represent the molecular viscosity evaluated at nodes b and d, respectively.

The values of Q at the nodes are needed only for the viscous terms and are obtained by second-order interpolation of Q from those cells sharing the node [33]

$$Q_j = \sum_{cells} w_i Q_i / \sum_{cells} w_i \tag{87}$$

where Q_j denotes the Q at node j, Q_i denotes Q at the centroid of cell i which shares the node j, the sum is over all cells sharing the node (x_j, y_j), and w_i are dimensionless weights

$$w_i = 1 + \lambda_x (x_i - x_j) + \lambda_y (y_i - y_j) \tag{88}$$

where

$$\begin{aligned}
\lambda_x &= (I_{xy}R_y - I_{yy}R_x) / \left(I_{xx}I_{yy} - I_{xy}^2\right) \\
\lambda_y &= (I_{xy}R_x - I_{xx}R_y) / \left(I_{xx}I_{yy} - I_{xy}^2\right) \\
R_x &= \sum_{cells}(x_i - x_j), R_y = \sum_{cells}(y_i - y_j) \\
I_{xx} &= \sum_{cells}(x_i - x_j)^2, I_{yy} = \sum_{cells}(y_i - y_j)^2 \\
I_{xy} &= \sum_{cells}(x_i - x_j)(y_i - y_j)
\end{aligned} \tag{89}$$

5.4 Jacobian of Inviscid Terms

The exact expression for the individual Jacobians of the inviscid terms in eqn. (67) is

$$\left.\frac{\partial C_i}{\partial Q_j}\right|_{inv} = \sum_{k=1}^{k=3}\{A_l + B_l + C\}\frac{\partial Q_l}{\partial Q_j} + \sum_{k=1}^{k=3}\{A_r + B_r - C\}\frac{\partial Q_r}{\partial Q_j} \tag{90}$$

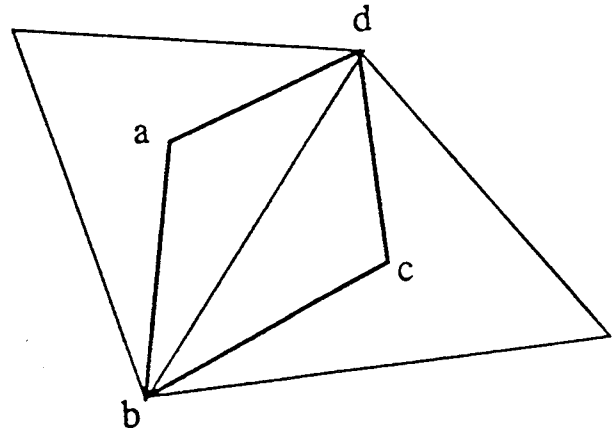

Figure 10: Quadrilateral employed for determination of viscous fluxes and heat transfer

where

$$\begin{aligned} A_l &= \tfrac{1}{2} T^{-1} \frac{\partial H_l}{\partial Q_l} \Delta s \\ A_r &= \tfrac{1}{2} T^{-1} \frac{\partial H_r}{\partial Q_r} \Delta s \\ B_l &= \frac{\partial C}{\partial Q_l} (Q_l - Q_r) \\ B_r &= \frac{\partial C}{\partial Q_r} (Q_l - Q_r) \\ C &= \tfrac{1}{2} T^{-1} \tilde{S} |\Lambda| \tilde{S}^{-1} T \Delta s \end{aligned} \tag{91}$$

Complete details of the exact inviscid Jacobian are provided in Appendix D.

5.5 Jacobian of Viscous Terms

The exact expression for the individual Jacobians of the viscous terms in eqn. (67) is

$$\left. \frac{\partial C_i}{\partial Q_j} \right|_{vis} = \sum_{k=1}^{k=3} \frac{\partial N}{\partial Q_j} \tag{92}$$

where

$$N = \begin{Bmatrix} 0 \\ -\tau_{xx} \Delta y + \tau_{xy} \Delta x \\ -\tau_{xy} \Delta y + \tau_{yy} \Delta x \\ \beta_x \Delta y - \beta_y \Delta x \end{Bmatrix} \tag{93}$$

Complete details of the exact viscous Jacobian are provided in Appendix D.

5.6 Boundary Conditions

Boundary conditions are incorporated implicitly. At a supersonic inflow boundary, Q is specified fully. At a solid boundary, the velocity is set equal to zero, the surface temperature or heat flux (*e.g.*, adiabatic) is specified, and the normal derivative of the static pressure is set to zero. On a symmetry boundary, the normal component of the velocity is set to zero, and the normal gradients of the remaining flow variables are set to zero. At a supersonic outflow boundary, the flow variables are extrapolated linearly from the interior.

5.7 Solution of Linear System

The linear system eqn. (70) is solved at each time step using the BiCGSTAB algorithm of Van der Vorst [46]. The algorithm is a conjugate gradient type iterative method.

6 CODE VALIDATION (STRUCTURED GRID)

A two-dimensional, laminar, compressible Navier-Stokes solver has been developed employing the Beam-Warming algorithm described in section 3. A variety of two-dimensional test computations were performed to establish the accuracy of the solver. The solver was validated through application to the following computations :

(a) Flat plate boundary layer.

(b) Steady state laminar flow past a NACA-0012 airfoil.

(c) Unsteady laminar flow past a pitching NACA-0015 airfoil.

6.1 Flat Plate Boundary Layer

The supersonic laminar boundary layer on a flat plate provides a test of the accuracy of the solver for viscous flows by comparison with an exact solution of the boundary layer equations under the conditions $Pr = 1$, and $\mu = T$. The solver was employed to perform a boundary layer computation over a flat plate. The freestream Mach number M_∞ was 2.0 and Reynolds number based on the length of the plate (Re_L) was selected to be 10^4.

The computational configuration is shown in Fig. (11). The inflow is a uniform steady flow and extrapolation was used to find the flow variables at the outflow. The Method of Characteristics was used at the top boundary. At the lower boundary, in front of the plate leading edge, a symmetry boundary condition was used for the flow variables in the η-direction (i.e., $\frac{\partial}{\partial \eta}(\ ) = 0$). At the plate boundary, a no-slip, adiabatic boundary condition was used for the velocity and temperature, respectively. A linear viscosity law was employed with $Pr = 1.0$.

$$\frac{\mu}{\mu_\infty} = \frac{T}{T_\infty} \tag{94}$$

where the subscript ∞ denotes the freestream values.

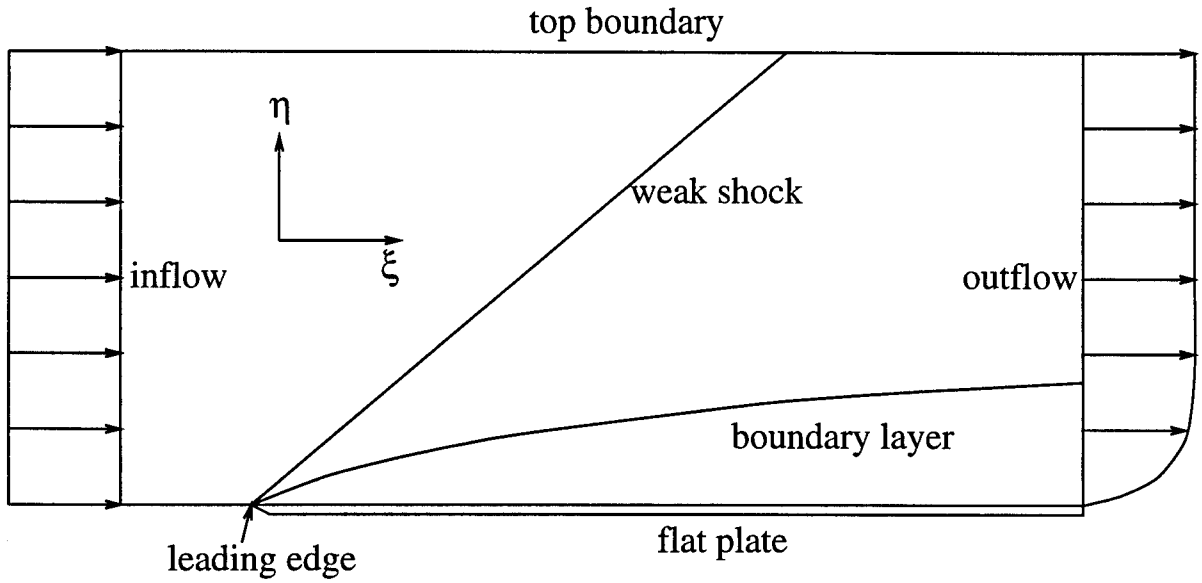

Figure 11: Schematic of the computational domain for boundary layer over a flat plate.

The grid employed $N_\xi = 60$ and $N_\eta = 75$ points in the streamwise (ξ) and normal (η) directions, respectively. The number of grid points within the boundary layer was $N_{BL} = 54$ at the end of the flat plate.

The computed velocity and static temperature profiles are compared with the available analytical profiles [56] in Figures (12) and (13) at $x = 0.8L$. The ordinate is the transformed distance in η direction:

$$\eta^+ = \sqrt{\frac{Re_x}{2}} \int_0^y \frac{\rho}{\rho_\infty} \frac{dy}{x} \tag{95}$$

The velocity is normalized by the freestream velocity, U_∞, and the static temperature is normalized by the freestream static temperature, T_∞. The agreement between the computation and the theory is excellent. The computed velocity and static temperature profiles agreed with the analytical profiles to within 1.0%.

A computation was also performed with the grid at an angle to the horizontal. The results showed similar agreement with the theory as in the previous case. This computation ascertained the accuracy of the grid transformation from (x, y) coordinates to (ξ, η) coordinates.

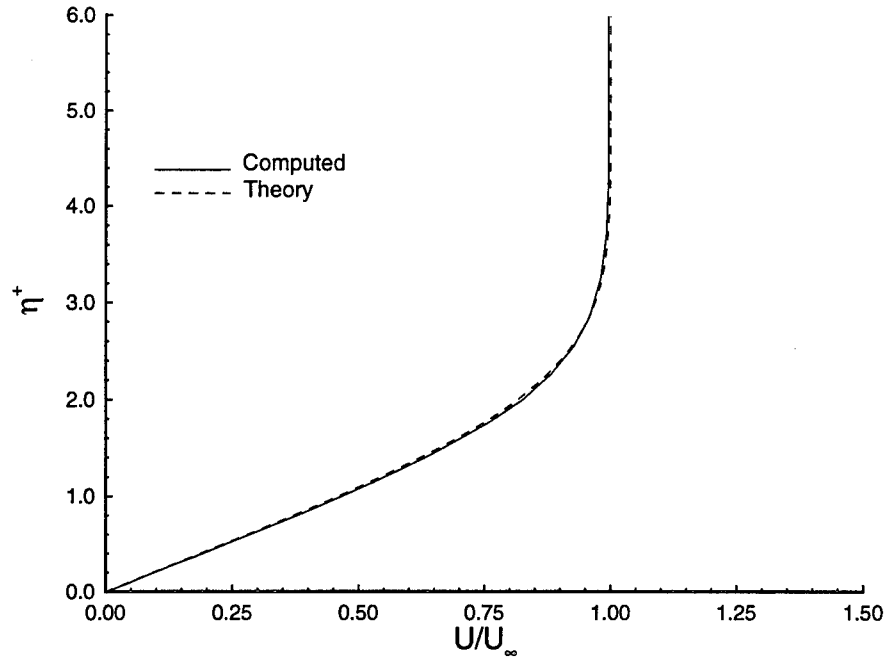

Figure 12: Velocity profile in the boundary layer over a flat plate ($Re_L = 10^4$, $M_\infty = 2.0$).

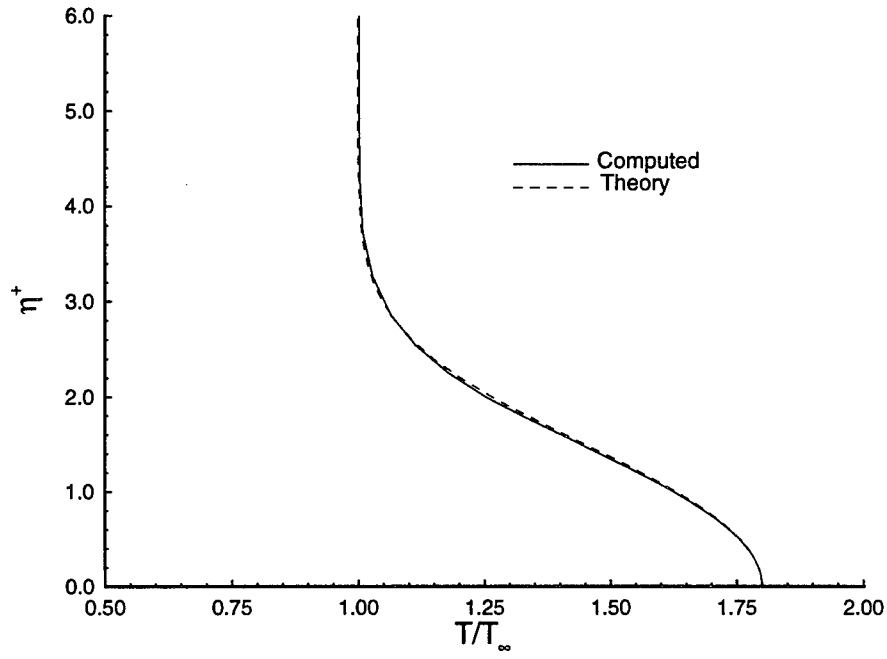

Figure 13: Static temperature profile in the boundary layer over a flat plate ($Re_L = 10^4$, $M_\infty = 2.0$).

6.2 Steady Flow Past a Stationary NACA-0012 Airfoil

The viscous subsonic flow past an airfoil at a fixed angle provides a realistic test of the accuracy of the numerical algorithm by comparison with previous numerical computations.

A series of computations were performed for a stationary NACA-0012 airfoil at an angle of attack, $\alpha = 0°$, Reynolds number based on the chord $Re_c = 5 \times 10^3$, and freestream Mach number $M_\infty = 0.2$. Sutherland's Law was employed, and $Pr = 0.73$. A C-grid was employed with $N_\xi = 303$ and $N_\eta = 101$, where ξ is the curvilinear coordinate in the direction of the "C", and η is the coordinate approximately orthogonal to η. The average normal distance of the first row of mesh points adjacent to the airfoil was $\Delta n_{aver} = 5.0 \times 10^{-4} c$, and 25 grid points were contained within the boundary layer at mid-chord. The grid spacing tangential to the airfoil surface varied from $\Delta s = 4.3 \times 10^{-4} c$ to $1.99 \times 10^{-2} c$, with the finest grid employed near the leading and trailing edges.

The results were compared with previous computations by Beran [3] and the results utilizing the present unstructured grid algorithm [20] at the same flow field conditions, and Mehta [26] at the same Reynolds number for incompressible flow. Table 2 presents the computed drag coefficient of the present study and the three other computations. Figure 14 shows the comparison of the computed surface pressure coefficient with Beran's results. The computed drag coefficient and surface pressure coefficient show close agreement with the other computations.

Table 2: Computed Drag Coefficient (Stationary NACA-0012 Airfoil), $Re_c = 5 \times 10^3$, $M_\infty = 0.2$, $\alpha = 0°$.

Reference	*drag coefficient* (c_d)
Present study (Structured grid)	0.0544
Beran	0.0530
Present study (Unstructured grid)	0.0547
Mehta	0.0534

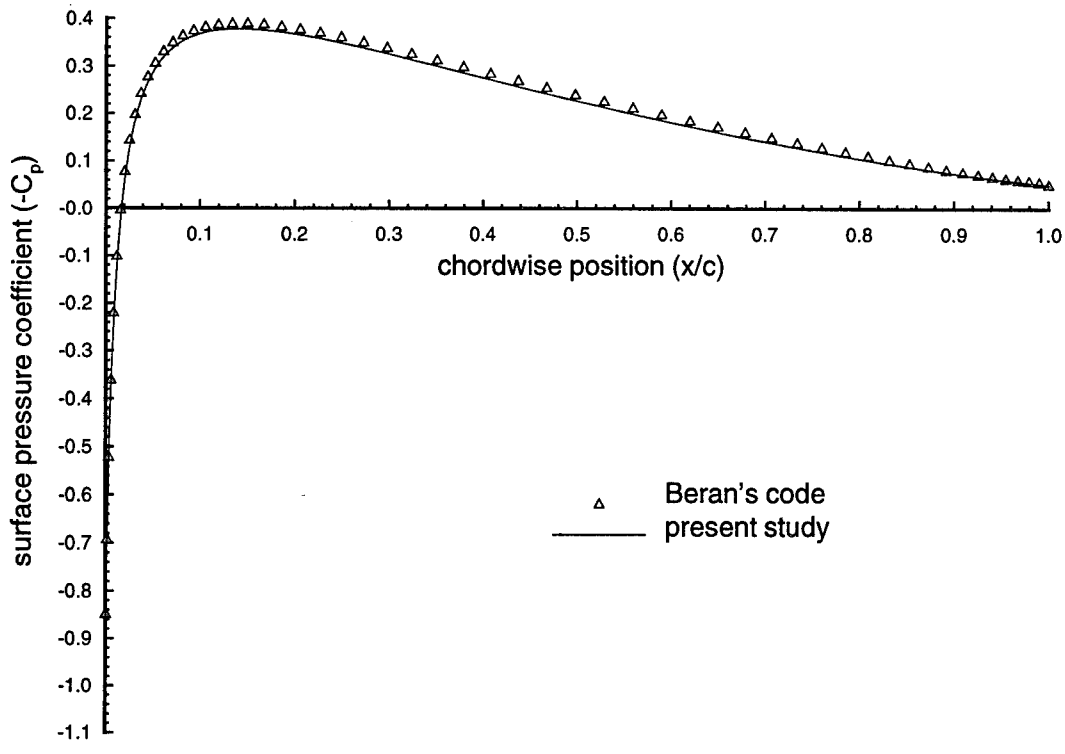

Figure 14: Pressure coefficient on the surface of a stationary NACA-0012 airfoil at $\alpha = 0°$ ($Re_c = 5 \times 10^3$, $M_\infty = 0.2$).

The Beam-Warming algorithm has artificial damping terms. It is important to study the effect of the damping coefficients on the computations. A number of computations were performed to study the sensitivity of the computed flowfield to the magnitude of the explicit damping coefficient, ω_e. The steady solutions do not depend on the magnitude of the implicit dissipation terms because at steady state the right hand side of equations 39 and 40 are zero and the implicit dissipation term does not have any effect on the final solution. The computed flowfield was found to be insensitive to the magnitude of the explicit damping coefficient ω_e provided $\omega_e < 0.01$. Figure (15) shows the values of the drag coefficient and leading edge pressure coefficient for different values of explicit damping coefficient.

The effect of the location of the outer boundary distance from the airfoil on the computed flowfield was also studied. Figure (16) shows that the computed drag coefficient and leading edge pressure coefficient are insensitive to the location of the outer boundary provided the distance from the airfoil exceeds $18c$.

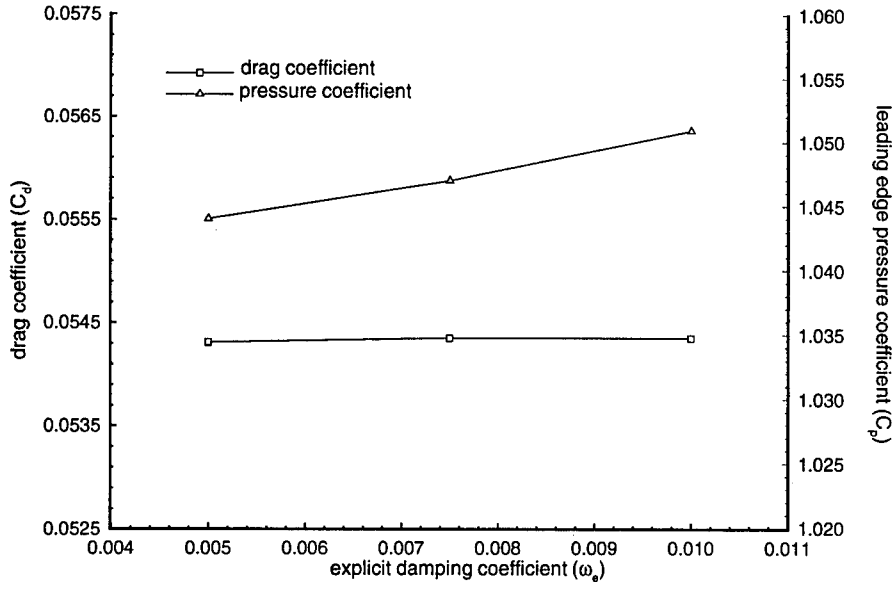

Figure 15: Effect of explicit damping coefficient, ω_e, on the drag coefficient and leading edge pressure coefficient for a stationary NACA-0012 airfoil at $\alpha = 0°$ ($Re_c = 5 \times 10^3$, $M_\infty = 0.2$).

6.3 Unsteady Flow Past a Pitching NACA-0015 Airfoil

The subsonic viscous unsteady flow past a pitching airfoil provides a test of the temporal and spatial accuracy of the numerical algorithm through comparison with previous numerical simulations.

A set of computations were performed to study the flow past an NACA-0015 airfoil pitching about its quarter chord axis at $Re_c = 10^4$, $M_\infty = 0.2$, and non-dimensional pitch rate $\Omega_o^+ = 0.2$. The pitching motion was defined by :

$$\Omega^+(t) = \Omega_o^+ \left(1 - e^{\left\{\frac{-4.6t}{t_o}\right\}}\right) \tag{96}$$

where t_o is the time at which the non-dimensional pitch rate Ω^+ has reached 99% of its

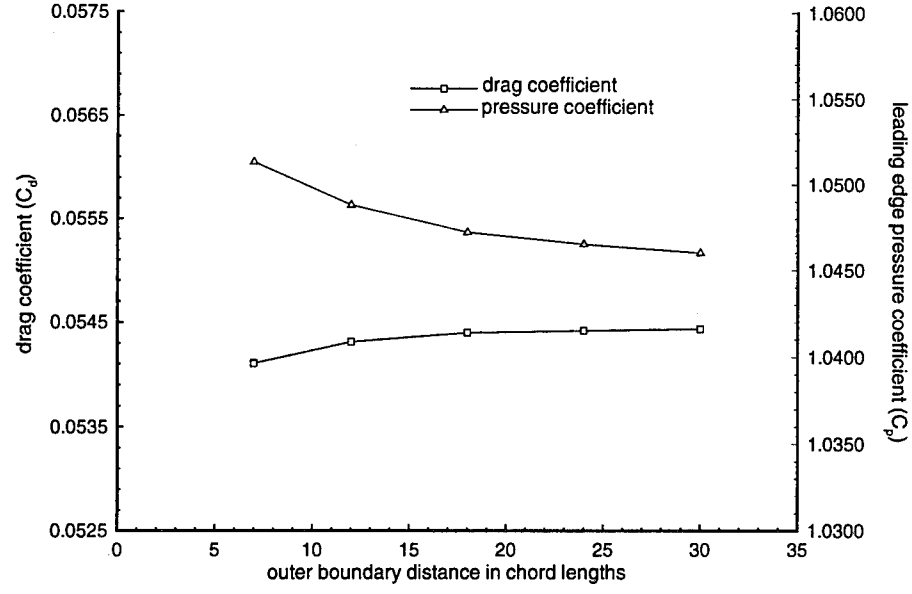

Figure 16: Effect of the location of the outer boundary distance from the airfoil on the drag coefficient and leading edge pressure coefficient for a stationary NACA-0012 airfoil at $\alpha = 0°$ ($Re_c = 5 \times 10^3$, $M_\infty = 0.2$).

asymptotic value, Ω_o^+. The non-dimensional pitch rate is defined as :

$$\Omega^+ = \frac{\Omega c}{U_\infty} \tag{97}$$

where Ω is the pitching rate in rad/sec, c is the chord length and U_∞ is the freestream velocity. The functional form of the non-dimensional pitch rate provides a smooth acceleration of the airfoil to its asymptotic value during an effective time interval $t_o = 0.5c/U_\infty$ which corresponds to 4.57° of pitch. The functional form of the pitching motion also removes the infinite acceleration faced at the start of the pitching if a constant value of Ω^+ is applied throughout the motion. The flow condition and expression for the pitching motion correspond to the previous computation by Visbal [49].

A C-grid was employed with $N_\xi = 332$ and $N_\eta = 85$. The average normal distance of the first row of mesh points adjacent to the airfoil was $\Delta n_{aver} = 1.0 \times 10^{-4} c$, and 33 grid points were contained within the boundary layer at mid-chord. The grid spacing

tangential to the airfoil surface varied from $\Delta s = 4.59 \times 10^{-3}c$ to $1.47 \times 10^{-2}c$, with the finest grid employed near the leading and trailing edges.

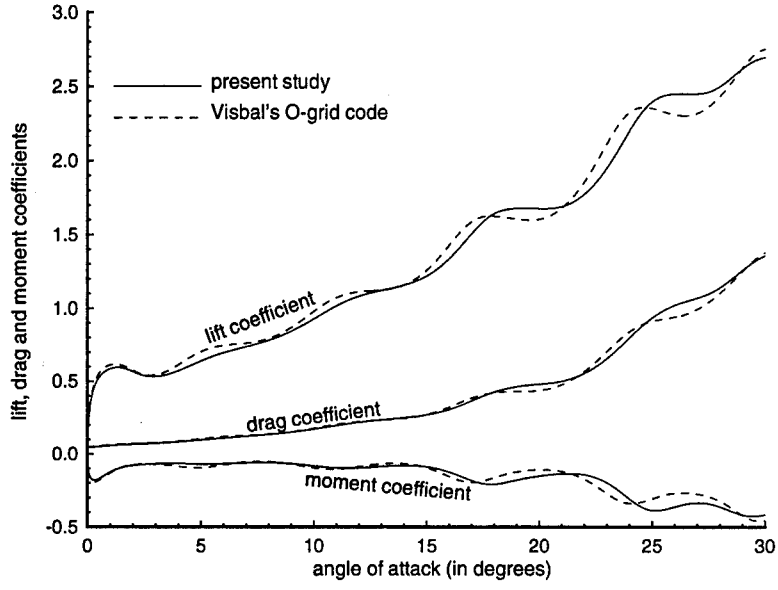

Figure 17: Lift, drag and moment coefficients for a pitching NACA-0015 airfoil ($Re_c = 10^4$, $M_\infty = 0.2$, $\Omega_o^+ = 0.2$).

The computed flowfields were found to be in close agreement with the previous computation by Visbal [49], who used an O-grid. Figure (17) shows the comparison of the computed lift coefficient C_l, drag coefficient C_d, and moment coefficient C_M with the previous results of Visbal for $0 < \alpha < 25°$, where α is the angle of attack of the airfoil. Detailed examination of the flow variables showed similar close agreement.

7 CODE VALIDATION (UNSTRUCTURED GRID)

7.1 Riemann Shock Tube

The Riemann Shock Tube Problem provides a test of the temporal and spatial accuracy of the numerical algorithm for inviscid flows through comparison with an exact solution [21]. A total of four rows of 200 triangular cells each were employed with cell spacing $\Delta x = \Delta y = 1.0$. The pressure ratio $p_4/p_1 = 10$, where p_4 and p_1 are the static pressure in the driver and driven sections, respectively. The static temperature ratio $T_4/T_1 = 1.0$. The diaphragm is located in the middle of the computational domain. The computations employed trapezoidal time differencing with a Courant number of 2. The entropy cut-off $\delta = 0.1$.

Results for the static pressure, static temperature and velocity are shown in Figs. 18 through 20 at $t = 18.4$. The computed profiles are in close agreement with the exact result [21].

7.2 Flat Plate Boundary Layer

The supersonic laminar boundary layer on a flat plate provides a test of the spatial accuracy of the numerical algorithm for viscous flows through comparison with an exact solution of the boundary layer equations under the conditions $Pr = 1$ and $\mu = T$ [56]. A total of 7802 triangular cells were utilized comprising 47 rows of 166 cells each. The streamwise cell length $\Delta x = 1.28 \times 10^{-2}$. The transverse cell length Δy varied from 1.0065×10^{-3} adjacent to the flat plate to 2.07×10^{-2} at the upper boundary of the computational domain. The Reynolds number Re_∞ based on plate length was 3.95×10^4.

The computed and theoretical velocity and static temperature profiles are displayed

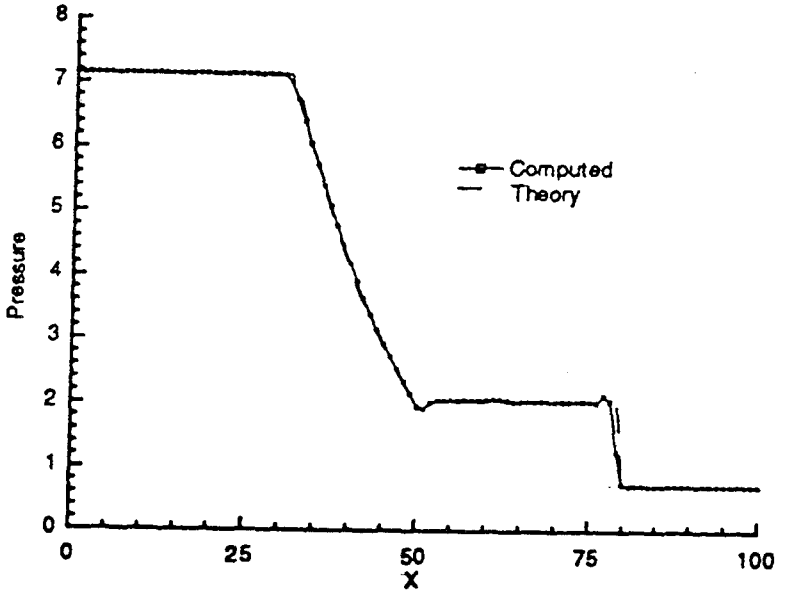

Figure 18: Comparison of static pressure in a shock tube

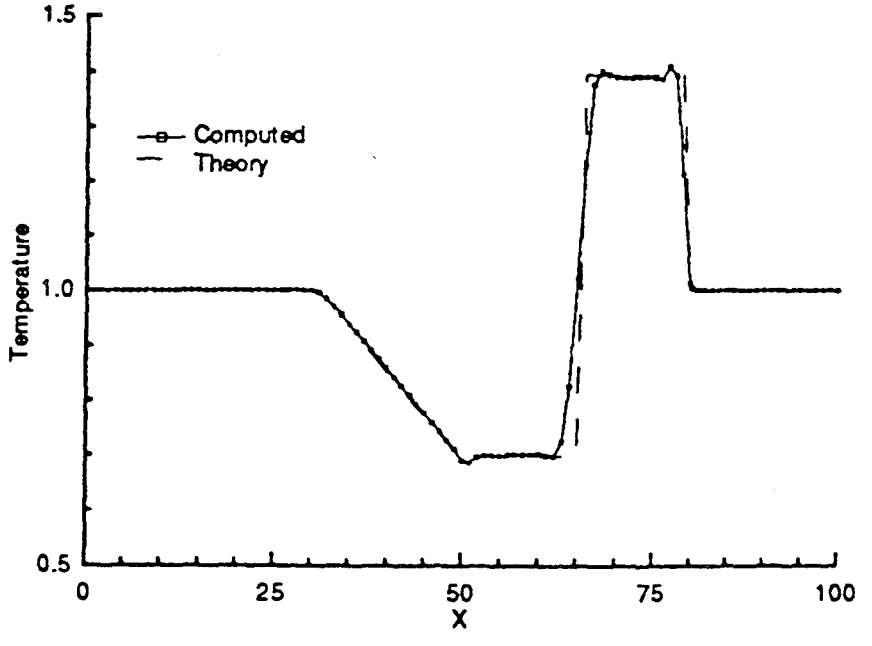

Figure 19: Comparison of static temperature in a shock tube

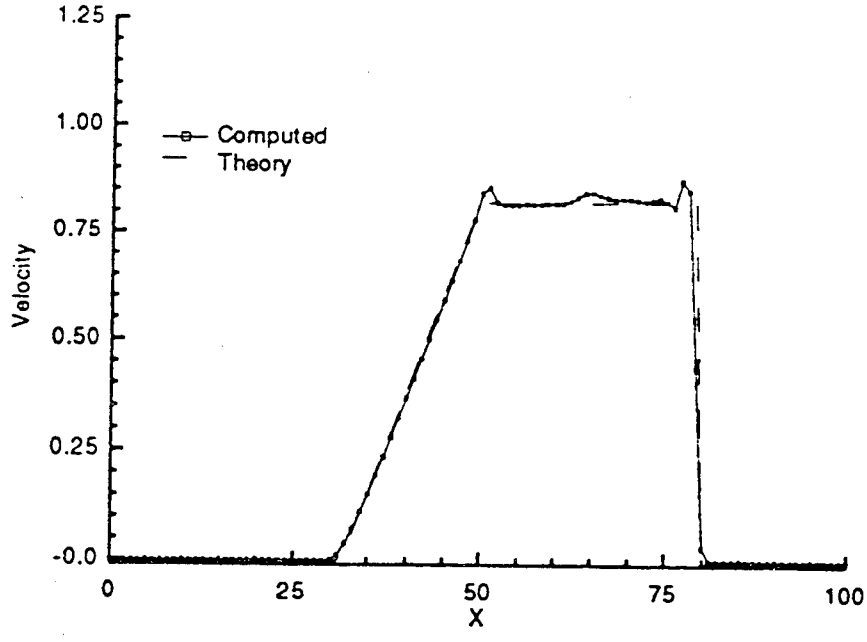

Figure 20: Comparison of velocity in a shock tube

in Figs. 21 and 22, respectively. The ordinate is the transformed dimensionless distance

$$\eta = Y\sqrt{\frac{Re_\infty}{2x}}, \; Y = \int_0^y \rho dy \tag{98}$$

The velocity is normalized by the freestream speed of sound (and hence $u_\infty = M_\infty$), and the static temperature is normalized by the freestream static temperature. The agreement between the computation and theory is excellent. The velocity profile agrees with the theoretical result to within 1.5%. Similar close agreement is observed with the static temperature profile. In particular, the computed wall temperature agrees with the theoretical value ($T_w = 1.80$) within 0.5%.

7.3 NACA-0012 Airfoil

The subsonic viscous flow past an NACA-0012 airfoil at $\alpha = 0$ deg was computed and compared with previous numerical solutions. A total of 25,534 cells were utilized. The cell nodes were generated using the GRAPE program of Sorenson [42] and the Delaunay triangulation obtained using the UNSTRUCT program of Merriam [27]. The nodes adjacent to the airfoil surface were typically at a normal distance of $2.0 \times 10^{-3}c$ where c is

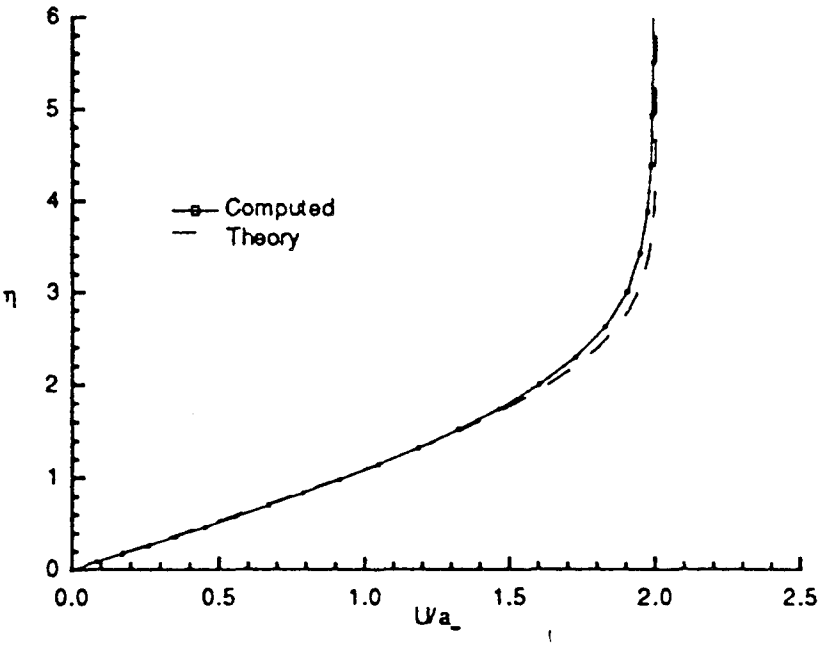

Figure 21: Comparison of velocity in the boundary layer

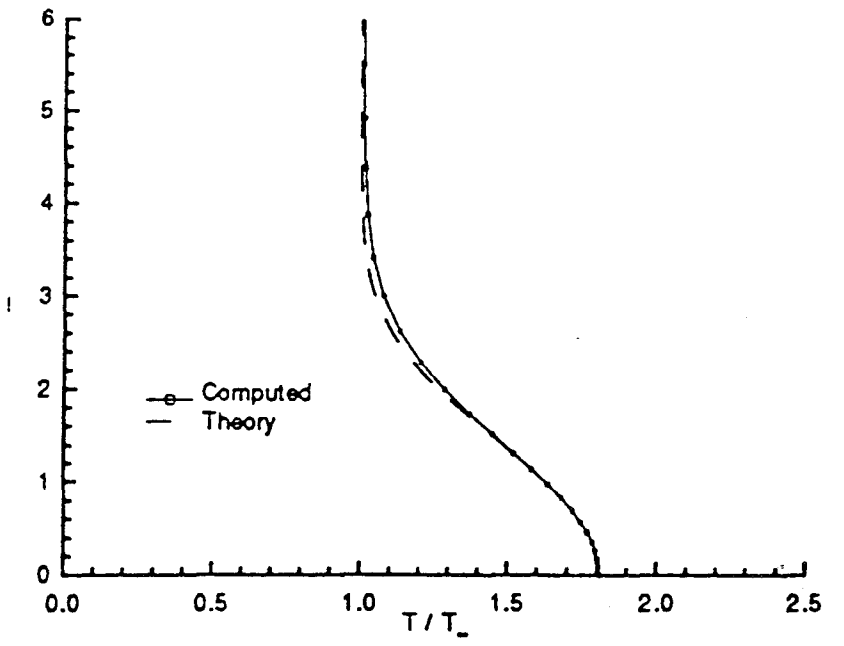

Figure 22: Comparison of static temperature in the boundary layer

the airfoil chord. The freestream Mach number $M_\infty = 0.2$ and the Reynolds Number $Re_c = 5 \times 10^3$ based on the chord.

The computed drag coefficient c_d is compared with the structured grid results, results due to Beran [3], and the results of Mehta [26] (Table 2). The flow conditions of all computations are identical, except the Mach number was zero for the computations by Mehta. The computed values of c_d are in close agreement.

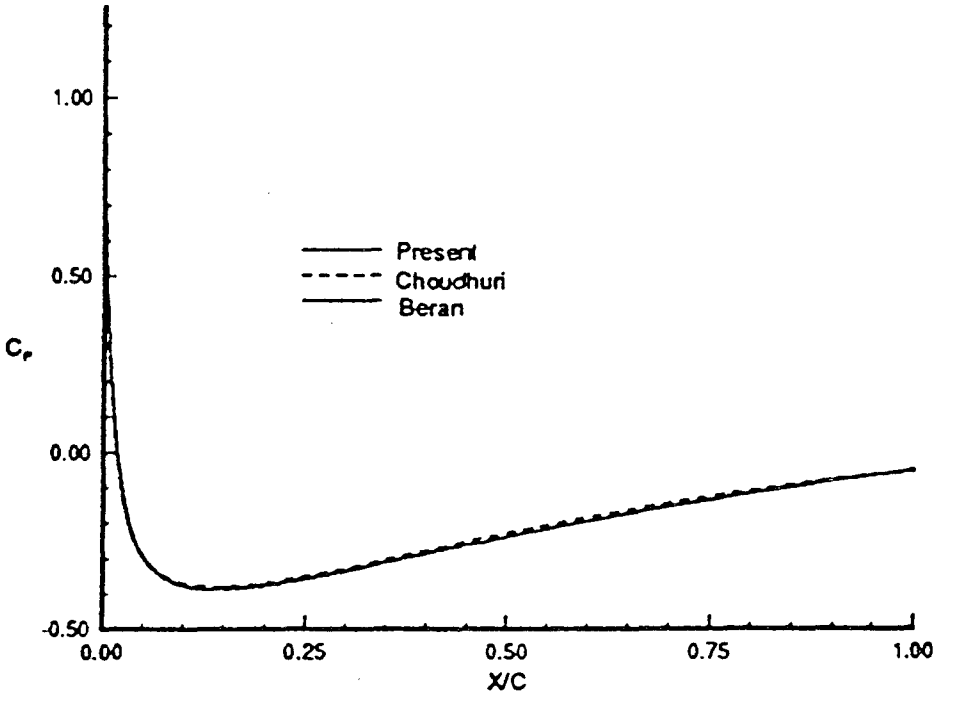

Figure 23: Comparison of surface pressure coefficient on a NACA-0012 airfoil

The computed surface pressure is shown in Fig. 23 for the present algorithm, together with the results of structured grid computation and results of Beran [3] which both employed the Beam-Warming algorithm. The agreement is excellent. The computed leading edge pressure coefficient c_p agrees with the exact (inviscid) value ($c_p = 1.01$) within 2%.

8 DEFINITION OF PROBLEM

The research problem is described in the present section. A brief description of the critical point theory follows the definition of the problem. The critical point theory has been applied to the computation of unsteady separation on a pitching airfoil to better understand the formation and development of the structures in the flowfield.

8.1 Problem Description

The focus of the research is understanding of the effects of compressibility, pitch rate and Reynolds number on the incipient boundary layer separation for viscous flow past a NACA-0012 airfoil pitching about the quarter chord axis. The flow and C-grid configurations are shown in Figure (24). The pitching motion is defined by equation (96). The pitching motion was initiated after the flowfield had been fully established at $\alpha = 0°$. The initial flowfield displayed a slight unsteadiness due to the periodic vortex shedding at the trailing edge. All computations were initiated when the lift coefficient was zero and the results presented herein are insensitive to the relative phase of the initiation of the pitching motion.

An extensive grid refinement study was conducted for each of the cases studied utilizing the structured grid algorithm to establish the accuracy of the solutions. Complete details of the grids employed for the different cases are given in Table 3. A total of 7 cases were studied (figure 2). The accuracy of the computations were assessed for each case based on the comparison of the results for two grids with successive refinement. A non-dimensional time step ($dt^+ = tU_\infty/c$) of 1.0×10^{-3} was employed for all the seven cases studied utilizing the structured grid algorithm. Computations conducted with a time step of 0.5×10^{-3} demonstrated that the computed results were insensitive to the selected time step.

One computation was performed for Case 1 using the unstructured grid algorithm for comparison with the structured grid solutions. Details of the grid are presented in

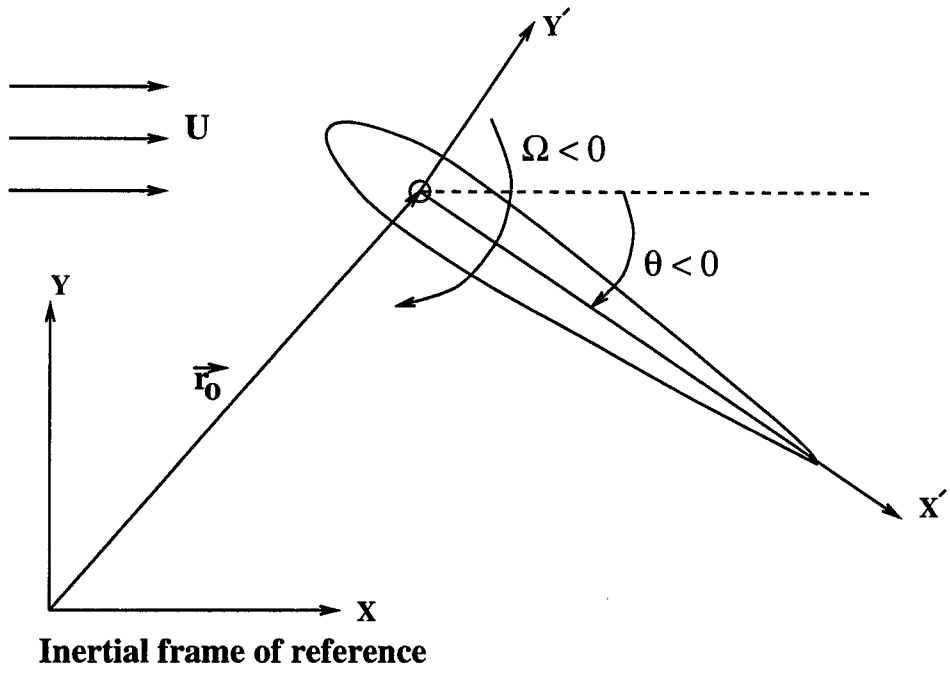

Figure 24: Pitching airfoil.

Table 3. Based on a temporal refinement study, a non-dimensional time step ($dt^+ = tU_\infty/c$) of 2.6×10^{-5} was selected for the computation.

The seven cases were chosen to study and understand the effects of compressibility, pitch rate and Reynolds number on the incipient separation process. In cases 1 through 3 and 4 through 6, the pitch rate is decreased while keeping the Reynolds and Mach numbers constant. Similarly in cases 1 and 4, 2 and 5, 3 and 6, the Mach number is increased from 0.2 to 0.5 while the Reynolds number and pitch rate are fixed. Cases 4 and 7 are computed at different Reynolds number while the Mach number and the pitch rate are fixed. These computations help in gaining an insight into several important trends related to the change in Mach number, Reynolds number or the pitch rate.

8.2 Critical Point Theory

The understanding of unsteady separation for a pitching airfoil is greatly facilitated by visualization of the *instantaneous* streamlines[3]. There are several possible frames of

[3]Of course, the instantaneous streamlines are not identical to the particle pathlines or streaklines since the flow is unsteady.

Table 3: Details of the grids

Structured Grid									
Case number	Reynolds number	Mach number	Pitch rate	Grid	N_ξ	N_η	$\Delta n/c$ x10^4	$\Delta s/c$ x10^3	N_{BL}
1	10,000	0.2	0.2	a	637	181	1.0	1.69	64
				b	1011	181	1.0	0.84	64
				c	637	325	0.5	1.69	112
2	10,000	0.2	0.1	a	1037	181	1.0	1.025	58
				b	2073	361	0.5	0.511	115
3	10,000	0.2	0.05	a	1037	181	1.0	1.025	58
				b	2073	361	0.5	0.511	115
4	10,000	0.5	0.2	a	1037	181	1.0	1.025	58
				b	2073	361	0.5	0.511	115
5	10,000	0.5	0.1	a	1037	181	1.0	1.025	58
				b	2073	361	0.5	0.511	115
6	10,000	0.5	0.05	a	2073	159	2.0	0.509	44
				b	4145	317	1.0	0.252	88
7	100,000	0.5	0.2	a	2073	337	0.05	0.509	124
				b	4145	673	0.025	0.252	247

Unstructured Grid									
Case number	Reynolds number	Mach number	Pitch rate	Grid	*icell*	*jnode*	$\Delta n/c$ x10^4	$\Delta s/c$ x10^3	N_{BL}
1	10,000	0.2	0.2	a	30,238	15,299	10.0	3.5	14

LEGEND :

N_ξ = Number of points in $\xi-$direction

N_η = Number of points in $\eta-$direction

Δn = Average normal distance of points next to airfoil

Δs = Minimum tangential distance of points on airfoil

N_{BL} = Points in BL measured normal to airfoil surface at mid-chord for $\alpha = 0°$

icell = Number of triangles

jnode = Number of nodes

reference including 1) the inertial (laboratory) frame of reference wherein the freestream velocity is fixed and the velocity at the airfoil surface is generally nonzero, and 2) the rotating frame of reference (attached to the airfoil) wherein the freestream velocity is unsteady and the velocity at the airfoil surface is zero. The rotating frame possesses the seemingly intuitive advantage for physical interpretation of "forward" and "reverse" flow relative to the airfoil. Since the velocity is zero at the airfoil surface in the rotating frame of reference, the fluid immediately adjacent to a point on the airfoil surface is either instantaneously moving "forward" (*i.e.*, towards the trailing edge) or "reverse" (*i.e.*, towards the leading edge).

The instantaneous streamlines in the rotating frame of reference were selected for analysis. The components of the velocity (u',v') in the rotating frame of reference (x',y') are related to the components of the velocity (u,v) in the inertial frame by (Fig. (24))

$$\begin{aligned} u' &= +\Omega y' + u\cos\theta + v\sin\theta \\ v' &= -\Omega x' - u\sin\theta + v\cos\theta \end{aligned} \tag{99}$$

Note that the pitch rate Ω is negative for clockwise (pitch up) rotation. The instantaneous streamlines are

$$\begin{aligned} \frac{dx'}{d\tau} &= u'(x', y', t) \\ \frac{dy'}{d\tau} &= v'(x', y', t) \end{aligned} \tag{100}$$

where τ is the parametric length along the instantaneous streamlines at a particular time.

Equation (100) is an autonomous system of ordinary differential equations which may possess critical points, *i.e.*, loci where $u' = v' = 0$. The behavior of the equations in the vicinity of these critical points is well known as described, for example, in Kaplan [17] and Pontryagin [31]. Recent papers by Perry and Chong [30] and Chong *et al* [10] have elucidated further details regarding fluid motions near critical points. The critical points may be classified on the basis of the Jacobian J and dilatation Δ where

$$J = \frac{\partial u'}{\partial x'}\frac{\partial v'}{\partial y'} - \frac{\partial u'}{\partial y'}\frac{\partial v'}{\partial x'} \tag{101}$$

$$\Delta = \frac{\partial u'}{\partial x'} + \frac{\partial v'}{\partial y'} \tag{102}$$

The taxonomy of critical points for two-dimensional flow is described in Fig. (25). For $J < 0$, the topology is a saddle, with the relative orientation of the asymptotes determined by the value of Δ. For $J > 0$ the principal topologies are nodes and foci, with the latter obtained for $J > \Delta^2/4$. The patterns are stable (*i.e.*, the instantaneous fluid motion is *towards* the critical point) or unstable (*i.e.*, the instantaneous fluid motion is *away* from the critical point) based on the sign of Δ. Positive Δ leads to unstable patterns, while negative values of Δ lead to stable patterns. In those instances where $\Delta = 0$, the topology changes from a saddle (for $J < 0$), to a simple shear (for $J = 0$) and to a center (for $J > 0$). In 2-D incompressible flows, the dilatation (Δ) is zero and only saddles and centers can occur. Centers appear in the region of positive Jacobian and saddles in the region of negative Jacobian.

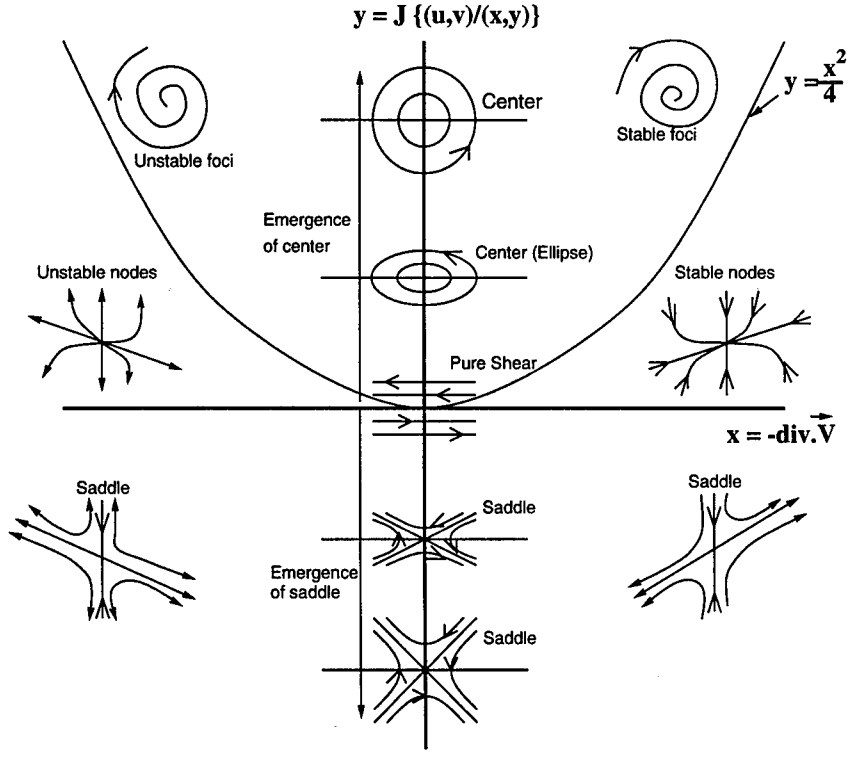

Figure 25: Classification of critical points.

The appearances of the critical points is closely related to the appearance of the recirculating regions and the development of the flow field. In the following section, critical point theory is applied to the computation of unsteady separation on a pitching airfoil.

9 RESULTS

The flow structures observed in the seven cases studied are described in the present section. A linear stability analysis was also conducted as a part of the research program to understand the reason for the formation of the recirculating regions in the flow field. The stability analysis has been presented at the end of this section.

The instantaneous streamlines obtained from the computations are presented in the following subsections. The results presented here correspond to Grid b for each of the cases (except for the unstructured grid results, which are for Grid a). The instantaneous streamlines are plotted based on a reference frame attached to the airfoil. (The instantaneous streamlines have not been plotted to scale in order to show all flow details.) The origin of the coordinate axis is the quarter chord point. The airfoil-attached reference frame allows an unambiguous definition of forward and reversed flow within a thin unseparated boundary layer, since the velocity of the fluid at the airfoil surface is zero. Forward flow is defined as fluid moving toward the trailing edge, and reversed flow indicates fluid moving toward the leading edge.

9.1 Case 1 : $Re_c = 10^4$, $M_\infty = 0.2$, $\Omega_o^+ = 0.2$ (Structured Grid)

The instantaneous streamlines at $\alpha = 14.5°$, $19.5°$, and $22.5°$ are shown in figures 26 through 28. At $\alpha = 14.5°$, the flow on the upper surface in the vicinity of the leading edge has a thin reversed flow region extending to the 7% chord position. A clockwise-rotating primary recirculating region can be seen near the leading edge on the upper surface at $\alpha = 19.5°$. The counterclockwise-rotating secondary recirculating region appears beneath the primary recirculating region and a clockwise-rotating tertiary recirculating region between the leading edge and the primary recirculating region at $\alpha = 22.5°$. The emergence of the primary recirculating region is traced to the appearance of a pair of critical points (which are defined as points in the velocity field where u=v=0 in a reference frame attached to the airfoil) within the flowfield at $\alpha = 14.99°$ at the

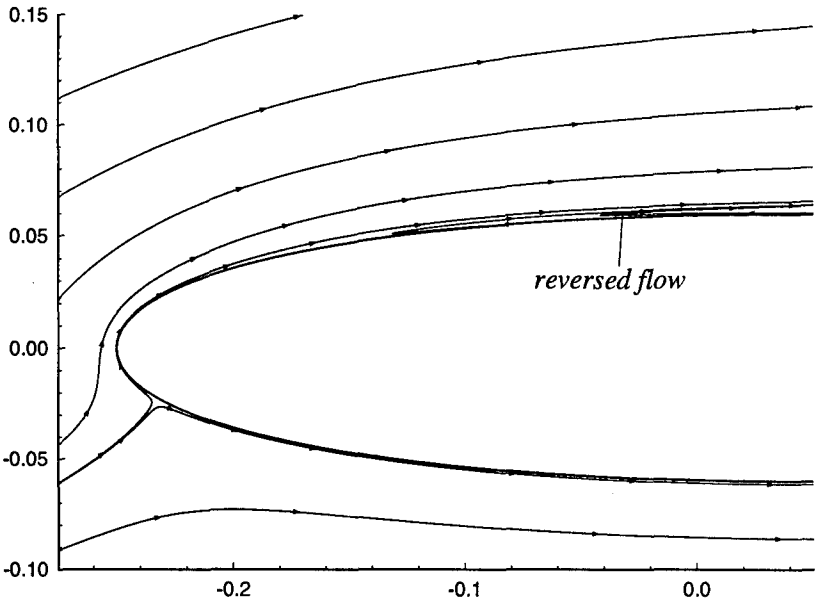

Figure 26: Instantaneous streamlines at $\alpha = 14.5°$ ($Re_c = 10^4$, $M_\infty = 0.2$, $\Omega_o^+ = 0.2$; Case 1)

18% chord location and a distance $2.5 \times 10^{-3}c$ above the airfoil surface. In figure 29, the close-up of the instantaneous streamlines at $\alpha = 15°$ show the structure of the primary recirculating region just after its birth. The instantaneous streamlines in the region between forward and reversed flow are in the shape of a "C". As α increases, one of the "C" shaped instantaneous streamlines collapses at a single point. The critical point initially appears as a single point corresponding to a pure shear, *i.e.*, $J = \Delta = 0$ (Fig. 25). It immediately bifurcates into two critical points (a *center* and a *saddle*) which move apart and the center gives rise to the *primary recirculating region.* The primary and secondary recirculating regions interact with each other to eject the fluid close to the airfoil surface in a direction approximately normal to the wall, thus leading to boundary layer separation (Peridier *et al* [28, 29]). The primary recirculating region eventually detaches from the airfoil surface and becomes the dynamic stall vortex. The developments near the leading edge are relatively isolated from the developments on the aft portion of the airfoil through a region of attached flow (figure 30).

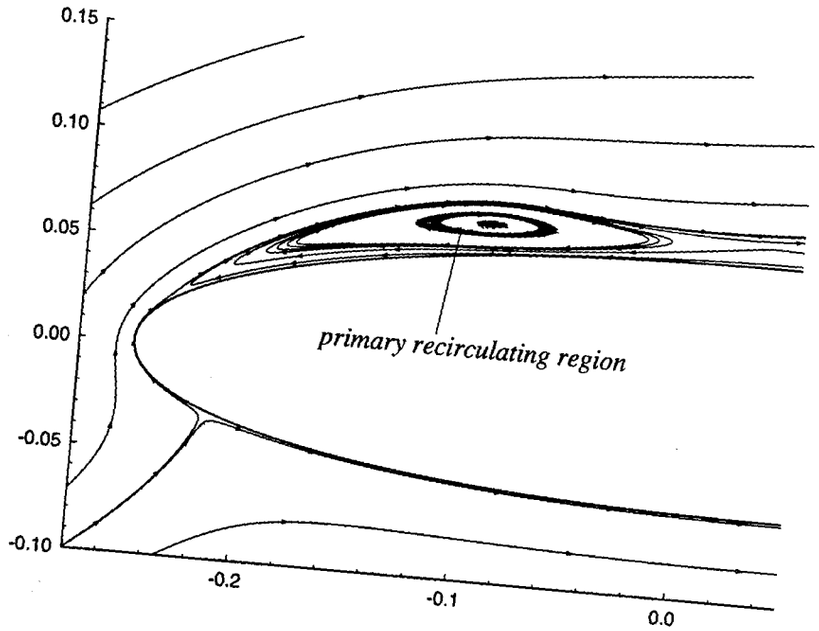

Figure 27: Instantaneous streamlines at $\alpha = 19.5°$ ($Re_c = 10^4$, $M_\infty = 0.2$, $\Omega_o^+ = 0.2$; Case 1)

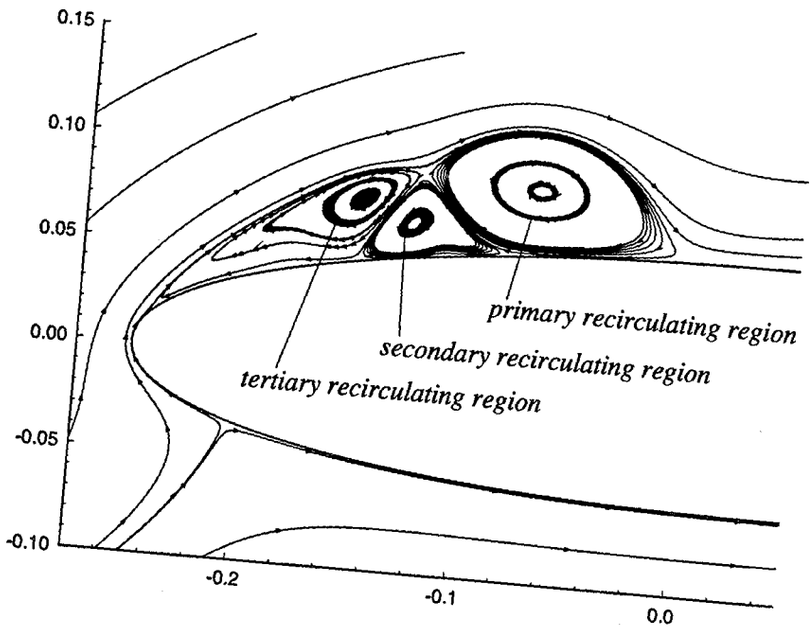

Figure 28: Instantaneous streamlines at $\alpha = 22.5°$ ($Re_c = 10^4$, $M_\infty = 0.2$, $\Omega_o^+ = 0.2$; Case 1)

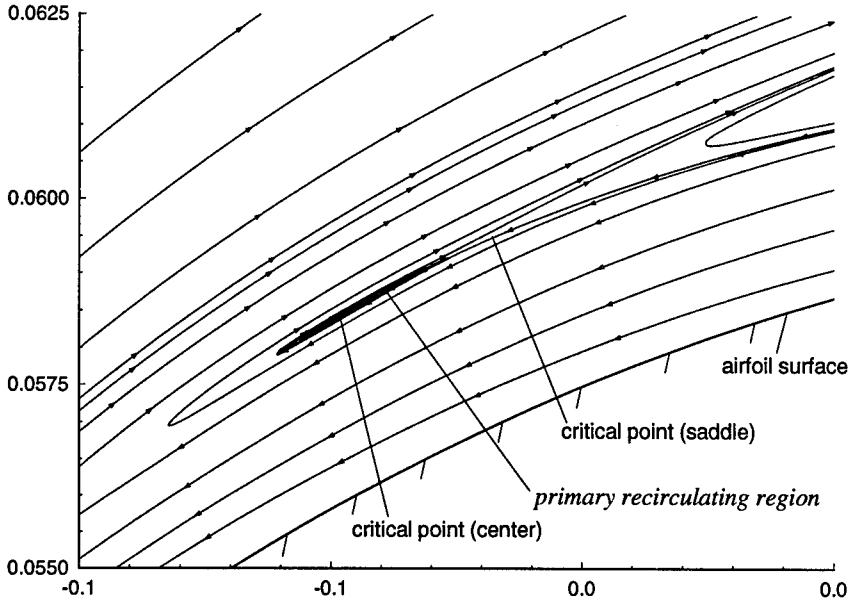

Figure 29: Instantaneous streamlines at $\alpha = 15°$ ($Re_c = 10^4$, $M_\infty = 0.2$, $\Omega_o^+ = 0.2$; Case 1)

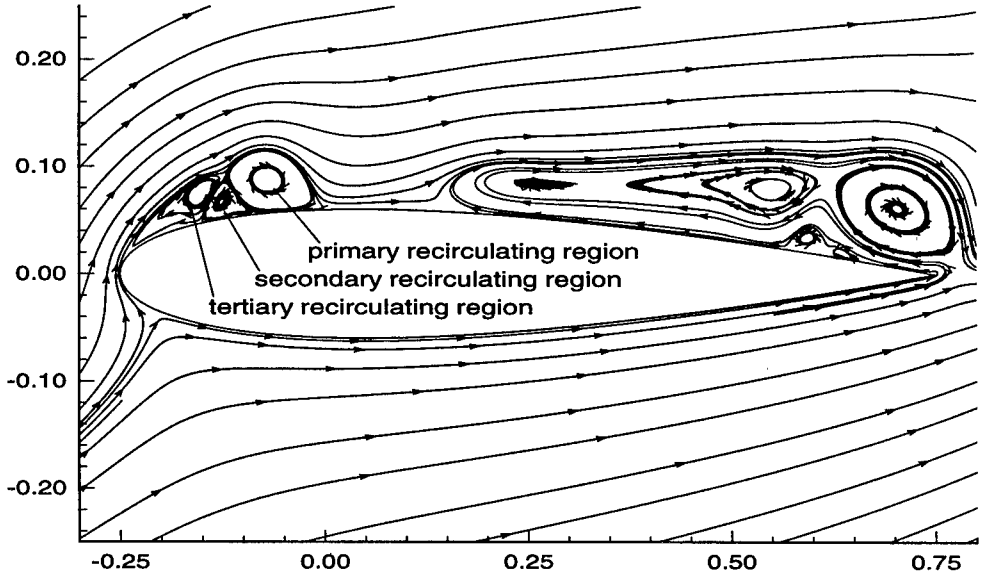

Figure 30: Instantaneous streamlines over the entire airfoil at $\alpha = 22.5°$ ($Re_c = 10^4$, $M_\infty = 0.2$, $\Omega_o^+ = 0.2$; Case 1)

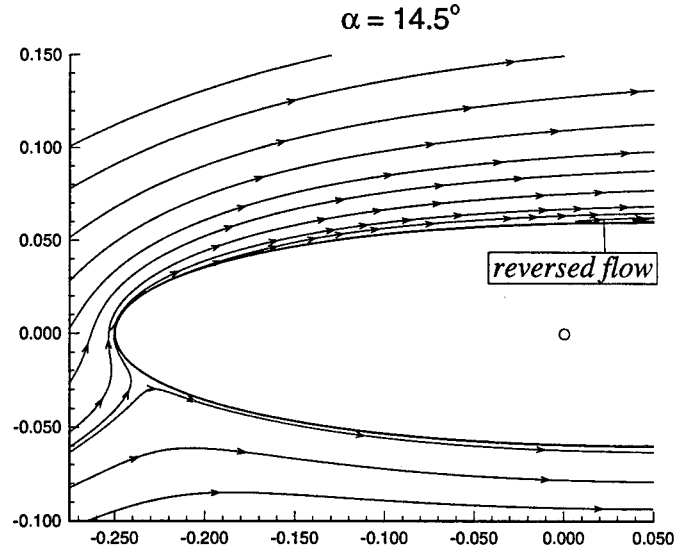

Figure 31: Instantaneous streamlines at $\alpha = 14.5°$ employing unstructured grid ($Re_c = 10^4$, $M_\infty = 0.2$, $\Omega_o^+ = 0.2$; Case 1)

9.2 Case 1 : $Re_c = 10^4$, $M_\infty = 0.2$, $\Omega_o^+ = 0.2$ (Unstructured Grid)

Instantaneous streamlines obtained using the unstructured grid code are shown in Figs. 31 to 35 at $\alpha = 14.5°$, 16.5°, 19.5°, 21.0° and 22.5°. Overall, there is close agreement between the structured and unstructured grid computations. The primary recirculating region is evident in both cases at $\alpha = 16.5°$, and has grown at $\alpha = 19.5°$. The secondary and tertiary recirculating regions at $\alpha = 22.5°$ are quantitatively very similar in both computations. The close comparison between the separate computations using two fundamentally different algorithms establishes the credibility of the results.

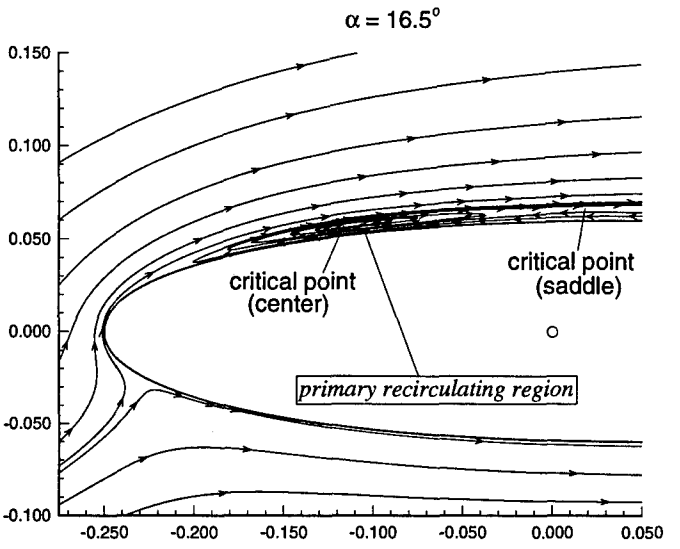

Figure 32: Instantaneous streamlines at $\alpha = 16.5°$ employing unstructured grid ($Re_c = 10^4$, $M_\infty = 0.2$, $\Omega_o^+ = 0.2$; Case 1)

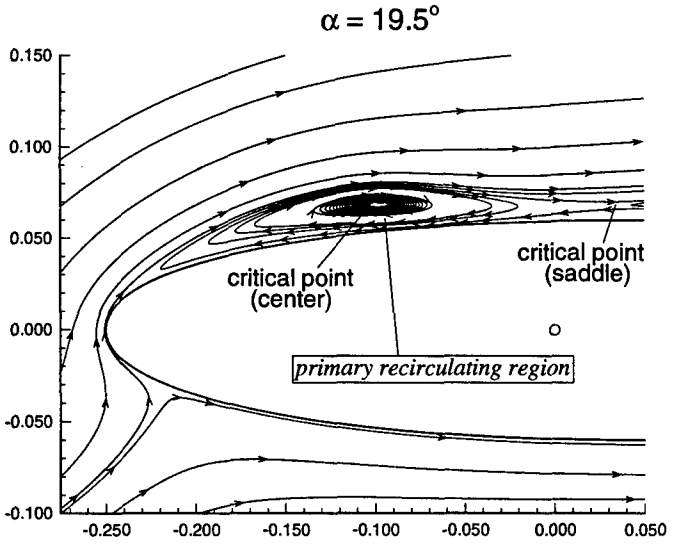

Figure 33: Instantaneous streamlines at $\alpha = 19.5°$ employing unstructured grid ($Re_c = 10^4$, $M_\infty = 0.2$, $\Omega_o^+ = 0.2$; Case 1)

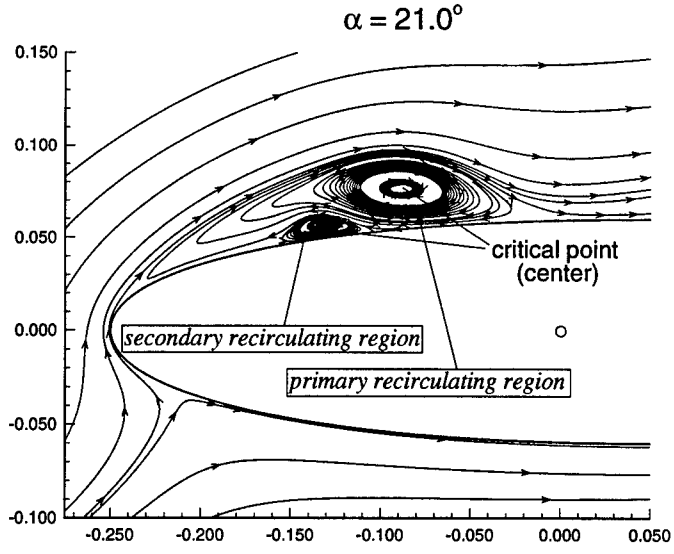

Figure 34: Instantaneous streamlines at $\alpha = 21.0°$ employing unstructured grid ($Re_c = 10^4$, $M_\infty = 0.2$, $\Omega_o^+ = 0.2$; Case 1)

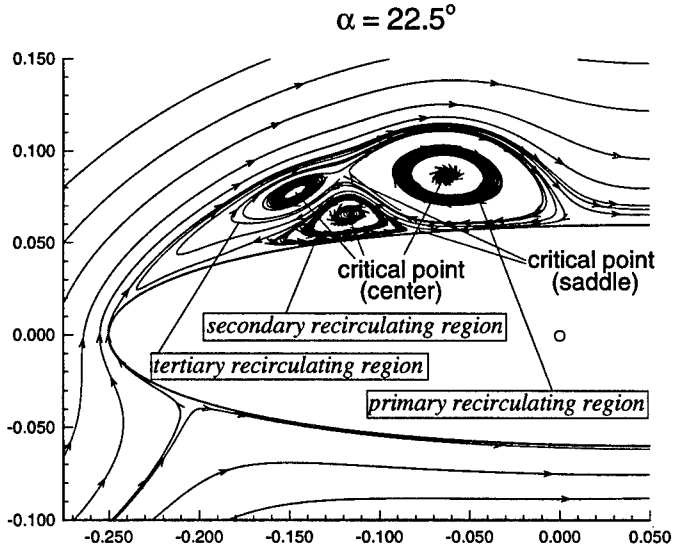

Figure 35: Instantaneous streamlines at $\alpha = 22.5°$ employing unstructured grid ($Re_c = 10^4$, $M_\infty = 0.2$, $\Omega_o^+ = 0.2$; Case 1)

9.3 Case 2 : $Re_c = 10^4$, $M_\infty = 0.2$, $\Omega_o^+ = 0.1$

The instantaneous streamlines are shown in figures 36 through 39 for $\alpha = 13.5°$, $15°$, $17°$ and $18°$, respectively. At $\alpha = 13.5°$, there is reversed flow on the upper surface extending almost to the leading edge. However, there are no recirculating regions in the area shown. (Flow near the trailing edge shows complex separation behavior.) The clockwise rotating primary recirculating region forms at $\alpha = 14.29°$ at 27% chord and a distance $1.25 \times 10^{-2}c$ above the wall. At $\alpha = 15°$, the primary recirculating region is shown. At $\alpha = 17°$, a counterclockwise rotating secondary recirculating region forms below the primary recirculating region at the 16% chord position. The primary recirculating region has grown normal to the airfoil surface and also moved toward the leading edge. The instantaneous streamlines are shown over the entire airfoil at $\alpha = 18°$ in figure 39, which shows that the developments in the leading edge region is relatively isolated from developments in the trailing edge region. A clockwise rotating tertiary recirculating region develops on top of the secondary recirculating region in between the leading edge and the primary recirculating region. The flow structures are similar to Case 1 ($\Omega_o^+ = 0.2$). However, the primary recirculating region appears at a smaller angle as compared to Case 1. Also, the structures form farther away from the leading edge and toward the trailing edge on the upper surface in Case 2.

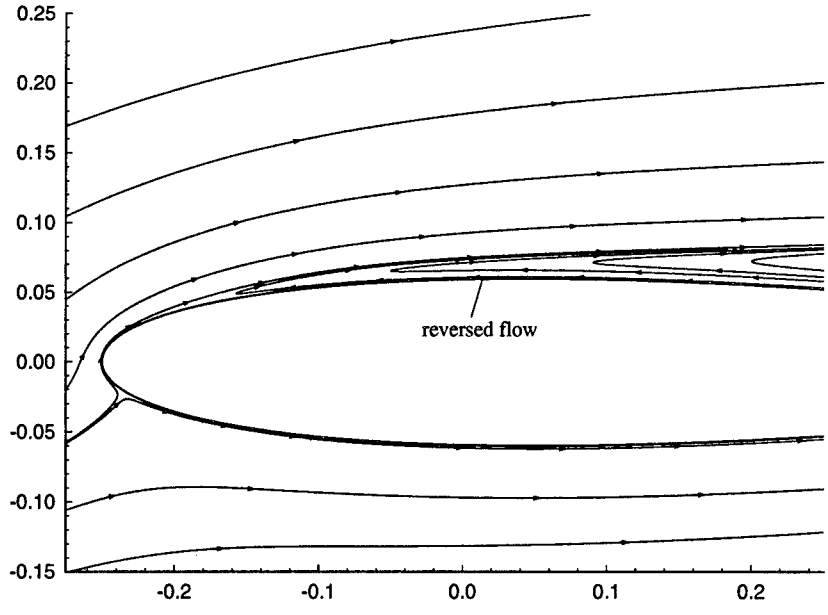

Figure 36: Instantaneous streamlines at $\alpha = 13.5°$ ($Re_c = 10^4$, $M_\infty = 0.2$, $\Omega_o^+ = 0.1$; Case 2)

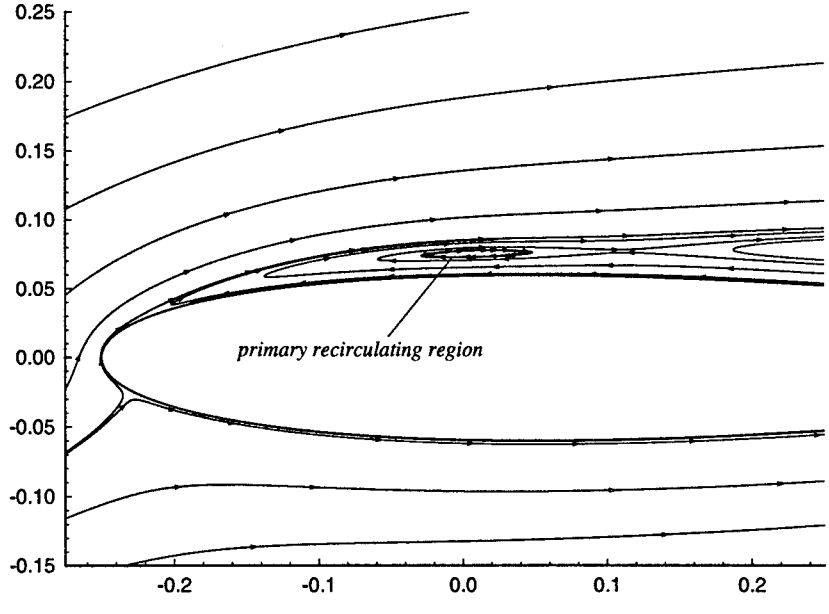

Figure 37: Instantaneous streamlines at $\alpha = 15°$ ($Re_c = 10^4$, $M_\infty = 0.2$, $\Omega_o^+ = 0.1$; Case 2)

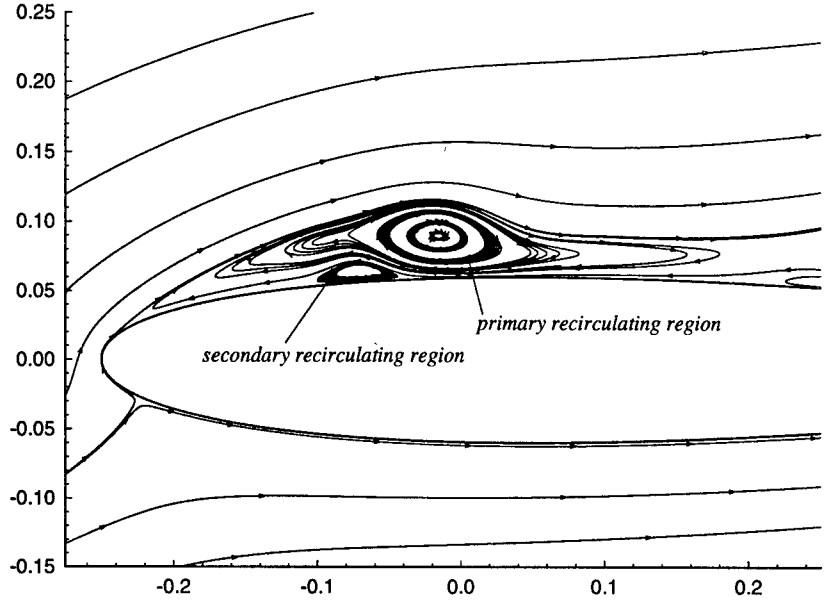

Figure 38: Instantaneous streamlines at $\alpha = 17°$ ($Re_c = 10^4$, $M_\infty = 0.2$, $\Omega_o^+ = 0.1$; Case 2)

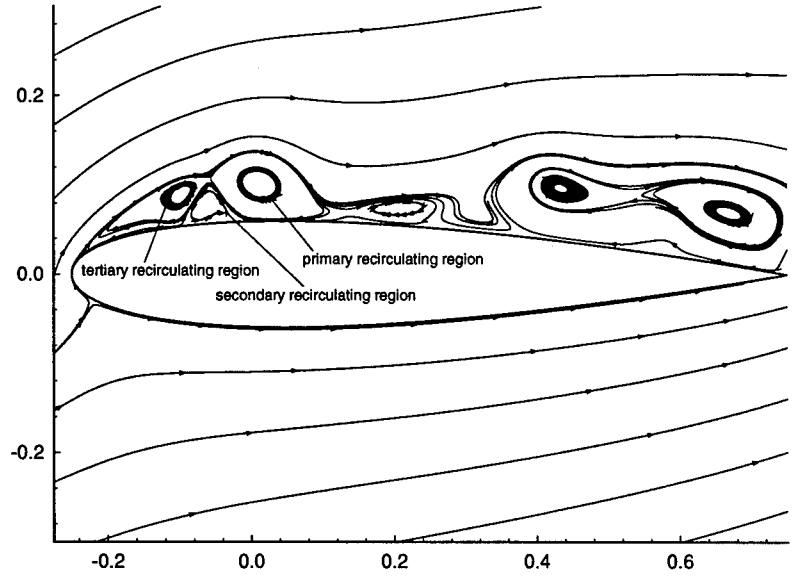

Figure 39: Instantaneous streamlines over the entire airfoil at $\alpha = 18°$ ($Re_c = 10^4$, $M_\infty = 0.2$, $\Omega_o^+ = 0.1$; Case 2)

9.4 Case 3 : $Re_c = 10^4$, $M_\infty = 0.2$, $\Omega_o^+ = 0.05$

The instantaneous streamlines over the entire airfoil are shown in figures 40 through 43 for $\alpha = 9°$, $10.5°$, $12°$, and $13.5°$, respectively. At $\alpha = 9°$, the reversed flow extends over most of the airfoil upper surface and a trailing edge recirculating region can be seen. The reversed flow extends over the entire airfoil upper surface at $\alpha = 10.5°$. The trailing edge recirculating region stretches along the airfoil upper surface and breaks down into multiple recirculating regions at $\alpha = 12°$ extending over the entire airfoil top surface. Unlike the Cases 1 and 2 (which are at higher pitch rate), the flow developments near the trailing edge are not isolated from the developments near the leading edge. Also, the recirculating regions appear far from the wall (average distance of $4.0 \times 10^{-2}c$). The instantaneous streamlines at $\alpha = 13.5°$ demonstrate the increase in size of the multiple recirculating regions in the transverse direction with increase in the angle of attack, giving rise to breakdown of the entire upper surface boundary layer. The development of the flow structure which gives rise to the dynamic stall vortex is not isolated in the leading edge only and appears over the entire airfoil upper surface, which is different from Cases 1 and 2.

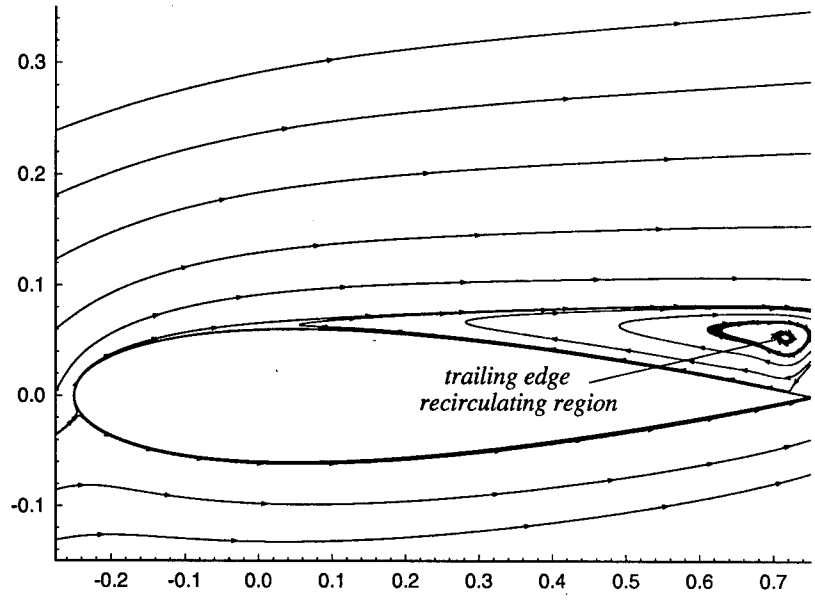

Figure 40: Instantaneous streamlines at $\alpha = 9.0°$ ($Re_c = 10^4$, $M_\infty = 0.2$, $\Omega_o^+ = 0.05$; Case 3)

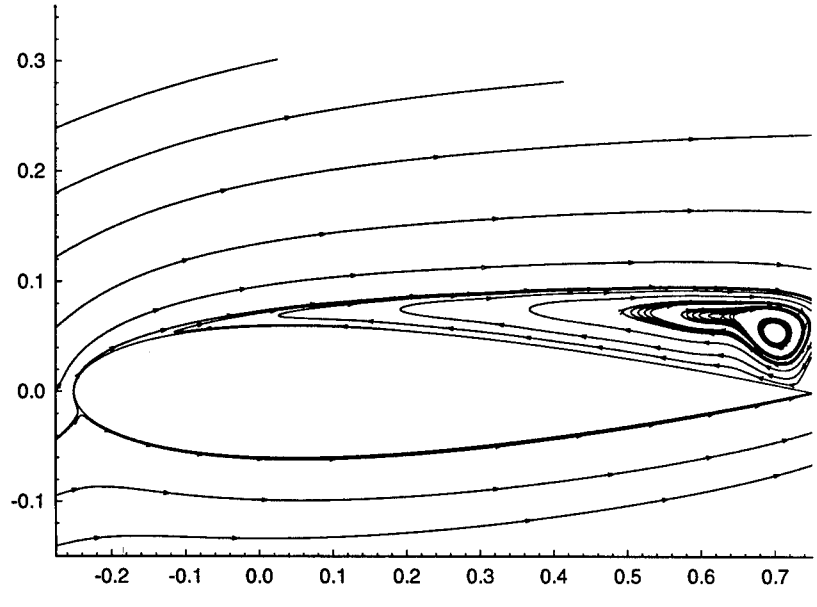

Figure 41: Instantaneous streamlines at $\alpha = 10.5°$ ($Re_c = 10^4$, $M_\infty = 0.2$, $\Omega_o^+ = 0.05$; Case 3)

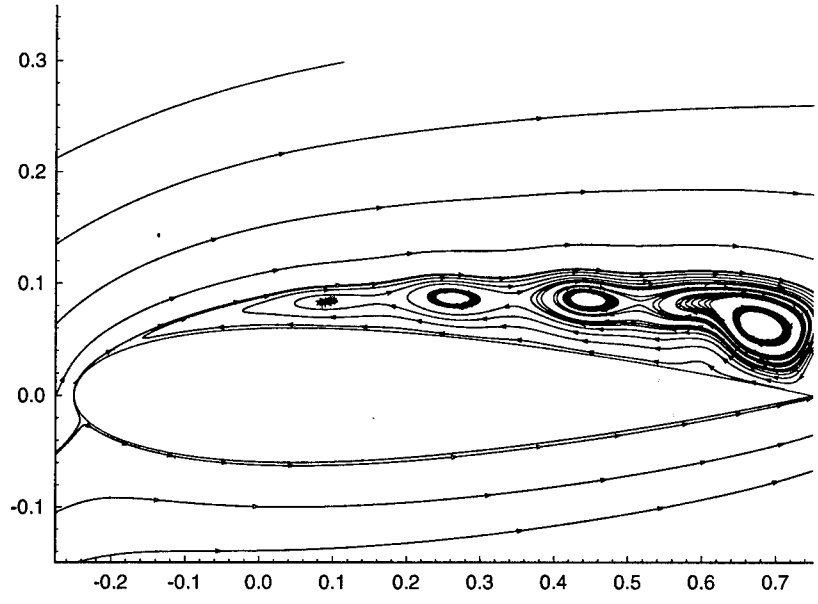

Figure 42: Instantaneous streamlines at $\alpha = 12°$ ($Re_c = 10^4$, $M_\infty = 0.2$, $\Omega_o^+ = 0.05$; Case 3)

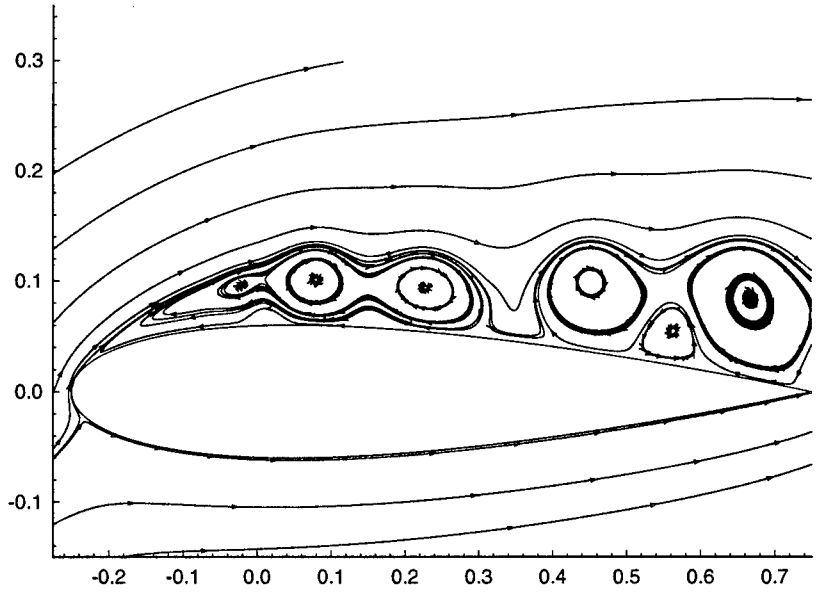

Figure 43: Instantaneous streamlines at $\alpha = 13.5°$ ($Re_c = 10^4$, $M_\infty = 0.2$, $\Omega_o^+ = 0.05$; Case 3)

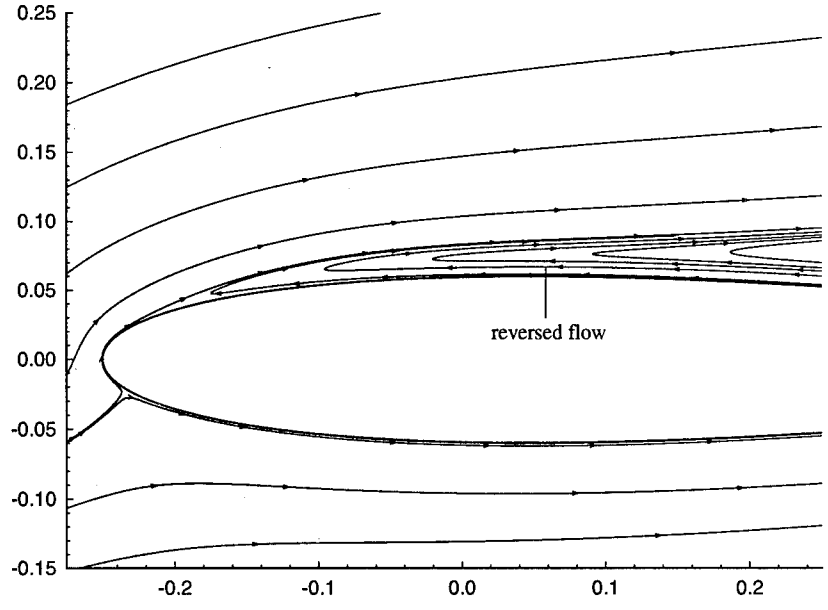

Figure 44: Instantaneous streamlines at $\alpha = 18°$ ($Re_c = 10^4$, $M_\infty = 0.5$, $\Omega_o^+ = 0.2$; Case 4)

9.5 Case 4 : $Re_c = 10^4$, $M_\infty = 0.5$, $\Omega_o^+ = 0.2$

The instantaneous streamlines over the front 50% of the airfoil are shown in figures 44 through 47 for $\alpha = 18°$, 19.5°, 22.5°, and 25.5°, respectively. The reversed flow region observed over the airfoil upper surface at $\alpha = 18°$ is much thicker as compared to the reversed flow region at $M_\infty = 0.2$ (Cases 1 and 2). At $\alpha = 19.5°$, the primary recirculating region has formed. In particular, the primary recirculating region appears first at $\alpha = 18.8°$ at 30% chord position and a distance $1.7 \times 10^{-2} c$ from the airfoil surface. The secondary recirculating region can be seen at $\alpha = 22.5°$. The secondary recirculating region develops below the primary recirculating region which expands normal to airfoil surface. At $\alpha = 25.5°$, the tertiary recirculating region appears above the secondary recirculating region and the primary recirculating region is pushed farther from the airfoil surface. In this case, the vortical structures have larger length scale as compared to Case 1 or Case 2. Again, the development of the flow field is very similar to Cases 1 and 2, but with a delay.

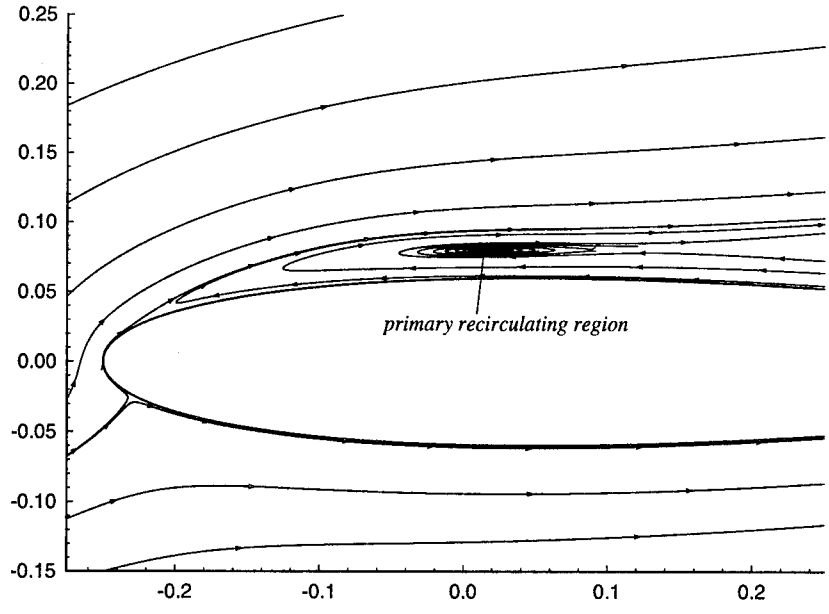

Figure 45: Instantaneous streamlines at $\alpha = 19.5°$ ($Re_c = 10^4$, $M_\infty = 0.5$, $\Omega_o^+ = 0.2$; Case 4)

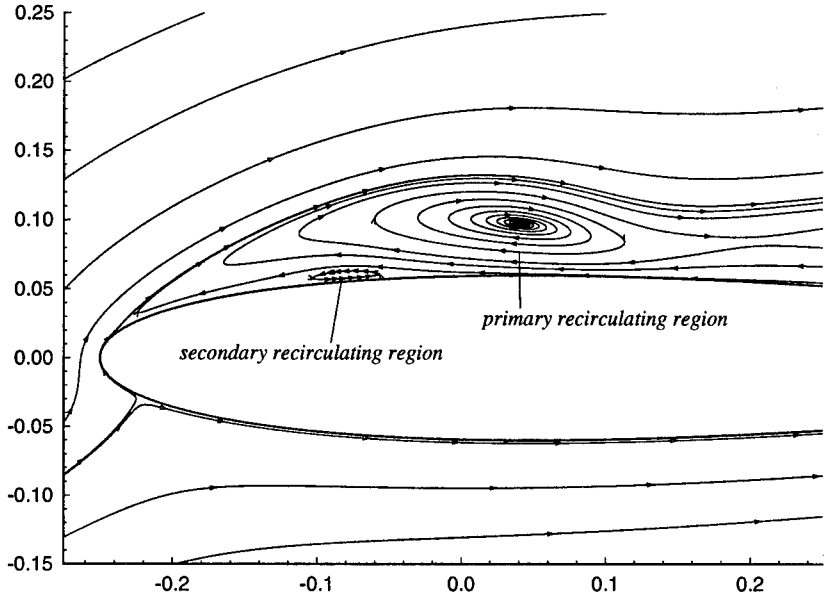

Figure 46: Instantaneous streamlines at $\alpha = 22.5°$ ($Re_c = 10^4$, $M_\infty = 0.5$, $\Omega_o^+ = 0.2$; Case 4)

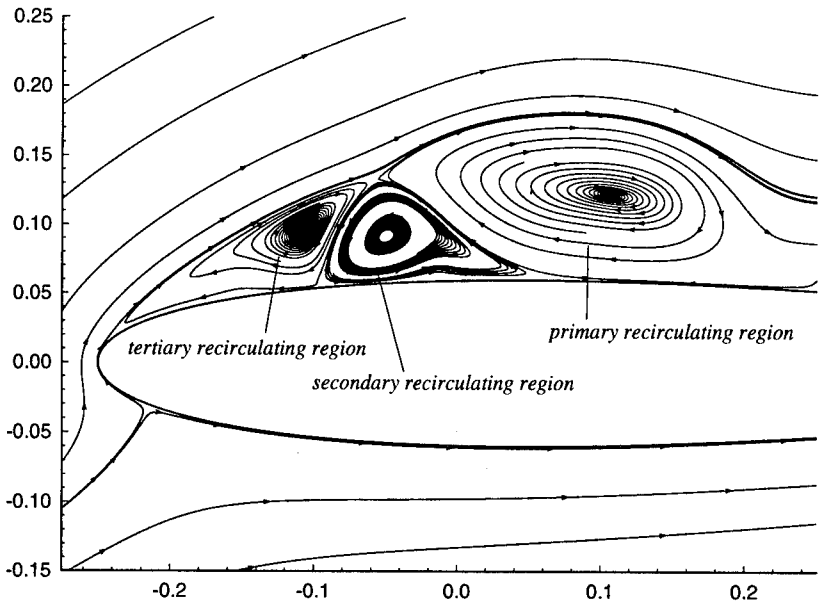

Figure 47: Instantaneous streamlines at $\alpha = 25.5°$ ($Re_c = 10^4$, $M_\infty = 0.5$, $\Omega_o^+ = 0.2$; Case 4)

9.6 Case 5 : $Re_c = 10^4$, $M_\infty = 0.5$, $\Omega_o^+ = 0.1$

The instantaneous streamlines at $\alpha = 15°$, 16.5°, 18°, and 19.5° over the leading 70% of the airfoil are shown in figures 48 through 51. At $\alpha = 15°$, a thick reversed flow region is observed over the entire upper surface. The primary recirculating originates at $\alpha = 15.65°$ at 44% chord position and a distance $3.8 \times 10^{-2}c$ above the airfoil surface. The primary recirculating region is observed to have developed at $\alpha = 16.5°$, and the secondary recirculating region forms below the primary recirculating region ($\alpha = 18°$). At $\alpha = 19.5°$, the tertiary recirculating region can be seen. The secondary recirculating region separates the primary recirculating region from the tertiary recirculating region. The separation process is again observed to be similar to Cases 1, 2, and 4. The principal differences are that the structures form farther away from the leading edge compared to the other three cases, and the length scale associated with the flow structures is substantially greater.

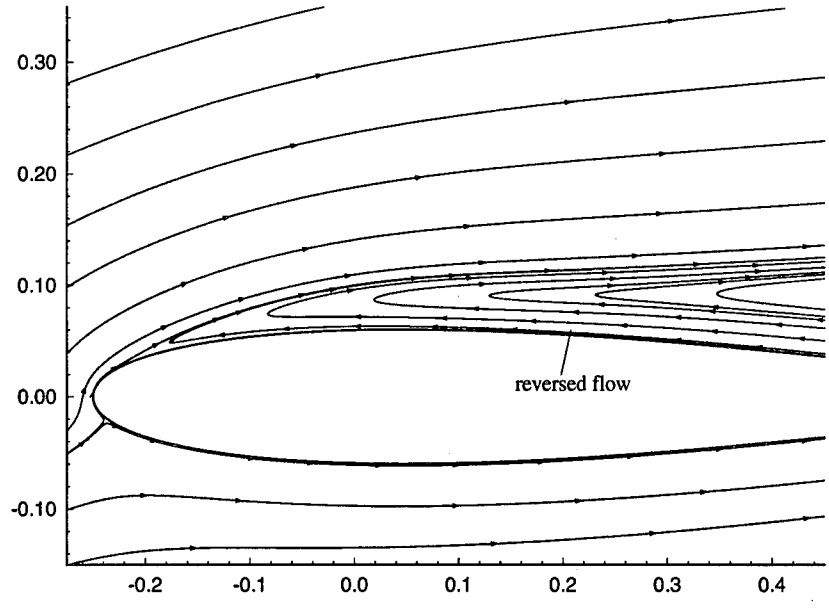

Figure 48: Instantaneous streamlines at $\alpha = 15°$ ($Re_c = 10^4$, $M_\infty = 0.5$, $\Omega_o^+ = 0.1$; Case 5)

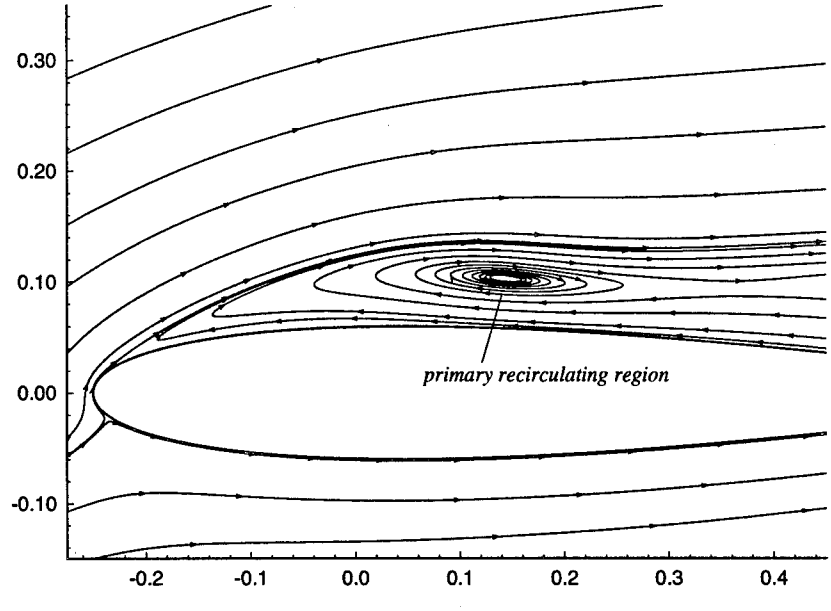

Figure 49: Instantaneous streamlines at $\alpha = 16.5°$ ($Re_c = 10^4$, $M_\infty = 0.5$, $\Omega_o^+ = 0.1$; Case 5)

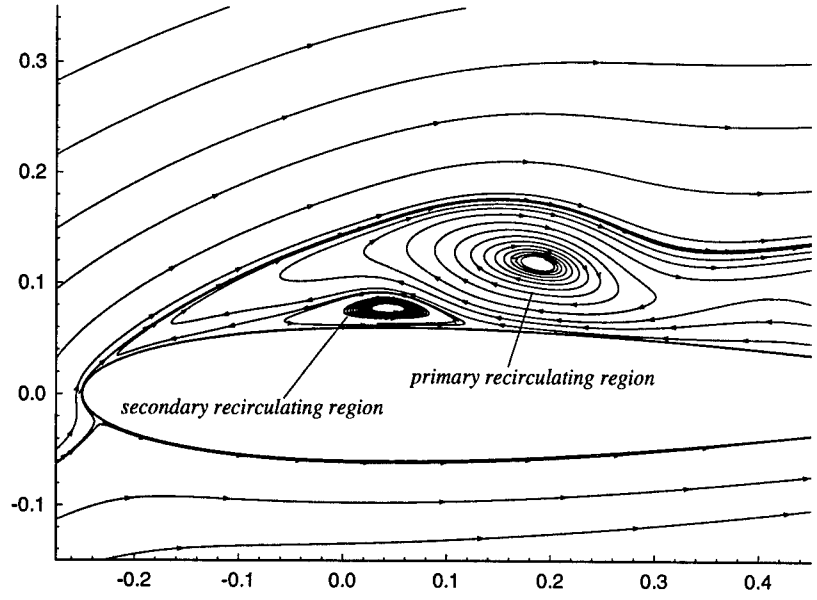

Figure 50: Instantaneous streamlines at $\alpha = 18°$ ($Re_c = 10^4$, $M_\infty = 0.5$, $\Omega_o^+ = 0.1$; Case 5)

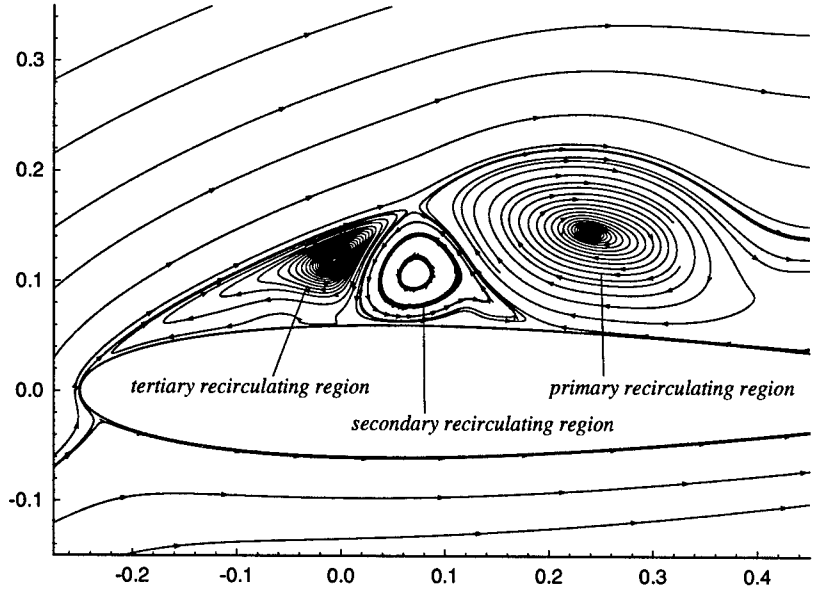

Figure 51: Instantaneous streamlines at $\alpha = 19.5°$ ($Re_c = 10^4$, $M_\infty = 0.5$, $\Omega_o^+ = 0.1$; Case 5)

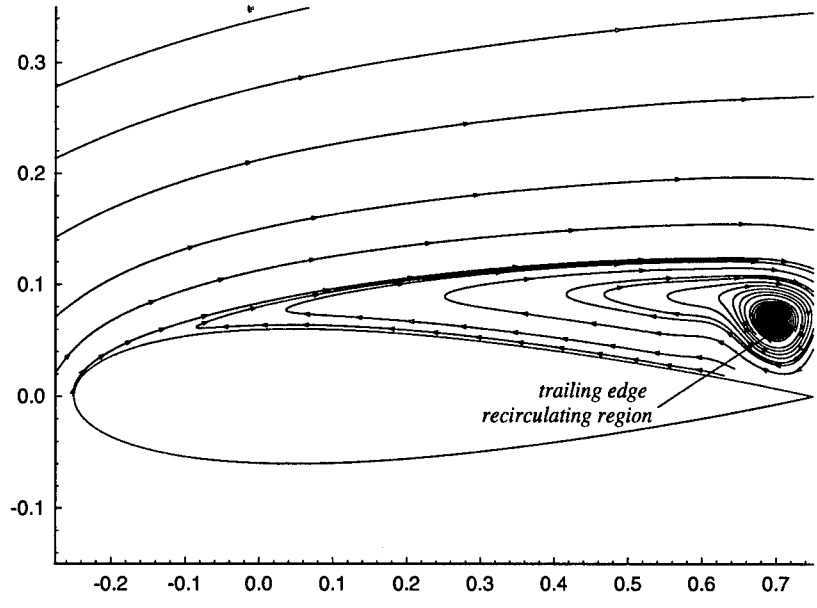

Figure 52: Instantaneous streamlines at $\alpha = 10.5°$ ($Re_c = 10^4$, $M_\infty = 0.5$, $\Omega_o^+ = 0.05$; Case 6)

9.7 Case 6 : $Re_c = 10^4$, $M_\infty = 0.5$, $\Omega_o^+ = 0.05$

The instantaneous streamlines over the entire airfoil upper surface are shown in figures 52 through 55 for $\alpha = 10.5°$, $12°$, $13.5°$, and $15°$, respectively. At $\alpha = 10.5°$, a recirculating region is present near the trailing edge and the reversed flow extends over the entire airfoil upper surface. The trailing edge recirculating region divides into two separate recirculating regions at $\alpha = 12°$. The recirculating region attached at the trailing edge is shed in the wake at $\alpha = 13.5°$, while the other one expands and is still attached to the airfoil surface. With increase in α two more recirculating regions appear and are observed at $\alpha = 15°$. The development of the flow structures in this case resembles Cases 1, 2, 4, and 5. However, the flow structures are not constrained to only a part of the airfoil upper surface. The primary recirculating region appears near the trailing edge and extends over the entire airfoil surface before breaking down into secondary and tertiary recirculating regions.

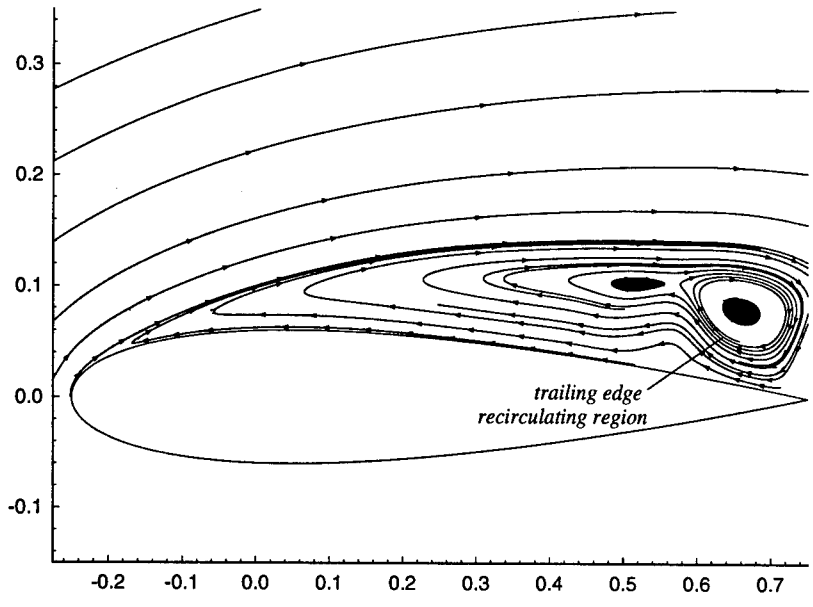

Figure 53: Instantaneous streamlines at $\alpha = 12°$ ($Re_c = 10^4$, $M_\infty = 0.5$, $\Omega_o^+ = 0.05$; Case 6)

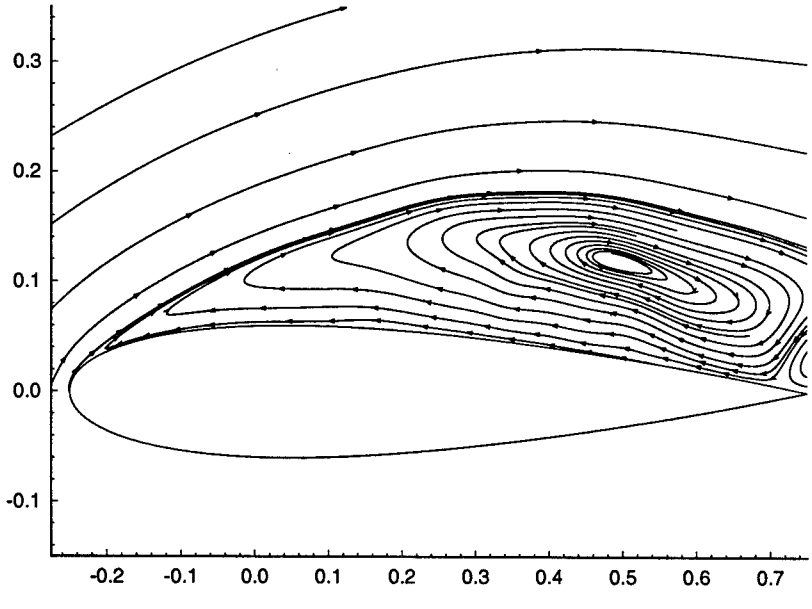

Figure 54: Instantaneous streamlines at $\alpha = 13.5°$ ($Re_c = 10^4$, $M_\infty = 0.5$, $\Omega_o^+ = 0.05$; Case 6)

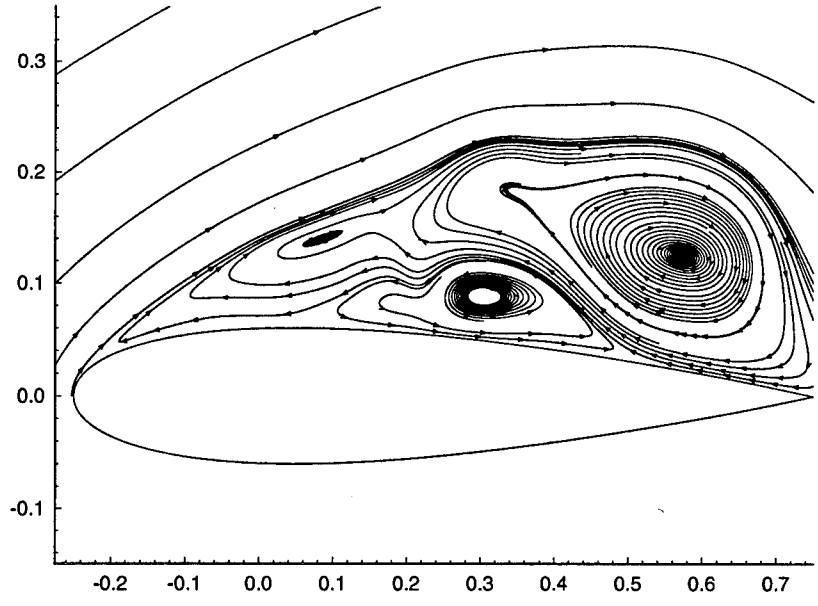

Figure 55: Instantaneous streamlines at $\alpha = 15°$ ($Re_c = 10^4$, $M_\infty = 0.5$, $\Omega_o^+ = 0.05$; Case 6)

9.8 Case 7 : $Re_c = 10^5$, $M_\infty = 0.5$, $\Omega_o^+ = 0.2$

The instantaneous streamlines are presented for $\alpha = 15°$, 18°, 19°, and 19.5° in figures 56 through 59. The instantaneous streamlines at $\alpha = 15°$ (figure 56) show the presence of the primary recirculating region near the leading edge in the close-up figure of the boxed region. In particular, the primary recirculating region forms at $\alpha = 14.9°$ as compared to $\alpha = 18.8°$ for Case 4. The primary recirculating region expands in a direction normal to airfoil surface with increase in α. This can be observed at $\alpha = 18°$. At $\alpha = 19°$, the secondary and tertiary recirculating regions are also evident. Up to $\alpha = 19°$, the development of the flow field is very similar to Cases 1, 2, 4, 5 and 6. However, at $\alpha = 19.5°$, multiple recirculating regions are seen attached to the airfoil surface. Similar results have been reported in an analytical study by Smith [38] and in a numerical study by Ghia *et al* [15] at $Re_c = 4.5 \times 10^4$, where simultaneous appearances of multiple recirculating regions near the leading edge at high Reynolds numbers were found. The pressure coefficient contours at $\alpha = 18°$, and 19.5° in figures 60 and 61, respectively, show the appearance of a shock in the flowfield at $\alpha = 19.5°$. Examination

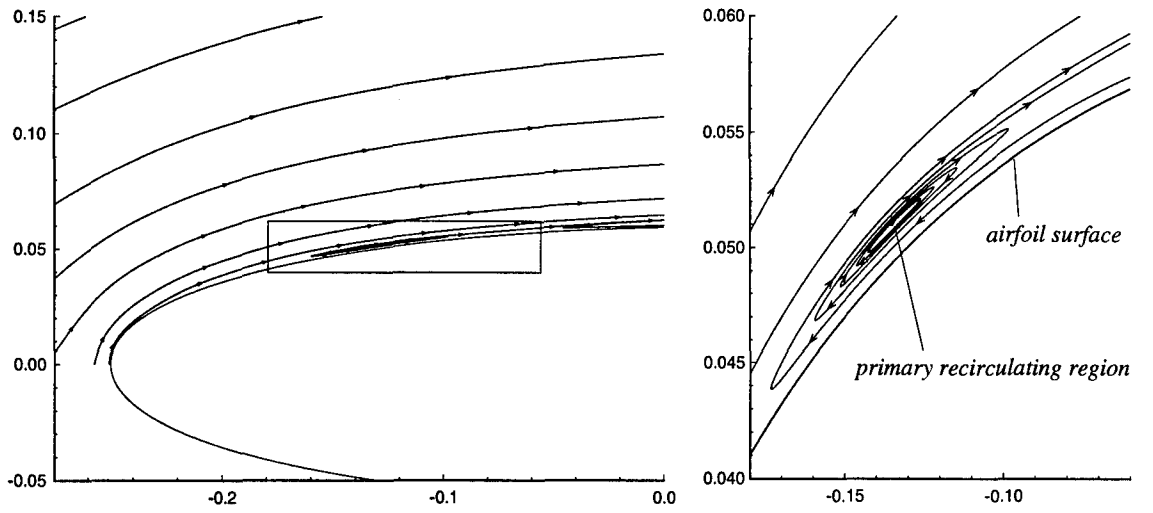

Figure 56: Instantaneous streamlines at $\alpha = 15°$ ($Re_c = 10^5$, $M_\infty = 0.5$, $\Omega_o^+ = 0.2$; Case 7)

of the Mach contours and the divergence of velocity in the flowfield (not shown here) also indicates a shock. The shock appears between $\alpha = 19°$ and $\alpha = 19.5°$. A separate inviscid computation showed similar appearance of a shock near the leading edge, which proves that the appearing shock is an inviscid phenomenon. For the inviscid case, the shock appears at a smaller angle of attack and nearer to the leading edge than in the viscous case. The length scale associated with the recirculating regions in this case is observed to be very small as compared to those in the other cases.

9.9 Effect of compressibility

The results indicate important trends related to the increase in Mach number. In the Cases 1 & 4 and 2 & 5, the pitch rate and Reynolds number are fixed while the Mach number is increased from 0.2 to 0.5. Increasing the Mach number (at fixed Reynolds number and pitch rate) causes the primary recirculating region to form farther from the airfoil surface and delays its formation. Sankar and Tassa [35] also saw a delay in the formation of the "leading edge vortex" (primary recirculating region) when the Mach number was increased from 0.2 to 0.4 at $Re_c = 5.0 \times 10^3$. Figure 62 displays

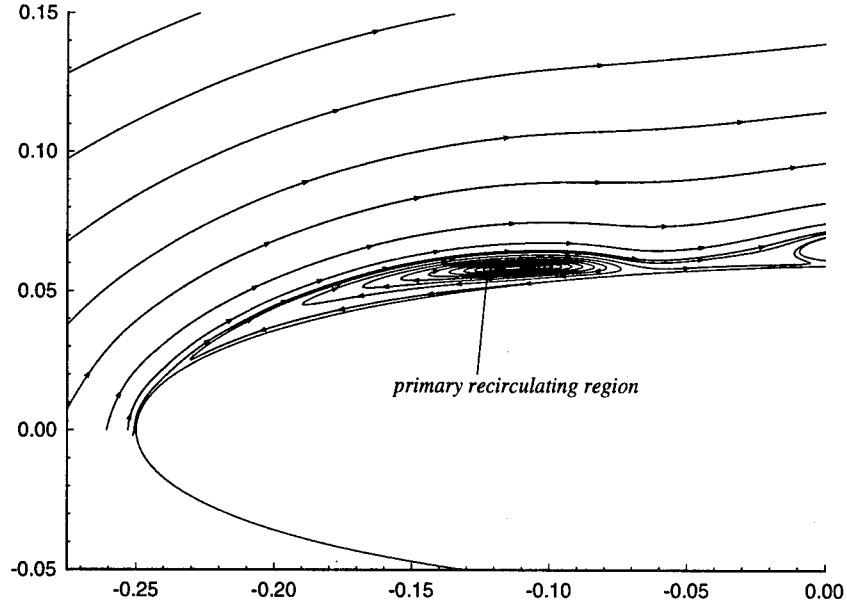

Figure 57: Instantaneous streamlines at $\alpha = 18°$ ($Re_c = 10^5$, $M_\infty = 0.5$, $\Omega_o^+ = 0.2$; Case 7)

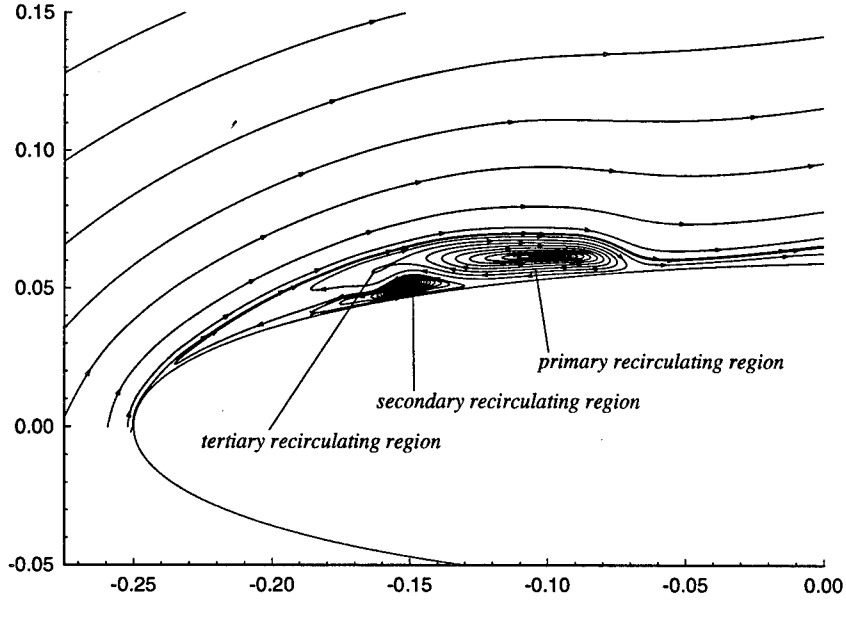

Figure 58: Instantaneous streamlines at $\alpha = 19°$ ($Re_c = 10^5$, $M_\infty = 0.5$, $\Omega_o^+ = 0.2$; Case 7)

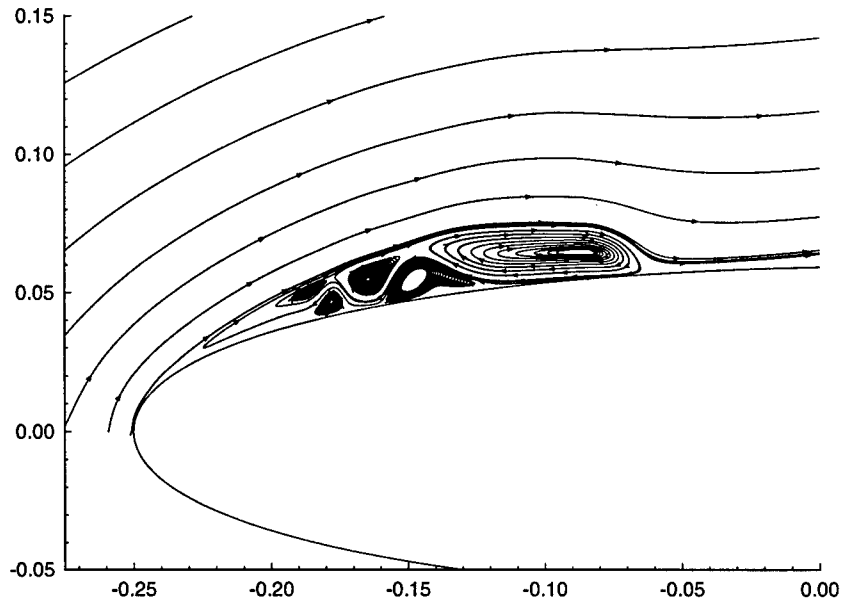

Figure 59: Instantaneous streamlines at $\alpha = 19.5°$ ($Re_c = 10^5$, $M_\infty = 0.5$, $\Omega_o^+ = 0.2$; Case 7)

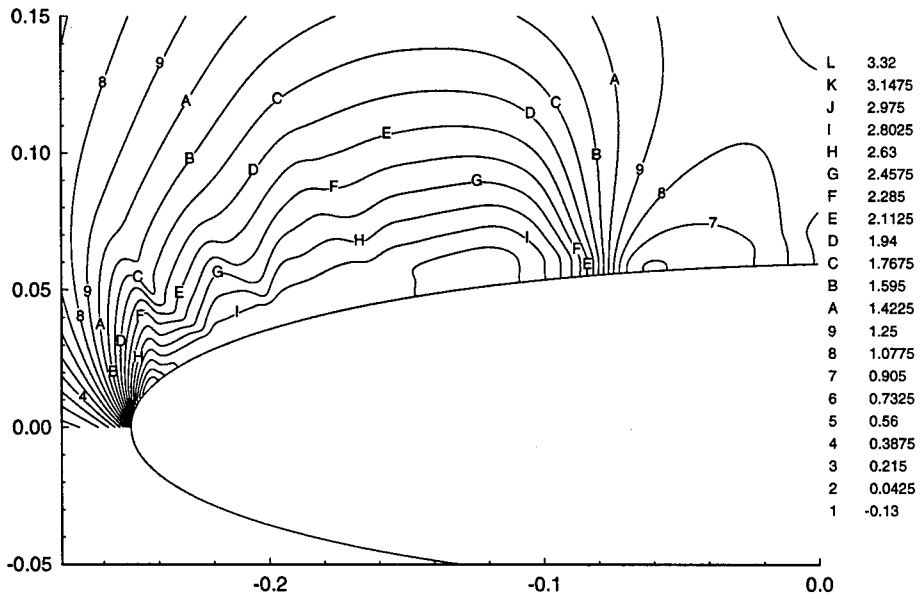

Figure 60: Pressure coefficient contours at $\alpha = 18°$ ($Re_c = 10^5$, $M_\infty = 0.5$, $\Omega_o^+ = 0.2$; Case 7)

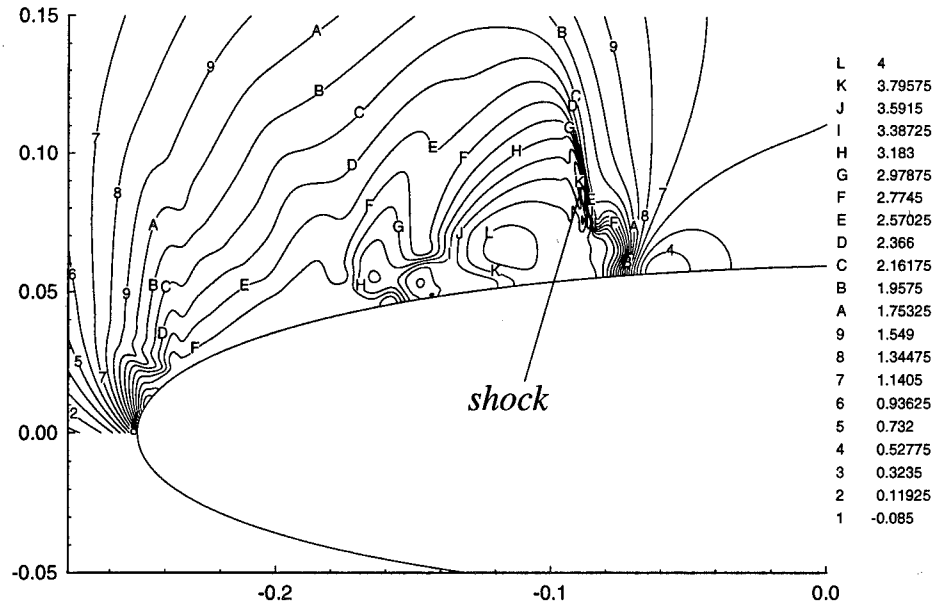

Figure 61: Pressure coefficient contours at α=19.5° ($Re_c = 10^5$, $M_\infty = 0.5$, $\Omega_o^+ = 0.2$; Case 7)

the angle at which the primary recirculating region first appears as a function of the pitch rate for two different Mach numbers at $Re_c = 10^4$. At a constant pitch rate, the formation of the primary recirculating region is delayed to higher angles when the Mach number is increased from 0.2 to 0.5. The surface pressure coefficient was compared to study the effect of Mach number. Figure 63 shows that for a fixed pitch rate and Reynolds number, increasing the Mach number causes a decrease in the leading edge suction pressure coefficient which in turn results in a lower adverse pressure gradient on the airfoil upper surface. The decreased adverse pressure gradient on the top surface at higher Mach numbers retards the movement of the reversed flow region toward the leading edge but increases the thickness of the reversed flow region and eventually delays the formation of the primary recirculating region. The length scale associated with the flow structures increase as well. The decrease in the magnitude of the leading edge suction pressure coefficient is primarily due to the compressibility effects on the boundary layer, which increase the effective radius of the leading edge of the airfoil and in turn lead to a decrease in the leading edge suction pressure coefficient. This is opposite to the behavior expected from a quasi-stationary application of the Prandtl-Glauert rule,

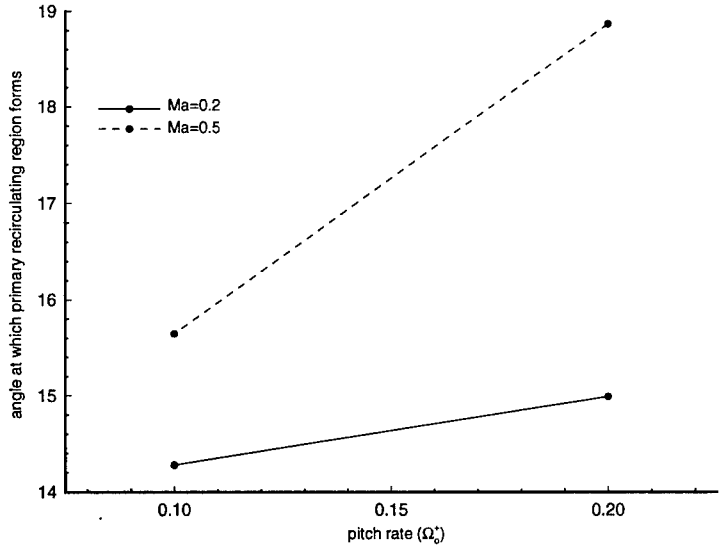

Figure 62: Effect of Mach number and pitch rate on the appearance of the primary recirculating region at $Re_c = 10^4$

where $C_{p_M}/C_{p_i} = 1/\sqrt{1-M^2}$ (C_{p_M} is the pressure coefficient for a compressible case of Mach number M and C_{p_i} is the pressure coefficient for an incompressible case).

9.10 Effect of pitch-rate

The flowfield is strongly dependent on the pitch rate. Comparison of Cases 1, 2 and 3, or 4, 5 and 6 exhibit the effects of the pitch rate at a fixed Mach number and Reynolds number. The pitch rate is decreased from 0.2 through 0.05 in cases 1 through 3 and 4 through 6. Increase in the pitch rate of the airfoil delays the formation of the primary recirculating region to higher angles of attack. The primary recirculating region forms closer to the leading edge on the upper surface. It is also observed that decrease in the pitch rate causes the transition from a predominantly leading-edge separation to a complex separation over the entire airfoil. Figure 62 shows the delay in the formation of the recirculating region with increase in pitch rate at constant Mach numbers and $Re_c = 10^4$. It should be noted that the delay in the formation of the recirculating region to higher angles does not mean that there is an increase in the actual time from start of pitch-up to the appearance of the recirculating region (the pitch rate is different).

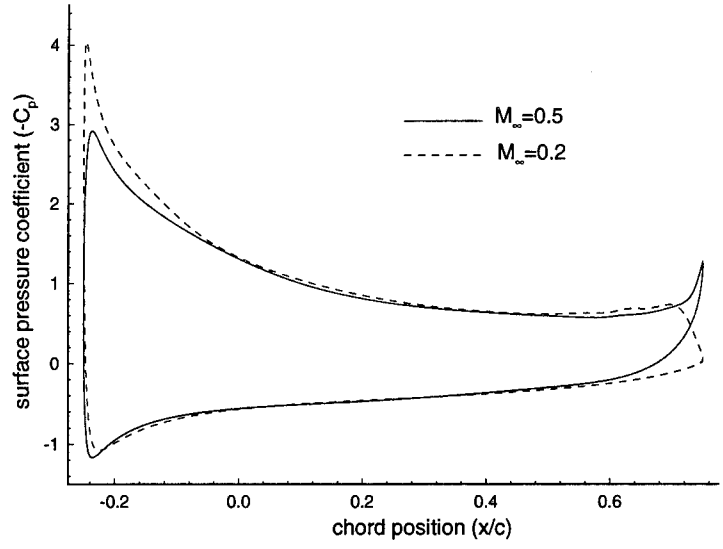

Figure 63: Comparison of the surface pressure coefficient at $\alpha = 16.5°$ for two different Mach numbers ($Re_c = 10^4$, $\Omega_o^+ = 0.2$)

At higher pitch rates, there is a decrease in the adverse pressure gradient on the upper surface of the airfoil (figure 64) that can also be explained from the potential flow theory, which slows down the development of the reversed flow region and defers the appearance of the primary recirculating region to a higher angle.

9.11 Effect of Reynolds number

The flowfield is sensitive to the change in Reynolds number. Cases 4 and 7 are compared to study the effect of increase in Reynolds number at a fixed Mach number and pitch rate. Increase in the Reynolds number hastens the appearance of the primary recirculating region and decreases the length scale of the flow structures. The primary recirculating region forms closer to the leading edge on the upper surface at higher Reynolds number. At $Re_c = 10^5$ and $M_\infty = 0.5$, a shock appears on the top surface. The appearance of the shock was found to be an inviscid phenomenon. Multiple recirculating regions develop simultaneously near the leading edge at higher Reynolds number and cause a complex separation of the boundary layer. Up to the formation of the shock, the evolution of the flowfield is identical in both cases except for the lag. The formation of the

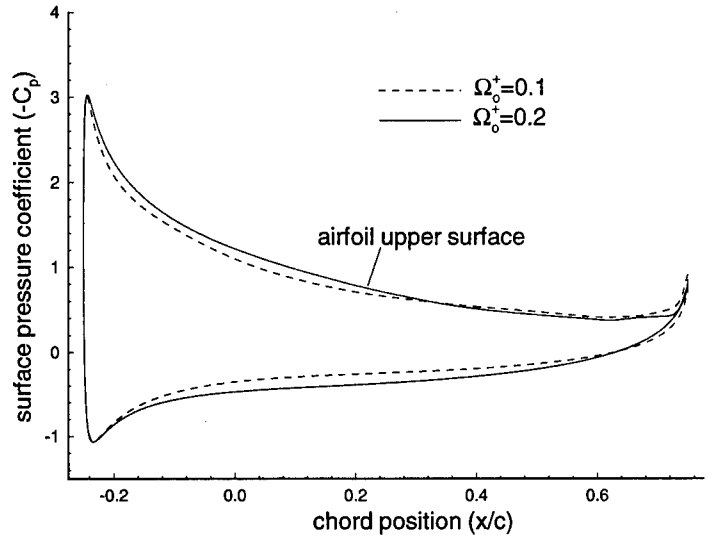

Figure 64: Comparison of the surface pressure coefficient at $\alpha = 13.5°$ for two different pitch rates ($Re_c = 10^4$, $M_\infty = 0.2$)

recirculating regions near the leading edge is not induced by the shock. Chandrasekhara *et al* [9] observed the presence of similar shocks near the leading edge at $M_\infty = 0.45$ and $Re_c = 3.6 \times 10^5$, in the experiments.

9.12 Linear Stability Analysis

A linear incompressible stability analysis was conducted to determine whether the formation of the primary recirculating region is related to an instability of the flow. The basic flow required for the stability analysis was obtained from the numerical simulations for Cases 1 and 2, which have been described in the preceding subsections. The Mach number in the flowfield does not exceed 0.6 in both the cases, and therefore an incompressible analysis was deemed sufficient.

In the stability analysis of a basic flow field, a small disturbance is introduced to the basic flow and the development of the flow field in time is sought to determine whether the flow field is stable or unstable. The velocities and the pressure are written as

$$u = U + u'; \quad v = V + v'; \quad p = P + p' \tag{103}$$

where U, V, and P denote the basic flow and u', v', and p' denote the disturbances in the

velocities and the pressure. These expressions are substituted into the incompressible Navier-Stokes equations which are then linearized. The disturbances are described as a complex perturbation streamfunction of the form

$$\psi'(x,y,t) = \varphi(y)\exp\{i(kx-\omega t)\} \tag{104}$$

where k and ω are the complex wavenumber and frequency respectively, $\varphi(y)$ is the complex amplitude function. The perturbed velocities are defined in terms of the perturbed streamfunction (ψ') and the pressure is eliminated from the linearized Navier-Stokes equation, which result in the following equation

$$\left[\frac{i}{kRe}(D^2-k^2)^2 + U(D^2-k^2) - \frac{\partial^2 U}{\partial y^2} - \frac{iV}{k}(D^2-k^2)D - \frac{\partial V}{\partial x}D \right.$$
$$\left. + ik\frac{\partial V}{\partial y} - \frac{i}{Re}\frac{\partial^2 U}{\partial y \partial x}D\right]\varphi - \frac{\omega}{k}(D^2-k^2)\varphi = 0 \tag{105}$$

where the operator 'D' denotes differentiation with respect to y. Details of the derivation of the above equation is given in Appendix E.

Equation (105) is a fourth order complex differential equation which together with the appropriate boundary condition defines the stability eigenvalue problem. In the present study, the reference frame is assumed to be attached to the airfoil surface and the x- and y-directions are aligned in the tangential and normal directions to the airfoil surface, respectively. The airfoil is pitching up at a constant pitch rate and therefore the boundary conditions can be written as

$$u' = v' = 0 \quad or \quad \varphi(y) = D\varphi(y) = 0 \quad at \quad y = 0 \tag{106}$$

$$\frac{d^2u'}{dy^2} = \frac{dv'}{dy} = 0 \quad or \quad D\varphi(y) = D^3\varphi(y) = 0 \quad at \quad y = \infty \tag{107}$$

The stability eigenvalue problem was solved by utilizing the Chevyshev polynomials to approximate the eigenfunctions [59]. To use the Chevyshev polynomial as a basis, the domain [0,∞] is mapped into the interval [-1,1] with the new variable z defined as $z = 1 - 2\exp(-y/y_0)$, where y_0 is the edge of the boundary layer. The eigenvalues of the system of equation are determined using the IMSL subroutines and the most unstable mode selected out of the set of eigenvalues, based on the imaginary part of the wave

frequency (ω) with the highest value. The flow is unstable when the imaginary part of the wave frequency is positive and its magnitude is a measure of the temporal growth rate of the disturbance.

The developed solver was validated by performing two computations to ascertain the accuracy. Stability computations were performed to determine the neutral curve ($\mathrm{Im}[\omega]=0$) for a Blasius profile and a Poiseuille flow. Excellent agreement was found with previous computations for both the cases.

The instability of the flow can be of two types - *absolute instability* and *convective instability*. A flow is said to be absolutely unstable if localized disturbances spread upstream and downstream and influence the entire flow field. On the other hand, if the disturbances are swept away from the source but nevertheless increase in magnitude with time, the flow is said to be convectively unstable. Figure 65 shows schematically the two different types of instabilities.

To study the absolute instability, complex wavenumbers are selected and the corresponding most unstable wave frequencies are computed to determine the dispersion relation of complex k and complex ω. The point in the $k-\omega$ plane (ω_0, k_o) where $d\omega/dk = 0$ gives the branch point singularity of the dispersion relation. The disturbance will grow or decay at its location of generation depending on the sign of $\mathrm{Im}[\omega_o]$. The flow is absolutely unstable if the branch point singularity of its dispersion relation lies in the upper half of the complex ω plane ($\mathrm{Im}[\omega_o]>0$). To study convective instability of the flow, only real values of the wavenumbers are selected and the most unstable wave frequency computed. The disturbance will grow in time at a location away from the source (convectively unstable) if $\mathrm{Im}[\omega]>0$.

The stability of the flowfield was computed and analyzed. The velocity profiles at different chordwise locations and angles of attack, obtained from the numerical simulation, were studied. In *Case 1*, the primary recirculating region appears at approximately 15°. The stability analysis for this case showed that the flowfield is not absolutely unstable at any location in the front 50% of the chord up to an angle of attack of 18°, which is well past the angle at which the primary recirculating region appears. This demonstrates that the primary recirculating region does not form due to an absolute instability of the flow.

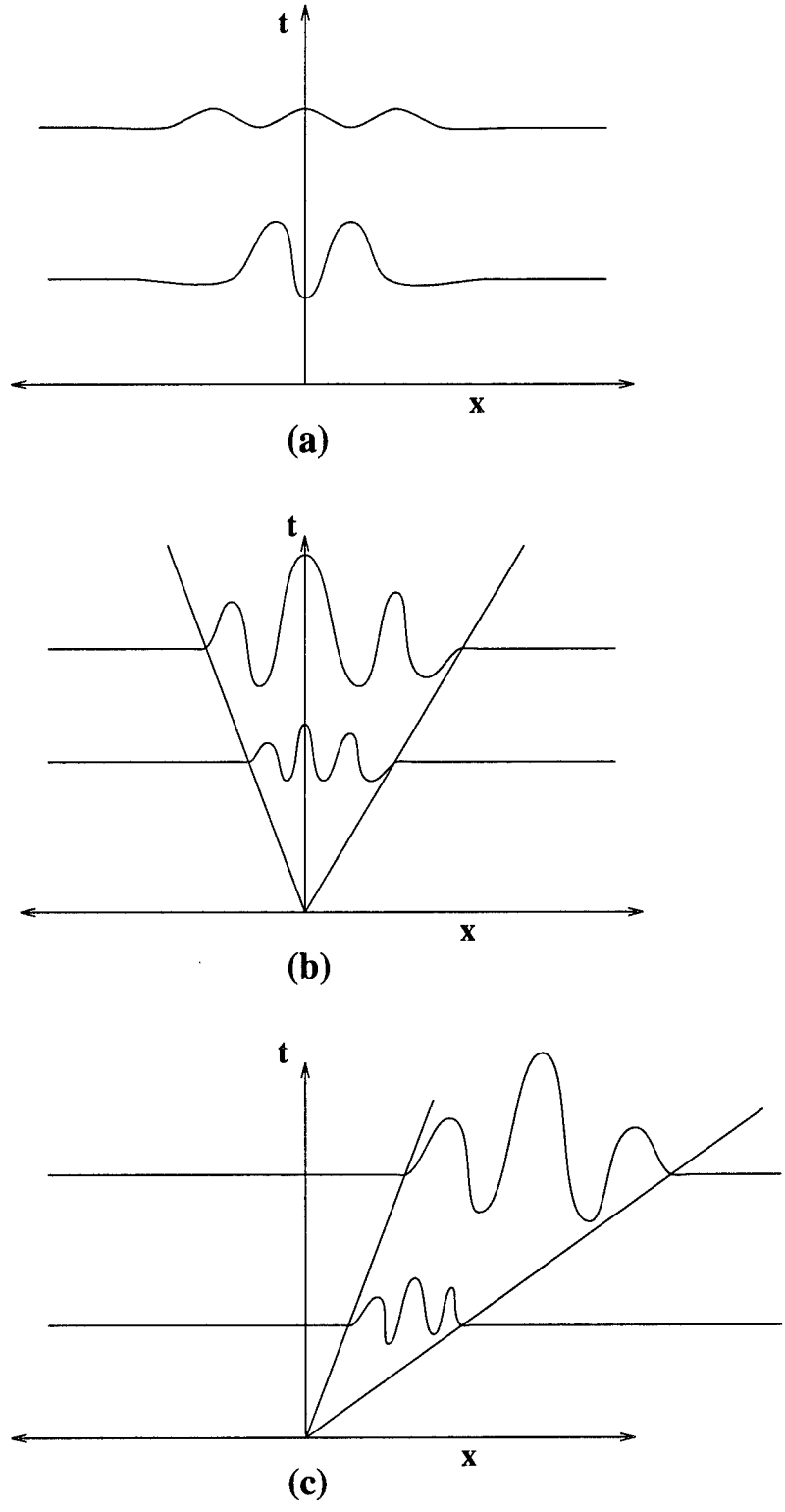

Figure 65: Sketch of a typical impulse response : (a) stable; (b) absolutely unstable; (c) convectively unstable

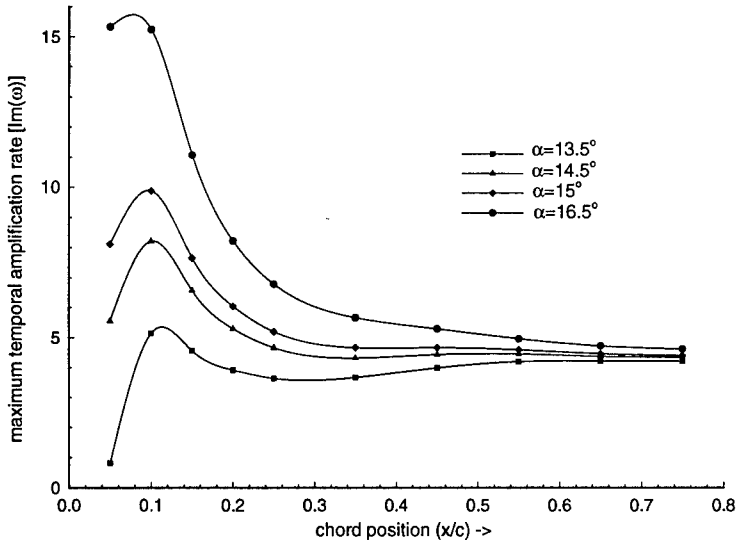

Figure 66: Maximum temporal growth rate of the disturbance in the flowfield at various chordwise positions on the airfoil and at different angles of attack (Case 1)

Convective stability analysis was conducted for *Case 1.* Figure 66 shows the maximum temporal growth rate for the velocity profiles at different chordwise positions of the airfoil for different angles of attack. Figure 67 shows the wavenumbers corresponding to the maximum temporal growth rate at different chord positions of the airfoil. It is seen that the flow is convectively unstable over the entire airfoil upper surface and the instability increases in magnitude with the increase in the angle of attack. The magnitude of convective instability is also higher in the region near the leading edge and increases at a faster rate with increase in the angle of attack as compared to the aft portion of the airfoil. From the numerical simulation we had seen that the primary recirculating region appears around 18% chord position for *Case 1.* Therefore it can be said that the appearance of the primary recirculating region may be due to the convective instability of the flowfield near the leading edge. The wavenumber of the disturbance (normalized by the chord length) corresponding to the maximum temporal growth rate at the 18% chord position is approximately 50 (figure 67), which corresponds to a wavelength of around 12.5% of the chord and corresponds roughly to the size of the primary recirculating region.

Figures 68 and 69 show the maximum temporal growth rate and the corresponding

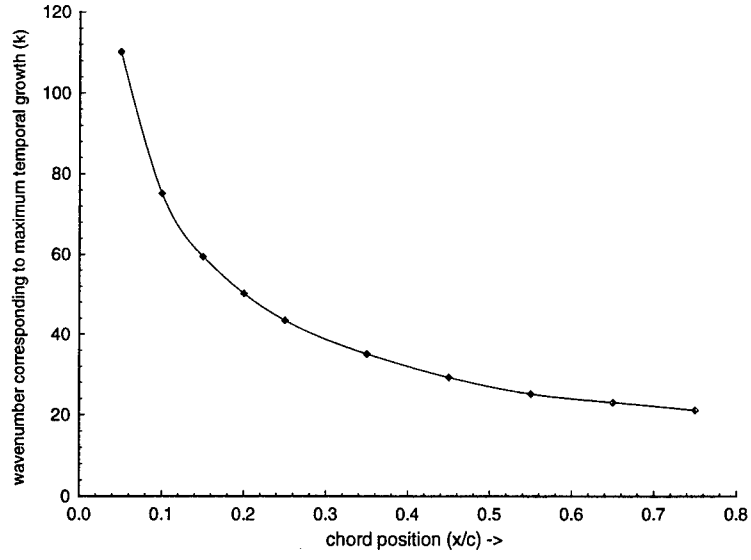

Figure 67: Wavenumber corresponding to maximum temporal growth rate of the disturbance at various chordwise positions on the airfoil and at different angles of attack (Case 1)

wave number at different chordwise positions and angles of attack for *Case 2*. *Case 2* represents a decrease in the pitch rate as compared to *Case 1* while the Mach number and Reynolds number are the same. It is observed that the magnitude of the instability (temporal amplification rate) is much higher for *Case 2* as compared to *Case 1* at any particular angle. This suggests that the primary recirculating region will appear at a smaller angle of attack for this case with respect to *Case 1*. A similar trend was observed in the numerical simulations which is shown in figure 62. The wavenumber (normalized by the chord length) corresponding to the maximum growth rate at the location where the primary recirculating region appears is approximately 40, which in turn relates to a disturbance wavelength of around 16% of the chord. Sections 9.1 and 9.3 describe that the decrease in the pitch rate at a constant Mach number and Reynolds number leads to an increase in the size of the primary recirculating region, which is also indicated in the linear stability analysis.

The linear stability analysis shows that the appearance of the primary recirculating region is related to the convective instability of the flowfield near the leading edge of the airfoil. The wavelength of the disturbance is comparable to the size of the primary

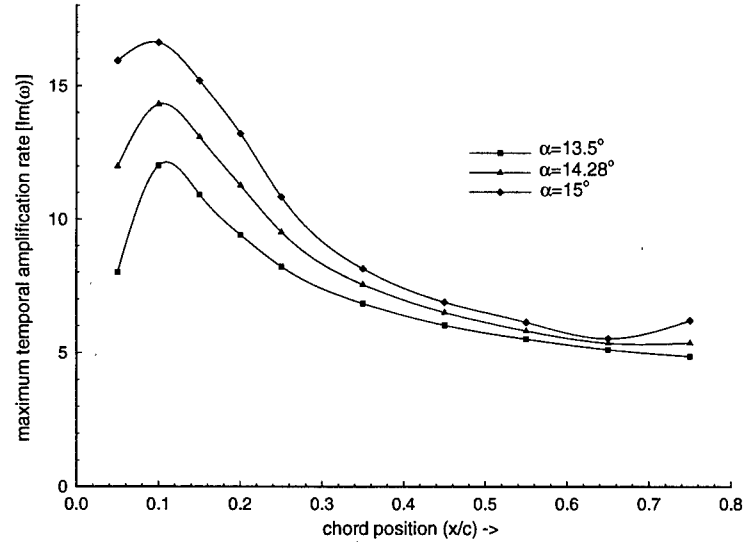

Figure 68: Maximum temporal growth rate of the disturbance in the flowfield at various chordwise positions on the airfoil and at different angles of attack (Case 2)

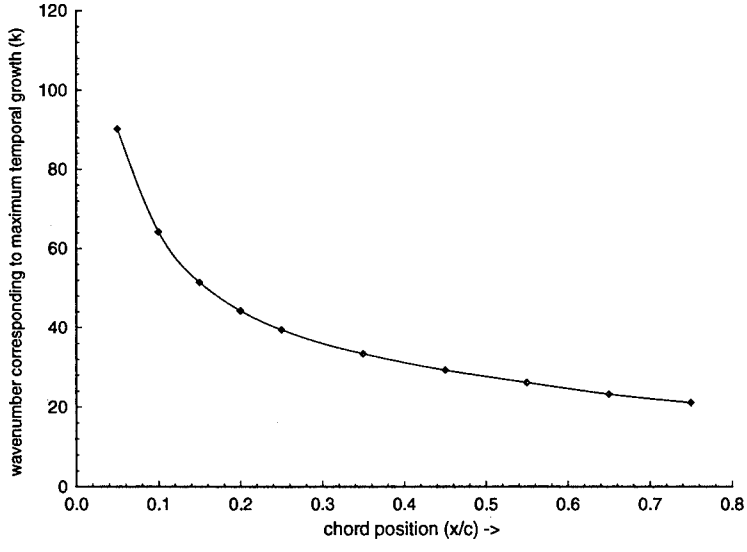

Figure 69: Wavenumber corresponding to maximum temporal growth rate of the disturbance at various chordwise positions on the airfoil and at different angles of attack (case 2)

recirculating region as seen from the full Navier-Stokes simulations. The trend with regards to the effect of change in pitch rate on the size of the primary recirculating region and the angle at which it first appears matches with the observations from the direct numerical simulation.

9.13 Flow Control

Control of dynamic stall is very important to effectively utilize it in unsteady aerodynamic applications. There have been very few studies in the past to investigate different flow control techniques to delay dynamic stall. The active control using modulated suction/injection to manage the dynamic stall vortex has been studied the most and has been quite successful. But, there are practical problems in incorporating this control technique in the small blades of the helicopter rotor.

The present research project has been successful in tracing the formation of the dynamic stall vortex to a critical point in the flowfield. This information may be very useful in investigating different flow control methods because it gives an idea with respect to the location in the flowfield where flow control has to be applied to be most effective.

A study was conducted to delay the formation of the primary recirculating region by preferential heating and cooling of the entire airfoil surface. It has been observed in the results presented that the formation of the primary recirculating region depends to a great extent on the magnitude of the adverse pressure gradient on the airfoil upper surface. At higher Mach numbers, the leading edge suction pressure coefficient decreases as compared to that at lower Mach numbers. This leads to a decrease in the adverse pressure gradient on the airfoil upper surface and an eventual delay in the formation of the primary recirculating region. The same idea of decreasing the leading edge suction pressure coefficient can be utilized to delay the formation of the primary recirculating region. A preferential heating of the region near the leading edge and cooling of the trailing edge region can effectively lead to a decrease in the leading edge pressure coefficient and increase in pressure coefficient near the trailing edge. This on the other hand may lead to a decrease in the adverse pressure coefficient on the airfoil upper surface.

Simultaneous heating of the leading edge region and cooling of the trailing edge

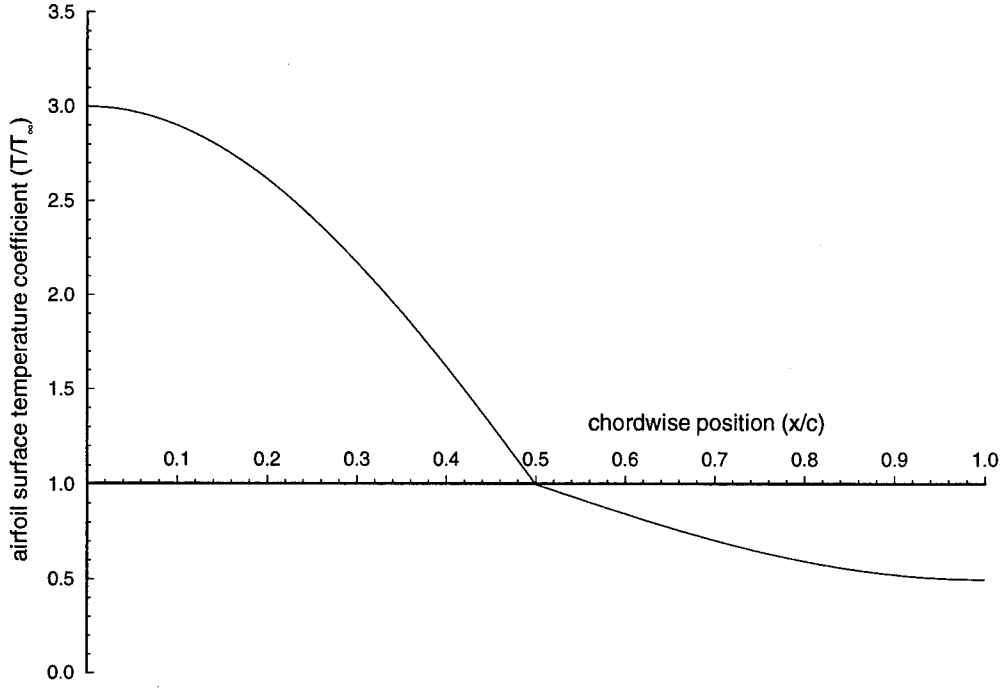

Figure 70: Profile of the temperature applied on airfoil surface

region was applied to Case 1 ($Re_c = 10^4$, $M_\infty = 0.2$, $\Omega_o^+ = 0.2$). Both upper and lower surfaces of the airfoil were either heated or cooled for simplicity. The temperature profile that was applied on the airfoil surface is shown as a function of the chordwise position in figure 70. The profile is a modified sinusoidal function. The temperature was applied to the surface at the start of the pitch up motion of the airfoil from zero degrees as an exponential function of time to reach the final value shown in the figure at approximately 1°.

The instantaneous streamlines over the airfoil for Case 1 with modulated heating and cooling are shown in figures 71 to 75 at $\alpha = 13.5°$, 15.0°, 16.5°, 18.0°, and 21.0°. At $\alpha = 13.5°$, there is already reversed flow over the entire airfoil upper surface. There are also two recirculating regions present near the trailing edge but none near the leading edge. By $\alpha = 15.0°$, the reversed flow has considerably increased in thickness and is of the order of the thickness of the airfoil. But, there is no presence of primary recirculating region near the leading edge. For Case 1 without heating, it was seen that the primary recirculating region appeared at $\alpha = 15.0°$ at 18% chord position and the reversed flow was much thinner. Figure 73 shows the presence of the primary recirculating region near

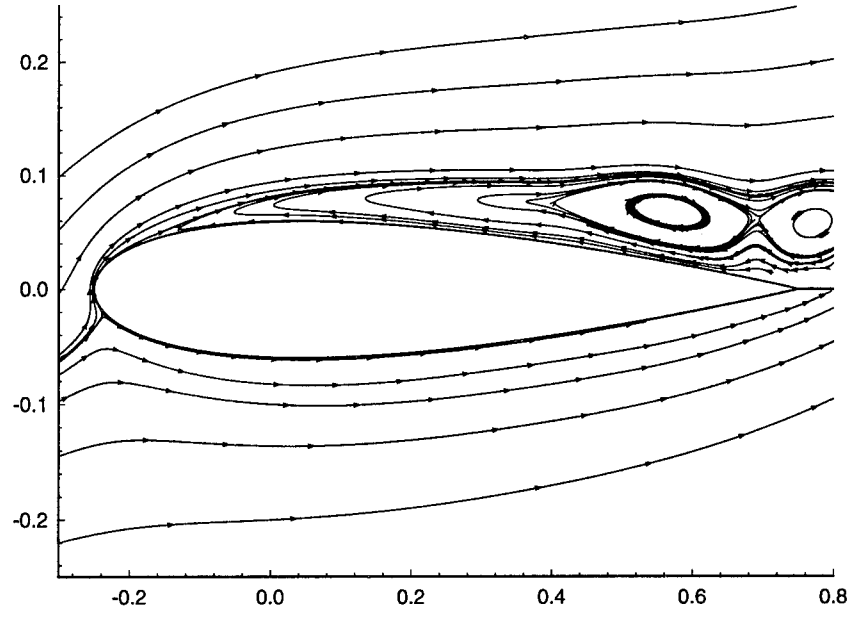

Figure 71: Instantaneous streamlines at $\alpha = 13.5°$ for Case 1 with modulated heating and cooling

the leading edge at $\alpha = 16.5°$. In fact, the primary recirculating region appears due to a breakup of the trailing edge vortex and at approximately 60% chord position. The primary recirculating region grows in size with increase in the angle of attack and moves upstream. This is shown in figure 74 at $\alpha = 18.0°$. The secondary recirculating region can be seen at $\alpha = 21.90°$ in figure 75. The development of the flowfield is very similar to the case where there is no modulated heating or cooling. The difference in the two cases is the position of the primary recirculating region and the angle of attack of its first appearance. Modulated heating delays the formation of the primary recirculating region by about 1°. The recirculating region also appears at a farther distance from the leading edge and the airfoil upper surface as compared to the case without any heating. The flow structures are much bigger in size and cover the entire airfoil upper surface.

The surface pressure coefficients are shown in figures 76 to 79. The figures show a comparison of the surface pressure coefficients for Case 1 without heating, Case 1 with modulated heating and cooling, and Case 4 (which denotes the effect of increase in compressibility). From the figures it can be seen that modulated heating of the leading edge region and cooling of the trailing edge region of the airfoil surface leads to

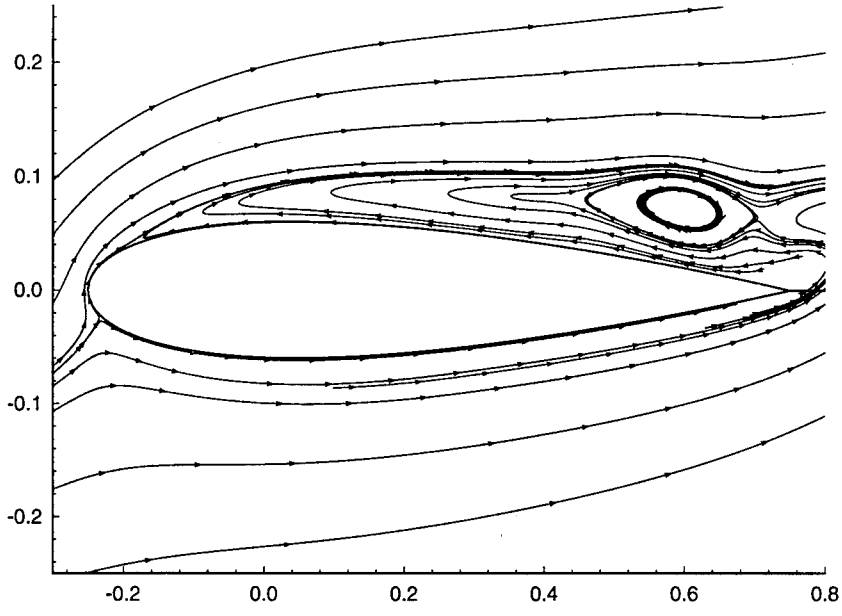

Figure 72: Instantaneous streamlines at $\alpha = 15.0°$ for Case 1 with modulated heating and cooling

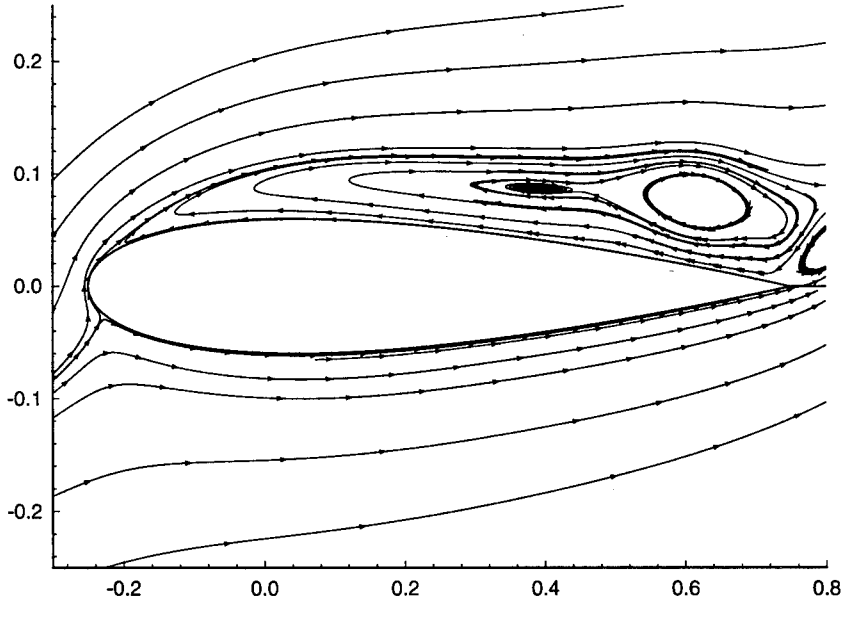

Figure 73: Instantaneous streamlines at $\alpha = 16.5°$ for Case 1 with modulated heating and cooling

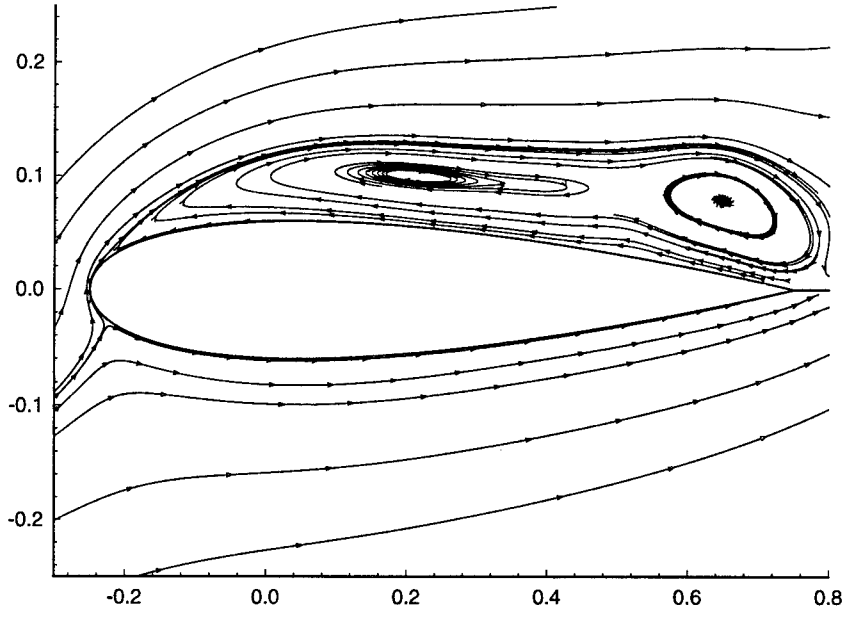

Figure 74: Instantaneous streamlines at $\alpha = 18.0°$ for Case 1 with modulated heating and cooling

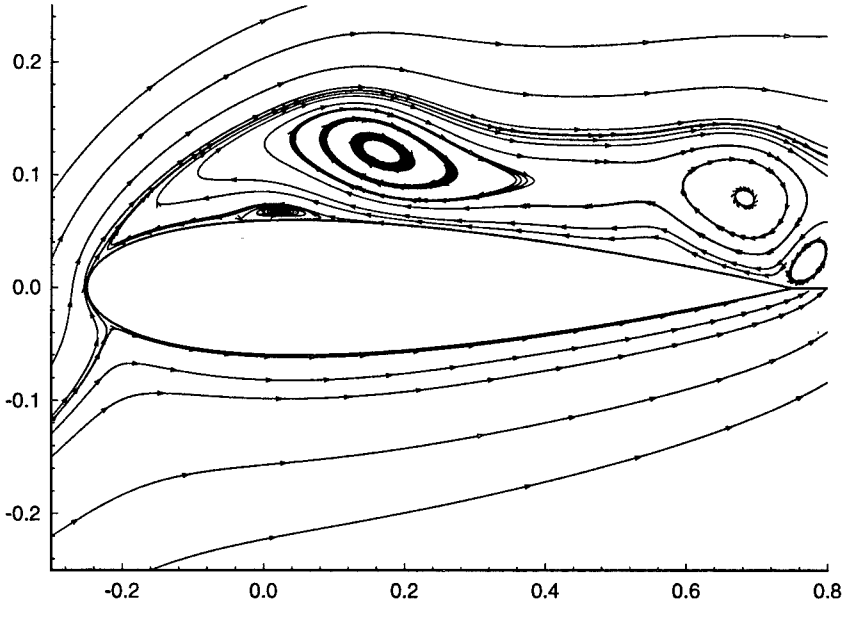

Figure 75: Instantaneous streamlines at $\alpha = 21.0°$ for Case 1 with modulated heating and cooling

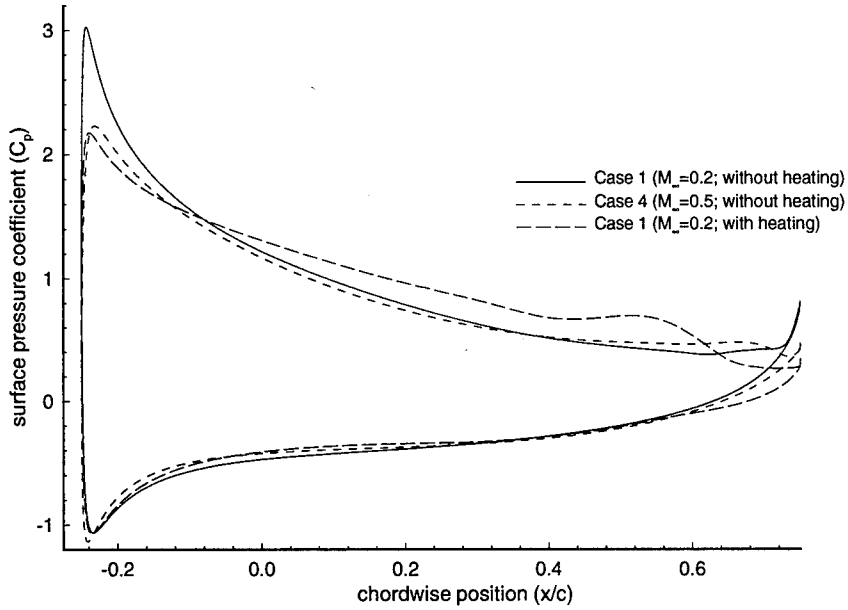

Figure 76: Surface pressure coefficient at $\alpha = 13.5°$

a substantial drop in the leading edge suction coefficient which is comparable to that at $M_\infty = 0.5$. The adverse pressure gradient on the airfoil surface is also less when the airfoil surface is heated. But, as is seen from the instantaneous streamline plots, this does not prevent the formation of the reversed flow region on the airfoil upper surface.

To summarize, it can be said that modulated heating and cooling of the airfoil surface does not delay the formation of the primary recirculating region by more than 2-3 degrees. It is not a very efficient way of controlling dynamic stall. Further studies need to be done to test other flow control techniques like generation of acoustic pulses on the airfoil surface to delay the formation of the primary recirculating region.

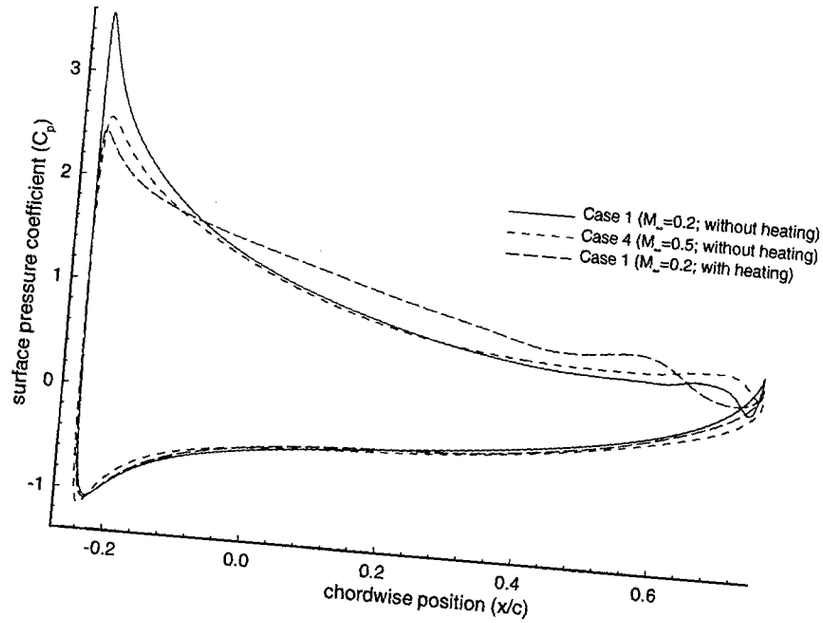

Figure 77: Surface pressure coefficient at $\alpha = 15.0°$

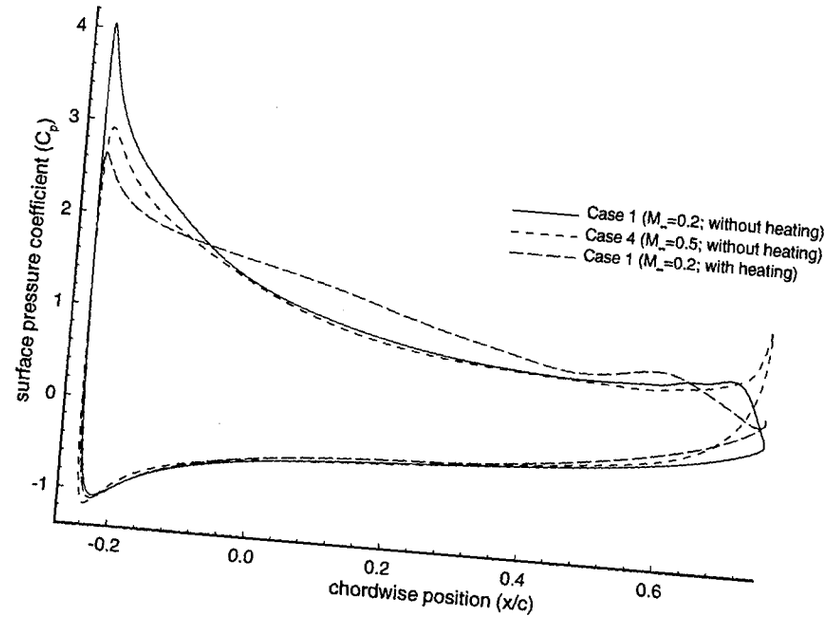

Figure 78: Surface pressure coefficient at $\alpha = 16.5°$

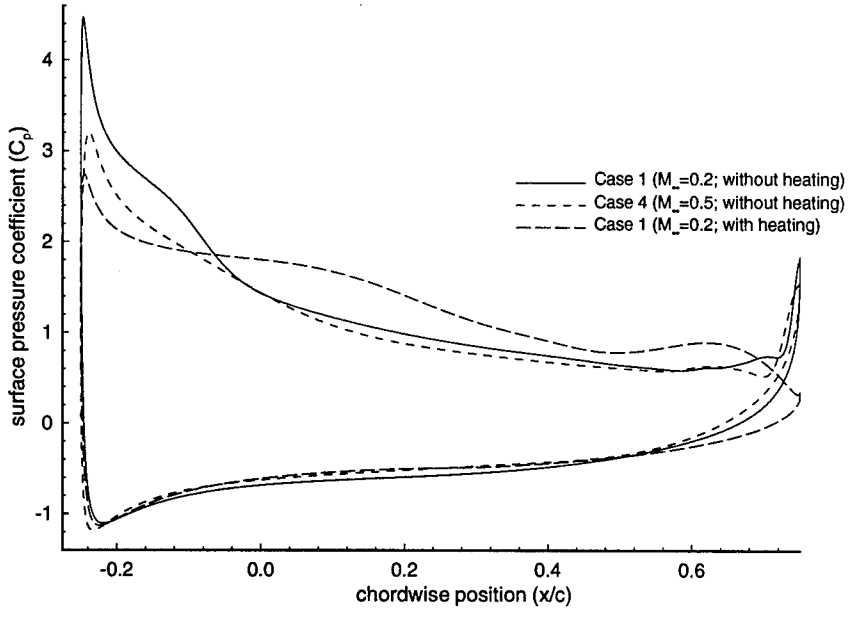

Figure 79: Surface pressure coefficient at $\alpha = 18°$

Table 4: CPU and Memory Requirements for the computations on Cray C90

Case	Memory (in Mw)	CPU-time (in hours)
1c	9.8	7
7b	128	125

9.14 Code Performance

The Navier-Stokes solver is fully-vectorized and was run on the Cray C90. Some typical CPU-time and memory requirements for the computations are shown in Table 4. The solver has a sustained performance of approximately 380 MFLOPS.

10 CONCLUSIONS AND SCOPE OF FUTURE WORK

10.1 Summary

The effects of compressibility, pitch rate and Reynolds number on the initial stages of boundary-layer separation on a NACA-0012 airfoil pitching about its quarter chord position have been studied numerically. Computations have been performed using two separate algorithms for the compressible laminar Navier-Stokes equations. The first method, denoted the *structured grid algorithm*, utilizes a structured, boundary-fitted C-grid and employs the implicit approximate-factorization algorithm of Beam and Warming. The solver was developed originally by Visbal [48, 49] for an O-grid topology and has been modified to employ a C-grid, Method of Characteristics boundary condition at the outer boundary and the Geometric Conservation Law to eliminate the grid movement related errors. The second method, denoted the *unstructured grid algorithm*, utilizes an unstructured grid of triangles and employs the flux-difference splitting method of Roe and a discrete representation of Gauss' Theorem for the inviscid and viscous terms, respectively. A number of steady and unsteady computations have been performed to prove the accuracy of the two algorithms, including the boundary layer over a flat plate, stationary NACA-0012 airfoil at $\alpha = 0°$, and pitching NACA-0015 airfoil. The test cases were compared with available analytical solutions or previous computations. The effects of implicit and explicit artificial dissipation, and the temporal and spatial resolution have been studied in detail for the research problem. Accurate grid-converged solutions have been obtained for the flow.

The principal results of the study are :

- The emergence of the primary recirculating region has been traced to a pair of

critical points (a center and a saddle) that form as a pure shear at a single point and immediately bifurcate and move apart.

- Secondary and tertiary recirculating regions form after the appearance of the primary recirculating region. The secondary recirculating region interacts with the primary recirculating region to eject the fluid close to the wall in a direction approximately normal to the wall. The ejection of the fluid near the wall signifies boundary layer separation.

- The accuracy of the computations has been confirmed by the close agreement between the structured and unstructured grid computations, and the grid refinement study for the structured grid computations.

Mach number

- Increase in Mach number from 0.2 to 0.5 (at fixed Reynolds number and pitch rate) delays the formation of the primary recirculating region and causes it to form farther from the airfoil surface. The compressibility effects on the boundary layer result in a decrease in the magnitude of the leading edge suction pressure coefficient and a consequent decrease in the adverse pressure gradient on the upper surface. The decrease in adverse pressure gradient retards the movement of reversed flow region towards the leading edge and hence delays the formation of the primary recirculating region.

Pitch rate

- Increase in pitch rate from 0.05 through 0.2 (at fixed Mach number and Reynolds number) causes the transition from trailing edge separation to leading edge separation.

- Increase in pitch rate delays the formation of the primary recirculating region to higher angles of attack. This is due to the decrease in the adverse pressure gradient on the airfoil upper surface which retards the development of the reversed flow region on the upper surface and the formation of the primary recirculating region. The primary recirculating region also appears closer to the leading edge.

Reynolds number

- Increasing the Reynolds number from 10^4 to 10^5 (at fixed Mach number and pitch rate) hastens the appearance of the primary recirculating region and decreases the length scale of the flow structures.
- Multiple recirculating regions appear simultaneously near the leading edge.

Shock wave

- A shock appears on the top surface at $Re_c = 10^5$, $M_\infty = 0.5$, and $\Omega_o^+ = 0.2$ at $\alpha = 19.5°$. A separate inviscid computation also showed a similar appearance of shock, implying the formation of the shock is an inviscid phenomenon. For the inviscid case, the shock appears closer to the leading edge and also at an earlier angle of attack as compared to the viscous case.
- The formation of the recirculating regions near the leading edge was found not to be induced by the shock.

Stability analysis

- Linear stability analysis of the computed flowfield shows that the formation of the primary recirculating region is related to the convective instability of the flow. It also confirms the trend seen in the the numerical simulations with regards to the effect of change in pitch rate on the appearance of the primary recirculating region.

10.2 Future Work

The field of unsteady aerodynamics is relatively in the nascent stage. A substantial amount of research has recently focused on the study of the complex unsteady effects in the flow over a pitching and oscillating airfoil so that ultimately the unsteady effects of a pitching airfoil may be utilized to an advantage in the design of aerodynamic bodies. The present work presented in this dissertation has concentrated on the study of incipient stages of unsteady boundary layer separation and the effects of compressibility, pitch rate and Reynolds number on the separation process. Computations are still limited to

relatively low Reynolds number flows (with respect to practical range) due to the memory restrictions of the computer. Their remains scope for future study in the following areas :

- Practical aerodynamic flows have Reynolds number based on the chord of the order of 10^6. Increasing Re_c leads to more expensive computations, both in terms of memory and CPU. Robust and efficient algorithms have to be developed to solve such flows. The use of parallel computers may be the answer to the problem.

- Flow at high Re_c is mainly turbulent. However, there are not any turbulence models which can accurately simulate the flow in the separated regions [6]. Proper turbulence models need to be developed for such flows.

- Study of 3-D effects can also be described as important. But, the computer resources available at the present time does not allow an accurate simulation for 3-D flowfields.

- The control of dynamic stall process is a very important problem that needs to be addressed. In this study, the formation of the dynamic stall vortex has been traced to a pair of critical points in the flow field. It might be of interest to apply different flow control techniques at the location of the formation of these points to ultimately delay the formation of the dynamic stall vortex.

11 LIST OF PUBLICATIONS

1. Knight, D. D., "A Fully Implicit Navier-Stokes Algorithm Using an Unstructured Grid and Flux Difference Splitting", AIAA Paper No. 93-0875, 1993.

2. Ghosh Choudhuri, P., Knight, D. D., Visbal M. R., "2-D Unsteady Separation on a Pitching Airfoil", 1993 ASME Division of Fluids Engineering Spring Meeting-Forum on Unsteady Flows, Washington D.C., June 1993.

3. Knight, D. D., Ghosh Choudhuri, P., "2-D Unsteady Leading Edge Separation on a Pitching Airfoil", AIAA Paper No. 93-2977, 1993.

4. Ghosh Choudhuri, P., Knight, D. D., Visbal M. R., "Two-Dimensional Unsteady Leading-Edge Separation on a Pitching Airfoil", *AIAA Journal*, Vol. 32, April 1994, pp. 673-681.

5. Knight, D. D., "A Fully Implicit Navier-Stokes Algorithm Using an Unstructured Grid and Flux Difference Splitting", *Applied Numerical Mathematics*, Vol. 16, No. 1/2, December 1994, pp. 101-128.

6. Ghosh Choudhuri, P., Knight, D. D., "Effects of Compressibility, Pitch rate and Reynolds Number on Unsteady Incipient Boundary Layer Separation Over a Pitching Airfoil", AIAA Paper No. 95-0782, 1995.

7. Ghosh Choudhuri, P., Knight, D. D., "Effects of Compressibility, Pitch rate and Reynolds Number on Unsteady Incipient Leading-Edge Boundary Layer Separation Over a Pitching Airfoil", submitted to *Journal of Fluid Mechanics.*

12 LIST OF PERSONNEL AND DEGREES AWARDED

12.1 Personnel

Principal Investigator :

Prof. Doyle D. Knight

Department of Mechanical and Aerospace Engineering

Rutgers University

Graduate Research Assistant :

Mr. Pushkar Ghosh Choudhuri

Department of Mechanical and Aerospace Engineering

Rutgers University

12.2 Degrees Awarded

1. Ghosh Choudhuri, P., "Initial Stages of 2-D Unsteady Leading Edge Separation on a Pitching Airfoil", M. S. Thesis, Department of Mechanical and Aerospace Engineering, Rutgers University, May 1993.

2. Ghosh Choudhuri, P., "Effects of Compressibility, Pitch Rate and Reynolds Number on Unsteady Incipient Leading-Edge Boundary Layer Separation Over a Pitching Airfoil", Ph.D. Dissertation, Department of Mechanical and Aerospace Engineering, Rutgers University, May 1995.

References

[1] Acharya, M., Metwally, M. Evolution of the Unsteady Pressure Field and Vorticity Production at the Surface of a Pitching Airfoil. AIAA Paper No. 90-1472, 1990.

[2] Beam, Richard M., and Warming, R. F. An Implicit Factored Scheme for the Compressible Navier-Stokes Equations. *AIAA Journal*, Vol. 15, 1978, pp. 393-402.

[3] Beran, P. Steady and Unsteady Solutions of the Navier-Stokes Equations for Flows About Airfoils at Low Speeds. AIAA Paper No. 91-1733, 1991.

[4] Carr, L. Progress in Analysis and Prediction of Dynamic Stall. *Journal of Aircraft*, Vol. 25, 1988, pp. 6-17.

[5] Carr, L., Chandrashekhara, M. S., Brock, N. A Quantitative Study of Unsteady Compressible Flow on an Oscillating Airfoil. AIAA Paper No. 91-1683, 1991.

[6] Carr, L. W., and McCroskey, W. J. A Review of Recent Advances in Computational and Experimental Analysis of Dynamic Stall. IUTAM Symposium on Fluid Dynamics of High Angle of Attack, Tokyo, Japan, 1992.

[7] Chandrashekhara, M. S., and Carr, L. Flow Visualization of the Mach Number Effects on the Dynamic Stall of an Oscillating Airfoil. AIAA Paper No. 89-0023, 1989.

[8] Chandrashekhara, M. S., Ahmed, S. Laser Velocimetry Measurements of Oscillating Airfoil Dynamic Stall Flow Field. AIAA Paper No. 91-1799, 1991.

[9] Chandrashekhara, M. S., Carr, L. W., and Wilder, M. C. Interferometric Investigations of Compressible Dynamic Stall Over a Transiently Pitching Airfoil. *AIAA Journal*, Vol. 32, 1994, pp. 586-593.

[10] Chong, M., Perry, A. A General Classification of Three-Dimensional Flow Fields. *Topological Fluid Dynamics - Proceedings of the IUTAM Symposium*, H. Moffatt and A. Tsinober, ed., Cambridge University Press, 1990.

[11] Crisler, W., Krothapalli, A., and Lourenco, L. PIV Investigation of High Speed Flow Over a Pitching Airfoil. AIAA Paper No. 94-0533, 1994.

[12] Currier, J. M., and Fung, K. Y. Analysis of the Onset of Dynamic Stall. *AIAA Journal*, Vol. 30, 1992, pp. 2469-2477.

[13] Doligalski, T. L., Smith, C. R., and Walker, J. D. A. Vortex Interaction with Walls. *Annual Review of Fluid Mechanics*, Vol. 26, 1994, pp. 573-616.

[14] Ghia, K. N., Yang, J., Osswald, G. A., Ghia, U. Study of the Dynamic Stall Mechanism Using Simulation of Two-Dimensional Navier-Stokes Equations. AIAA Paper No. 91-0546, 1991.

[15] Ghia, K. N., Yang, J., Osswald, G. A., Ghia, U. Study of the Role of Unsteady Separation in the Formation of Dynamic Stall Vortex. AIAA Paper No. 92-0196, 1992.

[16] Ghosh Choudhuri, P., Knight, D., and Visbal, M. Two-Dimensional Unsteady Leading-Edge Separation on a Pitching Airfoil. *AIAA Journal*, Vol. 32, 1994, pp. 673-681.

[17] Kaplan, W. *Ordinary Differential Equations.* Addison-Wesley, Reading, MA, 1991.

[18] Karim, Md. A. Experimental Investigation of the Formation and Control of the Dynamic-Stall Vortex Over a Pitching Airfoil. MS Thesis, Illinois Institute of Technology, 1992.

[19] Kinsey, Don W., Barth, Timothy J. Description of a Hyperbolic Grid Generating Procedure for Arbitrary Two-Dimensional bodies. AFWAL-TM-84-191, 1984.

[20] Knight, D. D. A fully implicit Navier-Stokes Algorithm Using an Unstructured Grid and Flux-Difference Splitting. *Applied Numerical Mathematics*, Vol. 16, No. 1/2, 1994, pp. 101-128.

[21] Liepmann, H., and Roshko, A. *Elements of Gas Dynamics.* John Wiley & Sons, Inc., 1957.

[22] Martinelli, L., and Jameson, A. Validation of a Multigrid Method for the Reynolds Averaged Equations. AIAA Paper No. 88-0414, 1988.

[23] McCroskey, W. J., and Philippe, J. Unsteady Viscous Flow on Oscillating Airfoils. *AIAA Journal*, Vol. 13, 1975, pp. 71-79.

[24] McCroskey, W. J., Carr, L., and McAlister, K. Dynamic Stall Experiments on Oscillating Airfoils. *AIAA Journal*, Vol. 14, 1976, pp. 51-62.

[25] Mehta, U. Starting Vortex, Separation Bubbles and Stall : A Numerical Study of Laminar Unsteady Flow Around an Airfoil. *Journal of Fluid Mechanics*, Vol. 67, 1976, pp. 227-256.

[26] Mehta, U. Dynamic Stall of an Oscillating Airfoil. *AGARD CP-227, Unsteady Aerodynamics*, 1977.

[27] Merriam, M. UNSTRUCT - An Unstructured Grid Generator for the Iris Workstation. NASA Ames Research Center, 1991.

[28] Peridier, Vallorie J., Smith, F. T., and Walker, J. D. A. Vortex-induced Boundary-layer Separation. Part 1. The Limit Problem Re $\rightarrow \infty$. *Journal of Fluid Mechanics*, Vol. 232, 1991, pp. 99-131.

[29] Peridier, Vallorie J., Smith, F. T., and Walker, J. D. A. Vortex-induced Boundary-layer Separation. Part 2. Unsteady Interacting Boundary-layer Theory. *Journal of Fluid Mechanics*, Vol. 232, 1991, pp. 133-165.

[30] Perry, A. E., and Chong, M. S. A Description of Eddying Motions and Flow Patterns Using Critical-Point Concepts. *Annual Review of Fluid Mechanics*, Vol. 19, 1987, pp. 125-155.

[31] Pontryagin, L. S. *Ordinary Differential Equations.* Addison-Wesley, Reading, MA, 1962.

[32] Pulliam, Thomas H. Artificial Dissipation Models for the Euler Equations. *AIAA Journal*, Vol. 24, No. 12, 1986, pp. 1931-1940.

[33] Rausch, R., Batina, J., and Yang, H. Spatial Adaption Procedures on Unstructured Meshes for Accurate Unsteady Aerodynamic Flow Computation AIAA Paper No. 91-1106, 1991.

[34] Roe, P. L. Approximate Riemann Solvers, Parameter Vectors, and Difference Schemes. *J. Comp. Physics*, Vol. 43, 1981, pp. 357-372.

[35] Sankar, N. L., and Tassa, Y. Compressibility Effects on Dynamic Stall of an NACA-0012 Airfoil. *AIAA Journal*, Vol. 19, 1981, pp. 557-558.

[36] Shida, Y., Takami, H., Kuwahara, K., and Ono, K. Computation of Dynamic Stall of NACA0012 Airfoil by Block Pentadiagonal Matrix Scheme. AIAA Paper No. 86-0116, 1986.

[37] Shih, C.,Lourenco, L., Van Dommelen, L., Krothapalli, A. Unsteady Flow Past an Airfoil Pitching at a Constant Rate. *AIAA Journal*, Vol. 30, No. 5, 1992, pp. 1153-1161.

[38] Smith, F. T. Concerning Dynamic Stall. *Aeronautical Quarterly*, Vol. 33, 1982, pp. 331-352.

[39] Smith, F. T. On the Abrupt Turbulent Reattachment Downstream of Leading-edge Laminar Separation. *Proceedings of The Royal Society of London A*, Vol. 401, 1985, pp. 1-27.

[40] Smith, F. T. Steady and Unsteady Boundary Layer Separation. *Annual Review of Fluid Mechanics*, Vol. 18, 1986, pp. 197-220.

[41] Smith, F. T. Finite-time Break-up can Occur in Any Unsteady Interacting Boundary Layer. *Mathematika*, Vol. 35, 1989, pp. 256-273.

[42] Sorenson, R. A Computer Program to Generate Two-Dimensional Grids About Airfoils and Other Shapes by the Use of Poisson's Equation. NASA TM 81198.

[43] Steger, J. Implicit Finite-Difference Simulation of Flow About Arbitrary Two-Dimensional Geometries. *AIAA Journal*, Vol. 16, No. 7, 1978, pp. 679-686.

[44] Thomas, P. D., and Lombard, C. K. Geometric Conservation Law and its Applications to Flow Computations on Moving Grids. *AIAA Journal*, Vol. 17, 1979, pp. 1030-1037.

[45] Thomas, James L., and Salas, M. D. Far-Field Boundary Conditions for Transonic Lifting Solutions to the Euler Equations. *AIAA Journal*, Vol. 24, 1986, pp. 1074-1080.

[46] Van der Vorst, H. BI-CGSTAB : A Fast and Smoothly Converging Variant of BI-CG for the Solution of Nonsymmetric Linear Systems. *SIAM Journal on Scientific and Statistical Computing*, Vol. 13, No. 2, 1992, pp. 631-644.

[47] Van Dommelen, Leon L., and Cowley, Stephen J. On the Lagrangian Description of Unsteady Boundary-layer Separation. Part 1. General Theory. *Journal of Fluid Mechanics*, Vol. 210, 1990, pp. 593-626.

[48] Visbal, Miguel R. Calculations of Viscous Transonic Flows About a Supercritical Airfoil. AFWAL-TR-86-3013, 1986.

[49] Visbal, M. R. Evaluation of an Implicit Navier-Stokes Solver for Some Unsteady Separated Flows. AIAA Paper No. 86-1053, 1986.

[50] Visbal, M. R., Shang, J. S. Investigation of the Flow Structure Around a Rapidly Pitching Airfoil. *AIAA Journal*, Vol. 27, No. 8, 1989, pp. 1044-1051.

[51] Visbal, Miguel R. Dynamic Stall of a Constant-Rate Pitching Airfoil. *Journal of Aircraft*, Vol. 27, No. 5, 1990, pp. 400-407.

[52] Visbal, Miguel R. On the Formation and Control of the Dynamic Stall Vortex on a Pitching Airfoil. AIAA Paper No. 91-0006, 1991.

[53] Walker, J. Unsteady Boundary Layer Separation in Two-Dimensional Flows. Workshop on Supermaneuverability : Physics of Unsteady Separated Flows at High Angle of Attack, Lehigh University, Bethelehem, PA, 1992.

[54] Walker, J. Issues Relating to Unsteady Separation at High Reynolds Number. 1992 Computational Fluid Dynamics Symposium, Wright-Patterson AFB, OH, 1992.

[55] Warming, R. F., and Beam, R. M. On the Construction and Application of Implicit Factored Schemes for Conservation Laws. *SIAM-AMS Proceedings*, Vol. 11, 1978, pp. 85-129.

[56] White, Frank M. *Viscous Fluid Flow.* McGraw-Hill, New-York, 1974.

[57] Whittaker, D., Slack, R., and Walters, R. Solution Algorithms for the Two-Dimensional Euler Equations on Unstructured Meshes. AIAA Paper No. 90-0697, 1990.

[58] Yang, J., Ghia, K., Ghia, U., and Osswald, G. Management of Dynamic Stall Phenomenon Through Active Control of Unsteady Separation. AIAA Paper No. 93-3284, 1993.

[59] Zebib, A. A Chevyshev Method for the Solution of Boundary Value Problems. *Journal of Computational Physics*, Vol. 53, 1984, pp. 443-455.

A Jacobian Matrices for Structured Grid Algorithm

Explicit form of the Jacobian matrices has been presented in this appendix. The matrices are obtained analytically by rewriting the matrices F, G, V_1, V_2, W_1, and W_2 in terms of ρ/J, $\rho u/J$, $\rho v/J$, and $\rho e/J$ and differentiating according to eqn. (21) and eqns. (25) to (29).

The Jacobian matrices A and B given by eqns. (21) and (25), respectively are :

$$A = \begin{pmatrix} \xi_t & \xi_x & \xi_y & 0 \\ \xi_x\phi - uU & \mathcal{U} - (\gamma-2)\xi_x u & \xi_y u - (\gamma-1)\xi_x v & (\gamma-1)\xi_x \\ \xi_y\phi - vU & \xi_x v - (\gamma-1)\xi_y u & \mathcal{U} - (\gamma-2)\xi_y v & (\gamma-1)\xi_y \\ \mathcal{U}(2\phi - \gamma e) & (\gamma e - \phi)\xi_x - (\gamma-1)uU & (\gamma e - \phi)\xi_y - (\gamma-1)vU & \gamma U + \xi_t \end{pmatrix} \tag{108}$$

where

$$U = \mathcal{U} - \xi_t; \qquad V = \mathcal{V} - \eta_t; \qquad \phi = \frac{1}{2}(\gamma-1)(u^2+v^2) \tag{109}$$

$\mathcal{U}$ and $\mathcal{V}$ are the contravariant velocities described by eqn. (7).

$$B = \begin{pmatrix} \eta_t & \eta_x & \eta_y & 0 \\ \eta_x\phi - uV & \mathcal{V} - (\gamma-2)\eta_x u & \eta_y u - (\gamma-1)\eta_x v & (\gamma-1)\eta_x \\ \eta_y\phi - vV & \eta_x v - (\gamma-1)\eta_y u & \mathcal{V} - (\gamma-2)\eta_y v & (\gamma-1)\eta_y \\ \mathcal{V}(2\phi - \gamma e) & (\gamma e - \phi)\eta_x - (\gamma-1)uV & (\gamma e - \phi)\eta_y - (\gamma-1)vV & \gamma V + \eta_t \end{pmatrix} \tag{110}$$

Equations (27) and (29) define the Jacobian matrices R and S, respectively.

$$R = \frac{1}{\rho}\begin{pmatrix} 0 & 0 & 0 & 0 \\ -(b_1 u + b_2 v) & b_1 & b_2 & 0 \\ -(b_2 u + b_3 v) & b_2 & b_3 & 0 \\ R_{41} & R_{42} & R_{43} & R_{44} \end{pmatrix} \tag{111}$$

where

$$R_{41} = -\{b_1 u^2 + 2b_2 uv + b_3 v^2 + b_4 \gamma(\gamma-1)(u^2+v^2-e)\} \tag{112}$$

$$R_{42} = \{b_1 - b_4\gamma(\gamma-1)\}u + b_2 v \tag{113}$$

$$R_{43} = b_2 u + \{b_3 - b_4\gamma(\gamma-1)\}v \tag{114}$$

$$R_{44} = b_4\gamma(\gamma-1) \tag{115}$$

$$S = \frac{1}{\rho}\begin{pmatrix} 0 & 0 & 0 & 0 \\ -(d_1 u + d_2 v) & d_1 & d_2 & 0 \\ -(d_2 u + d_3 v) & d_2 & d_3 & 0 \\ S_{41} & S_{42} & S_{43} & S_{44} \end{pmatrix} \tag{116}$$

where

$$S_{41} = -\{d_1 u^2 + 2d_2 uv + d_3 v^2 + d_4\gamma(\gamma-1)(u^2+v^2-e)\} \tag{117}$$

$$S_{42} = \{d_1 - d_4\gamma(\gamma-1)\}u + d_2 v \tag{118}$$

$$S_{43} = d_2 u + \{d_3 - d_4\gamma(\gamma-1)\}v \tag{119}$$

$$S_{44} = d_4\gamma(\gamma-1) \tag{120}$$

Jacobian matrices P and R are defined by eqns. (26) and (28). The matrices $(-P + R_\xi)$ and $(-Q + S_\eta)$ required in the Beam-Warming algorithm (eqns. (39) and (40)) are :

$$-P + R_\xi = \frac{J}{\rho}\begin{pmatrix} 0 & 0 & 0 & 0 \\ -\left\{\left(\frac{b_1}{J}\right)_\xi u + \left(\frac{b_2}{J}\right)_\xi v\right\} & \left(\frac{b_1}{J}\right)_\xi & \left(\frac{b_2}{J}\right)_\xi & 0 \\ -\left\{\left(\frac{b_2}{J}\right)_\xi u + \left(\frac{b_3}{J}\right)_\xi v\right\} & \left(\frac{b_2}{J}\right)_\xi & \left(\frac{b_3}{J}\right)_\xi & 0 \\ P_{41} & P_{42} & P_{43} & P_{44} \end{pmatrix} \tag{121}$$

where

$$P_{41} = -\left(\frac{b_1}{J}\right)_\xi u^2 - 2\left(\frac{b_2}{J}\right)_\xi uv - \left(\frac{b_3}{J}\right)_\xi v^2 + \left(\frac{b_4}{J}\right)_\xi \gamma(\gamma-1)(u^2+v^2-e) \tag{122}$$

$$P_{42} = \left(\frac{b_1}{J}\right)_\xi u + \left(\frac{b_2}{J}\right)_\xi v - \left(\frac{b_4}{J}\right)_\xi \gamma(\gamma-1)u \tag{123}$$

$$P_{43} = \left(\frac{b_2}{J}\right)_\xi u + \left(\frac{b_3}{J}\right)_\xi v - \left(\frac{b_4}{J}\right)_\xi \gamma(\gamma-1)v \tag{124}$$

$$P_{44} = \left(\frac{b_4}{J}\right)_\xi \gamma(\gamma-1) \tag{125}$$

coefficients b_i (i=1,....4) are given in eqn. (8).

$$-Q + S_\eta = \frac{J}{\rho}\begin{pmatrix} 0 & 0 & 0 & 0 \\ -\left\{\left(\frac{d_1}{J}\right)_\eta u + \left(\frac{d_2}{J}\right)_\eta v\right\} & \left(\frac{d_1}{J}\right)_\eta & \left(\frac{d_2}{J}\right)_\eta & 0 \\ -\left\{\left(\frac{d_2}{J}\right)_\eta u + \left(\frac{d_3}{J}\right)_\eta v\right\} & \left(\frac{d_2}{J}\right)_\eta & \left(\frac{d_3}{J}\right)_\eta & 0 \\ Q_{41} & Q_{42} & Q_{43} & Q_{44} \end{pmatrix} \tag{126}$$

where

$$Q_{41} = -\left(\frac{d_1}{J}\right)_\eta u^2 - 2\left(\frac{d_2}{J}\right)_\eta uv - \left(\frac{d_3}{J}\right)_\eta v^2 + \left(\frac{d_4}{J}\right)_\eta \gamma(\gamma-1)(u^2+v^2-e) \tag{127}$$

$$Q_{42} = \left(\frac{d_1}{J}\right)_\eta u + \left(\frac{d_2}{J}\right)_\eta v - \left(\frac{d_4}{J}\right)_\eta \gamma(\gamma-1)u \tag{128}$$

$$Q_{43} = \left(\frac{d_2}{J}\right)_\eta u + \left(\frac{d_3}{J}\right)_\eta v - \left(\frac{d_4}{J}\right)_\eta \gamma(\gamma-1)v \tag{129}$$

$$Q_{44} = \left(\frac{d_4}{J}\right)_\eta \gamma(\gamma-1) \tag{130}$$

coefficients d_i (i=1,....4) are given in eq. (10).

B Geometric Conservation Law

Geometric Conservation Law is based on the basic principle that a uniform steady flow in a computational domain should remain uniform if there are no external disturbances and even if the computational grid moves with time.

The unsteady, compressible, two-dimensional Navier-Stokes equations in strong conservation form has been presented in eqn. 1. The corresponding equations in transformed coordinates (ξ, η) can be written as :

$$\frac{\partial q}{\partial t} + \frac{\partial \mathcal{F}}{\partial \xi} + \frac{\partial \mathcal{G}}{\partial \eta} = \frac{\partial \mathcal{R}}{\partial \xi} + \frac{\partial \mathcal{S}}{\partial \eta} \tag{131}$$

where

$$q = \frac{U}{J} \tag{132}$$

$$\mathcal{F} = \frac{1}{J}\left(\xi_t U + \xi_x \widehat{F} + \xi_y \widehat{G}\right) \tag{133}$$

$$\mathcal{G} = \frac{1}{J}\left(\eta_t U + \eta_x \widehat{F} + \eta_y \widehat{G}\right) \tag{134}$$

$$\mathcal{R} = \frac{1}{J}\left(\xi_x \widehat{R} + \xi_y \widehat{S}\right) \tag{135}$$

$$\mathcal{S} = \frac{1}{J}\left(\eta_x \widehat{R} + \eta_y \widehat{S}\right) \tag{136}$$

and

$$\xi_x = y_\eta J; \quad \xi_y = -x_\eta J; \quad \xi_t = (-x_t y_\eta + y_t x_\eta) J$$

$$\eta_x = -y_\xi J; \quad \eta_y = x_\xi J; \quad \eta_t = (x_t y_\xi - y_t x_\xi) J$$

Beam-Warming algorithm is applied to eqn. 131 with trapezoidal time differencing to give :

$$\Delta q^n = \frac{\Delta t}{2}\left[\frac{\partial}{\partial \xi}(-\Delta \mathcal{F} + \Delta \mathcal{R}) + \frac{\partial}{\partial \eta}(-\Delta \mathcal{G} + \Delta \mathcal{S})\right]^n + \Delta t\left[\frac{\partial}{\partial \xi}(-\mathcal{F} + \mathcal{R}) + \frac{\partial}{\partial \eta}(-\mathcal{G} + \mathcal{S})\right]^n \tag{137}$$

where

$$\Delta q^n = q^{n+1} - q^n = \Delta\left(\frac{U}{J}\right)^n = \left(\frac{1}{J}\right)^{n+1} \Delta U^n + U^n \Delta\left(\frac{1}{J}\right)^n \tag{138}$$

Substituting eqn. 138 in eqn. 137 gives :

$$\frac{1}{J^n}\Delta U^n + \frac{\Delta t}{2}\left[\frac{\partial}{\partial\xi}(\Delta\mathcal{F} - \Delta\mathcal{R}) + \frac{\partial}{\partial\eta}(\Delta\mathcal{G} - \Delta\mathcal{S})\right]^n = -\Delta t\left[\frac{\partial}{\partial\xi}(\mathcal{F} - \mathcal{R}) + \frac{\partial}{\partial\eta}(\mathcal{G} - \mathcal{S})\right]^n - U^n\Delta\left(\frac{1}{J}\right)^n \tag{139}$$

Approximate factorization of eqn. 139 leads to :

$$\left[I + \frac{\Delta t}{2}\frac{\partial}{\partial\xi}(\mathcal{A}^n - \mathcal{C}^n)\right]\left[I + \frac{\Delta t}{2}\frac{\partial}{\partial\eta}(\mathcal{B}^n - \mathcal{D}^n)\right]\frac{\Delta U^n}{J^n} = -\left[U^n\Delta\left(\frac{1}{J}\right)^n + \Delta t\left\{\frac{\partial}{\partial\xi}(\mathcal{F} - \mathcal{R}) + \frac{\partial}{\partial\eta}(\mathcal{G} - \mathcal{S})\right\}^n\right] \tag{140}$$

where $\mathcal{A}$, $\mathcal{B}$, $\mathcal{C}$, and $\mathcal{D}$ are the Jacobian matrices defined by :

$$\mathcal{A} = \frac{\partial\mathcal{F}}{\partial q}; \quad \mathcal{B} = \frac{\partial\mathcal{G}}{\partial q}; \quad \mathcal{C} = \frac{\partial\mathcal{R}}{\partial q}; \quad \mathcal{D} = \frac{\partial\mathcal{S}}{\partial q} \tag{141}$$

If we consider uniform steady flow in the computational domain then the flow should remain unaltered after a time Δt. Also

$$u^n_{i,j} = u_\infty; \quad v^n_{i,j} = v_\infty; \quad p^n_{i,j} = p_\infty; \quad \rho^n_{i,j} = \rho_\infty; \quad U = Constant$$
$$\Delta U^n = 0; \quad \widehat{F} = Constant; \quad \widehat{G} = Constant; \quad \widehat{R} = [0]; \quad \widehat{S} = [0] \tag{142}$$

Substituting eqn. 142 and eqns. 133 to 136 in eqn. 140 leads to :

$$-\Delta t\left[\frac{\partial}{\partial\xi}\left(\frac{1}{J}\left\{\xi_t U + \xi_x\widehat{F} + \xi_y\widehat{G}\right\}\right) + \frac{\partial}{\partial\eta}\left(\frac{1}{J}\left\{\eta_t U + \eta_x\widehat{F} + \eta_y\widehat{G}\right\}\right)\right]^n - U^n\Delta\left(\frac{1}{J}\right)^n = 0 \tag{143}$$

$$or, \quad -\Delta t\left[\frac{\partial}{\partial\xi}\left(\frac{\xi_t}{J}U + y_\eta\widehat{F} - x_\eta\widehat{G}\right) + \frac{\partial}{\partial\eta}\left(\frac{\eta_t}{J}U - y_\xi\widehat{F} + x_\xi\widehat{G}\right)\right]^n - U^n\Delta\left(\frac{1}{J}\right)^n = 0 \tag{144}$$

$$or, \quad -\left[\Delta\left(\frac{1}{J}\right) + \Delta t\left\{\frac{\partial}{\partial\xi}\left(\frac{\xi_t}{J}\right) + \frac{\partial}{\partial\eta}\left(\frac{\eta_t}{J}\right)\right\}\right]^n U^n - \Delta t\left[\frac{\partial y_\eta}{\partial\xi} - \frac{\partial y_\xi}{\partial\eta}\right]\widehat{F} - \Delta t\left[-\frac{\partial x_\eta}{\partial\xi} + \frac{\partial x_\xi}{\partial\eta}\right]\widehat{G} = 0 \tag{145}$$

The metrics x_ξ, x_η, y_ξ, and y_η are calculated numerically using finite-difference formulas. Figure 80 shows 9 nodes of a part of the computational transformed grid. If central finite-differences are used to compute the metrics at point 'C' of the grid, and $\Delta\xi$ and $\Delta\eta$ are

assumed to be 1.0, then :

$$\frac{\partial y_\eta}{\partial \xi} - \frac{\partial y_\xi}{\partial \eta} = \frac{1}{2}\frac{\partial}{\partial \xi}(y_2 - y_7) - \frac{1}{2}\frac{\partial}{\partial \eta}(y_5 - y_4) = \left(\frac{1}{2}\right)^2 (y_3 - y_1 - y_8 + y_6) - \left(\frac{1}{2}\right)^2 (y_3 - y_8 - y_1 + y_6) = 0 \quad (146)$$

$$\frac{\partial x_\xi}{\partial \eta} - \frac{\partial x_\eta}{\partial \xi} = \frac{1}{2}\frac{\partial}{\partial \eta}(x_5 - x_4) - \frac{1}{2}\frac{\partial}{\partial \xi}(x_2 - x_7) = \left(\frac{1}{2}\right)^2 (x_3 - x_8 - x_1 + x_6) - \left(\frac{1}{2}\right)^2 (x_3 - x_1 - x_8 + x_6) = 0 \quad (147)$$

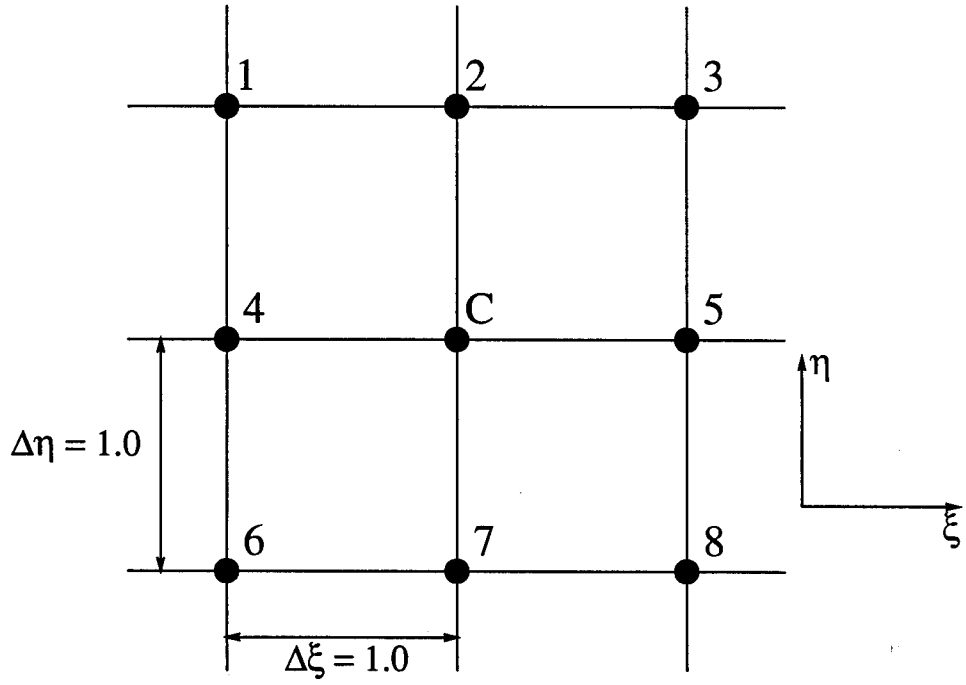

Figure 80: Part of the transformed (ξ, η) grid.

Substitution of eqns. (146) and (147) in eqn. (145) gives :

$$\left[\Delta\left(\frac{1}{J}\right) + \Delta t\left\{\frac{\partial}{\partial \xi}\left(\frac{\xi_t}{J}\right) + \frac{\partial}{\partial \eta}\left(\frac{\eta_t}{J}\right)\right\}\right]^n U^n = 0 \quad (148)$$

$$or, \quad \Delta\left(\frac{1}{J}\right)^n = -\Delta t\left\{\frac{\partial}{\partial \xi}\left(\frac{\xi_t}{J}\right) + \frac{\partial}{\partial \eta}\left(\frac{\eta_t}{J}\right)\right\}^n \quad (149)$$

$$or, \quad \Delta\left(\frac{1}{J}\right)^n = -\Delta t\left\{\frac{\partial}{\partial \xi}\left(-x_t y_\eta + y_t x_\eta\right) + \frac{\partial}{\partial \eta}\left(x_t y_\xi - y_t x_\xi\right)\right\}^n \quad (150)$$

For a stationary grid $\Delta(1/J)$ is equal to 0. *Geometric Conservation Law* states that for a grid moving with time, the term $-U^n\Delta(1/J)^n$ (given by eqn. (150)) is non-zero and has to be appended to the right hand side of the Beam-Warming algorithm.

C Method of Characteristics

The Method of Characteristics is based on the Euler equations. Figure 81 shows the outward moving perturbation wave generated by a point source after a time Δt. There is a uniform flow of velocity U_∞ coming into the domain. The perturbation wave moves in an approximately elliptical pattern. If the outer boundary is of the shape of the perturbation wave, the solution can be considered to be one-dimensional near the outer boundary. A C-grid matches with the wave shape to a certain degree, when the outer boundary is sufficiently far away from the airfoil. Therefore, a one-dimensional Method of Characteristics can be used at the outer boundary of the C-grid. In the Method of Characteristics, the Riemann variables corresponding to the characteristics moving out of the domain is interpolated from the inside of the domain and all the Riemann variables corresponding to the characteristics moving inside the domain are set as boundary conditions at the computational outer boundary.

A local coordinate system $(\overline{x}, \overline{y})$ is constructed orthogonal to the outer boundary with $\overline{x}$ normal to and directed outward from the boundary. The derivatives along the boundary $(\overline{y})$ are neglected (one-dimensional problem). Therefore, $\frac{\partial}{\partial \overline{y}}(\ ) = 0$.

The continuity equation can be written as :

$$\frac{D\rho}{Dt} + \rho \frac{\partial \overline{u}}{\partial \overline{x}} = 0 \tag{151}$$

where $\overline{u}$ is the velocity in $\overline{x}$-direction. Also $\rho = \rho(p, s)$, where p is the pressure and s is the entropy. Therefore,

$$d\rho = \left(\frac{\partial \rho}{\partial p}\right)_s dp + \left(\frac{\partial \rho}{\partial s}\right)_p ds \tag{152}$$

For locally isentropic flow, $ds = 0$. From eqns. (151) and (152) :

$$\frac{D\rho}{Dt} = \left(\frac{\partial \rho}{\partial p}\right)_s \frac{Dp}{Dt} = \frac{1}{a^2}\frac{Dp}{Dt} = -\rho \frac{\partial \overline{u}}{\partial \overline{x}} \tag{153}$$

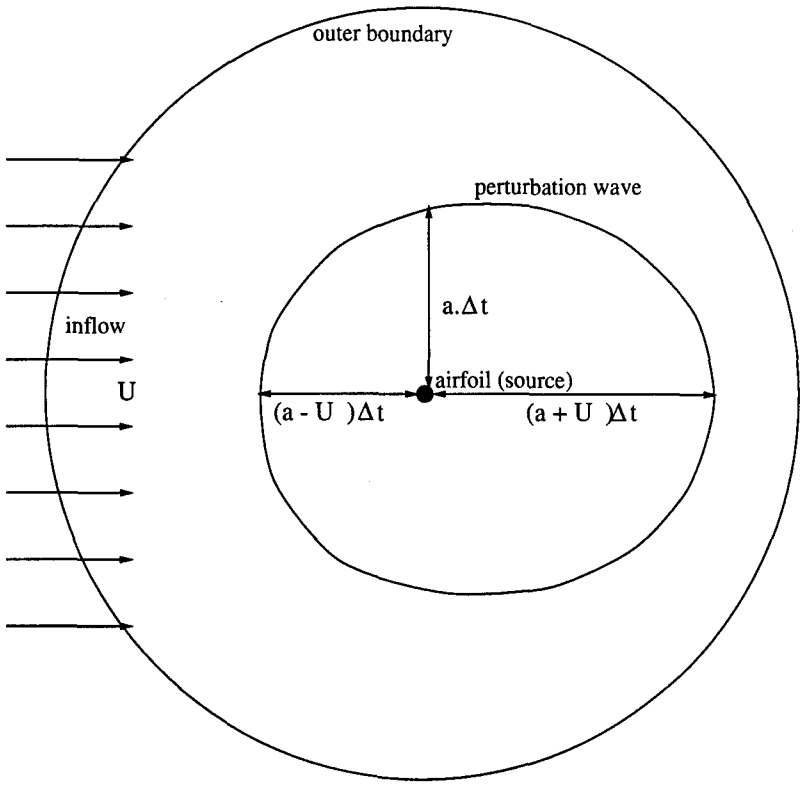

Figure 81: Perturbation wave around an airfoil.

$$or, \quad \frac{1}{\rho a}\left(\frac{\partial p}{\partial t} + \overline{u}\frac{\partial p}{\partial \overline{x}}\right) + a\frac{\partial \overline{u}}{\partial \overline{x}} = 0 \tag{154}$$

The momentum equation can be written as :

$$\frac{\partial \overline{u}}{\partial t} + \overline{u}\frac{\partial \overline{u}}{\partial \overline{x}} + \frac{1}{\rho}\frac{\partial p}{\partial \overline{x}} = 0 \tag{155}$$

Addition of eqns. (154) and (155) gives :

$$\left[\frac{\partial \overline{u}}{\partial t} + (\overline{u}+a)\frac{\partial \overline{u}}{\partial \overline{x}}\right] + \frac{1}{\rho a}\left[\frac{\partial p}{\partial t} + (\overline{u}+a)\frac{\partial p}{\partial \overline{x}}\right] = 0 \tag{156}$$

Subtraction of eqn. (154) from eqn. (155) gives :

$$\left[\frac{\partial \overline{u}}{\partial t} + (\overline{u}-a)\frac{\partial \overline{u}}{\partial \overline{x}}\right] - \frac{1}{\rho a}\left[\frac{\partial p}{\partial t} + (\overline{u}-a)\frac{\partial p}{\partial \overline{x}}\right] = 0 \tag{157}$$

Let, $\frac{d\overline{x}}{dt} = \overline{u} + a$. Therefore,

$$\frac{d\overline{u}}{dt} = \frac{\partial \overline{u}}{\partial t} + \frac{\partial \overline{u}}{\partial \overline{x}}\frac{d\overline{x}}{dt} = \frac{\partial \overline{u}}{\partial t} + (\overline{u}+a)\frac{\partial \overline{u}}{\partial \overline{x}} \tag{158}$$

$$\frac{dp}{dt} = \frac{\partial p}{\partial t} + \frac{\partial p}{\partial \overline{x}}\frac{d\overline{x}}{dt} = \frac{\partial p}{\partial t} + (\overline{u}+a)\frac{\partial p}{\partial \overline{x}} \tag{159}$$

Substitution of eqns. (158) and (159) in eqn. (156) gives :

$$d\overline{u} + \frac{dp}{\rho a} = 0 \tag{160}$$

For a perfect gas

$$a^2 = \frac{\gamma p}{\rho} \tag{161}$$

Also, for an isentropic process

$$p = C_3 T^{\frac{\gamma}{\gamma-1}} = C_4 a^{\frac{2\gamma}{\gamma-1}} \tag{162}$$

where C_3, and C_4 are constants.

$$dp = C_4 \left(\frac{2\gamma}{\gamma-1}\right) a^{\left\{\frac{2\gamma}{\gamma-1}-1\right\}} da \tag{163}$$

$$and, \quad \rho = C_4 \gamma a^{\left\{\frac{2\gamma}{\gamma-1}-2\right\}} \tag{164}$$

From eqns. (160), (163), and (164) :

$$\overline{u} + \int \frac{dp}{\rho a} = constant \tag{165}$$

$$or, \quad \overline{u} + \frac{2a}{\gamma-1} = constant \tag{166}$$

Therefore, the *first characteristic equation* is

$$\overline{u} + \frac{2a}{\gamma-1} = constant \quad along \quad \frac{d\overline{x}}{dt} = \overline{u} + a \tag{167}$$

Now, let $\frac{d\overline{x}}{dt} = \overline{u} - a$. This gives :

$$\frac{d\overline{u}}{dt} = \frac{\partial \overline{u}}{\partial t} + \frac{\partial \overline{u}}{\partial \overline{x}}\frac{d\overline{x}}{dt} = \frac{\partial \overline{u}}{\partial t} + (\overline{u} - a)\frac{\partial \overline{u}}{\partial \overline{x}} \tag{168}$$

$$\frac{dp}{dt} = \frac{\partial p}{\partial t} + \frac{\partial p}{\partial \overline{x}}\frac{d\overline{x}}{dt} = \frac{\partial p}{\partial t} + (\overline{u} - a)\frac{\partial p}{\partial \overline{x}} \tag{169}$$

Substitution of eqns. (168) and (169) in eqn. (157) gives :

$$d\overline{u} - \frac{dp}{\rho a} = 0 \tag{170}$$

$$\overline{u} - \int \frac{dp}{\rho a} = constant \tag{171}$$

$$\overline{u} - \frac{2a}{\gamma - 1} = constant \tag{172}$$

The *second characteristic equation* is

$$\overline{u} - \frac{2a}{\gamma - 1} = constant \quad along \quad \frac{d\overline{x}}{dt} = \overline{u} - a \tag{173}$$

The energy equation can be written as :

$$\frac{Ds}{Dt} = 0 = \frac{\partial s}{\partial t} + \overline{u}\frac{\partial s}{\partial \overline{x}} \tag{174}$$

Let $\frac{d\overline{x}}{dt} = \overline{u}$. Then

$$\frac{ds}{dt} = \frac{\partial s}{\partial t} + \frac{\partial s}{\partial \overline{x}}\frac{d\overline{x}}{dt} = \frac{\partial s}{\partial t} + \overline{u}\frac{\partial s}{\partial \overline{x}} \tag{175}$$

From eqns. (174) and (175)

$$\frac{ds}{dt} = 0 \tag{176}$$

The *third characteristic equation* is

$$s = constant \quad along \quad \frac{d\overline{x}}{dt} = \overline{u} \tag{177}$$

The equations are assumed to be one-dimensional at the boundary. Therefore, the velocity in the $\overline{y}$-direction ($\overline{v}$) can be assumed to be constant along the characteristic $\frac{d\overline{x}}{dt} = \overline{u}$.

The *fourth characteristic equation* is

$$\overline{v} = constant \quad along \quad \frac{d\overline{x}}{dt} = \overline{u} \tag{178}$$

D Jacobian Matrices for Unstructured Grid Algorithm

D.1 Inviscid Jacobian

Consider the terms in the inviscid Jacobian (90) involving the matrices

$$\begin{aligned} A_l &= \tfrac{1}{2} T^{-1} \frac{\partial H_l}{\partial Q_l} \Delta s \\ A_r &= \tfrac{1}{2} T^{-1} \frac{\partial H_r}{\partial Q_r} \Delta s \end{aligned}$$

The matrices A_l and A_r have an identical form, differing only in their evaluation using Q_l and Q_r, respectively. Define the matrix $A(Q)$ by

$$A = T^{-1} \frac{\partial H}{\partial Q} \Delta s$$

Note that A does *not* include the leading factor of $\frac{1}{2}$.

The components A_{ij} are

$$\begin{aligned} A_{11} &= -\bar{u}_s \Delta s \\ A_{12} &= \Delta y \\ A_{13} &= -\Delta x \\ A_{14} &= 0 \\ A_{21} &= \tfrac{1}{2} \left[(\gamma-3) u^2 + (\gamma-1) v^2 \right] \Delta y + uv \Delta x \\ A_{22} &= (3-\gamma) u \Delta y - v \Delta x - \bar{u}_s \Delta s \\ A_{23} &= -(\gamma-1) v \Delta y - u \Delta x \\ A_{24} &= (\gamma-1) \Delta y \\ A_{31} &= -uv \Delta y + \tfrac{1}{2} \left[(3-\gamma) v^2 - (\gamma-1) u^2 \right] \Delta x \\ A_{32} &= v \Delta y + (\gamma-1) u \Delta x \end{aligned}$$

$$
\begin{aligned}
A_{33} &= u\Delta y - (3-\gamma)\, v\Delta x - \bar{u}_s \Delta s \\
A_{34} &= -(\gamma-1)\, \Delta x \\
A_{41} &= \left[-\gamma u e + (\gamma-1)\left(u^3 + uv^2\right)\right] \Delta y + \left[\gamma v e - (\gamma-1)\left(u^2 v + v^3\right)\right] \Delta x \\
A_{42} &= \left[\gamma e - \frac{\gamma-1}{2}\left(3u^2 + v^2\right)\right] \Delta y + (\gamma-1)\, uv\Delta x \\
A_{43} &= -(\gamma-1)\, uv\Delta y - \left[\gamma e - \frac{\gamma-1}{2}\left(u^2 + 3v^2\right)\right] \Delta x \\
A_{44} &= \gamma\,(u\Delta y - v\Delta x) - \bar{u}_s \Delta s
\end{aligned}
$$

where

$$
\bar{u}_s = u_s \frac{\Delta y}{\Delta s} - v_s \frac{\Delta x}{\Delta s}
$$

Next, consider the terms in the inviscid Jacobian (90) involving the matrices

$$
\begin{aligned}
B_l &= \frac{\partial C}{\partial Q_l}\,(Q_l - Q_r) \\
B_r &= \frac{\partial C}{\partial Q_r}\,(Q_l - Q_r)
\end{aligned}
$$

where

$$
C = \tfrac{1}{2} T^{-1} \tilde{S} |\Lambda| \tilde{S}^{-1} T \Delta s
$$

Define the vector

$$
\tilde{Q} = (\tilde{\bar{u}}, \tilde{\bar{v}}, \tilde{a})^T
$$

Note that $\tilde{Q}$ has *three* components. Then

$$
\begin{aligned}
\frac{\partial C}{\partial Q_l} &= \frac{\partial C}{\partial \tilde{Q}} \frac{\partial \tilde{Q}}{\partial Q_l} \\
\frac{\partial C}{\partial Q_r} &= \frac{\partial C}{\partial \tilde{Q}} \frac{\partial \tilde{Q}}{\partial Q_r}
\end{aligned}
$$

where $\partial C / \partial \tilde{Q}$ is a *third* order tensor

$$
\frac{\partial C}{\partial \tilde{Q}} = \tfrac{1}{2} T^{-1} D T \Delta s
$$

and

$$
D = \frac{\partial \left(\tilde{S} |\tilde{\Lambda}| \tilde{S}^{-1}\right)}{\partial \tilde{Q}}
$$

The components D_{ijk} are defined as

$$D_{ijk} = \frac{\partial\left(\tilde{S}|\tilde{\Lambda}|\tilde{S}^{-1}|_{ij}\right)}{\partial\tilde{Q}_k}$$

where $|_{ij}$ indicates the component in the i^{th} row and j^{th} column of the matrix $\tilde{S}|\tilde{\Lambda}|\tilde{S}^{-1}$. The expressions are

$$\begin{aligned}
D_{111} &= \frac{\gamma-1}{2}\frac{\tilde{\bar{u}}}{\tilde{a}^2}\left[|\tilde{\lambda}_3|+|\tilde{\lambda}_4|-2|\tilde{\lambda}_2|\right]+\frac{\gamma-1}{2}\frac{\tilde{q}}{\tilde{a}^2}\left[\tilde{\Lambda}_3+\tilde{\Lambda}_4-2\tilde{\Lambda}_2\right]+\frac{1}{2\tilde{a}}\left[|\tilde{\lambda}_4|-|\tilde{\lambda}_3|\right] \\
&\quad +\frac{\tilde{\bar{u}}}{2\tilde{a}}\left[\tilde{\Lambda}_4-\tilde{\Lambda}_3\right]+\tilde{\Lambda}_2 \\
D_{112} &= \frac{\gamma-1}{2}\frac{\tilde{\bar{v}}}{\tilde{a}^2}\left[|\tilde{\lambda}_3|+|\tilde{\lambda}_4|-2|\tilde{\lambda}_2|\right] \\
D_{113} &= -(\gamma-1)\frac{\tilde{q}}{\tilde{a}^3}\left[|\tilde{\lambda}_3|+|\tilde{\lambda}_4|-2|\tilde{\lambda}_2|\right]+\frac{\gamma-1}{2}\frac{\tilde{q}}{\tilde{a}^2}\left[\tilde{\Lambda}_3-\tilde{\Lambda}_4\right]-\frac{1}{2}\frac{\tilde{\bar{u}}}{\tilde{a}^2}\left[|\tilde{\lambda}_4|-|\tilde{\lambda}_3|\right] \\
&\quad -\frac{1}{2}\frac{\tilde{\bar{u}}}{\tilde{a}}\left[\tilde{\Lambda}_4+\tilde{\Lambda}_3\right] \\
D_{121} &= \frac{\gamma-1}{2\tilde{a}^2}\left[2|\tilde{\lambda}_2|-|\tilde{\lambda}_3|-|\tilde{\lambda}_4|\right]+\frac{\gamma-1}{2}\frac{\tilde{\bar{u}}}{\tilde{a}^2}\left[2\tilde{\Lambda}_2-\tilde{\Lambda}_3-\tilde{\Lambda}_4\right]+\frac{1}{2\tilde{a}}\left[\tilde{\Lambda}_3-\tilde{\Lambda}_4\right] \\
D_{122} &= 0 \\
D_{123} &= -(\gamma-1)\frac{\tilde{\bar{u}}}{\tilde{a}^3}\left[2|\tilde{\lambda}_2|-|\tilde{\lambda}_3|-|\tilde{\lambda}_4|\right]+\frac{\gamma-1}{2}\frac{\tilde{\bar{u}}}{\tilde{a}^2}\left[\tilde{\Lambda}_4-\tilde{\Lambda}_3\right]-\frac{1}{2\tilde{a}^2}\left[|\tilde{\lambda}_3|-|\tilde{\lambda}_4|\right] \\
&\quad +\frac{1}{2\tilde{a}}\left[\tilde{\Lambda}_3+\tilde{\Lambda}_4\right] \\
D_{131} &= \frac{\gamma-1}{2}\frac{\tilde{\bar{v}}}{\tilde{a}^2}\left[2\tilde{\Lambda}_2-\tilde{\Lambda}_3-\tilde{\Lambda}_4\right] \\
D_{132} &= \frac{\gamma-1}{2\tilde{a}^2}\left[2|\tilde{\lambda}_2|-|\tilde{\lambda}_3|-|\tilde{\lambda}_4|\right\} \\
D_{133} &= -(\gamma-1)\frac{\tilde{\bar{v}}}{\tilde{a}^3}\left[2|\tilde{\lambda}_2|-|\tilde{\lambda}_3|-|\tilde{\lambda}_4|\right]+\frac{\gamma-1}{2}\frac{\tilde{\bar{v}}}{\tilde{a}^2}\left[\tilde{\Lambda}_4-\tilde{\Lambda}_3\right] \\
D_{141} &= \frac{\gamma-1}{2\tilde{a}^2}\left[\tilde{\Lambda}_3+\tilde{\Lambda}_4-2\tilde{\Lambda}_2\right] \\
D_{142} &= 0 \\
D_{143} &= -\frac{\gamma-1}{\tilde{a}^3}\left[|\tilde{\lambda}_3|+|\tilde{\lambda}_4|-2|\tilde{\lambda}_2|\right]+\frac{\gamma-1}{2\tilde{a}^2}\left[\tilde{\Lambda}_3-\tilde{\Lambda}_4\right] \\
D_{211} &= |\tilde{\lambda}_3|\frac{\gamma-1}{4\tilde{a}^2}\left[3\tilde{\bar{u}}^2+2\tilde{\bar{u}}\tilde{a}+\tilde{\bar{v}}^2\right]-|\tilde{\lambda}_3|\frac{1}{2\tilde{a}}\left[2\tilde{\bar{u}}+\tilde{a}\right]+|\tilde{\lambda}_4|\frac{\gamma-1}{4\tilde{a}^2}\left[3\tilde{\bar{u}}^2-2\tilde{\bar{u}}\tilde{a}+\tilde{\bar{v}}^2\right] \\
&\quad +|\tilde{\lambda}_4|\frac{1}{2\tilde{a}}\left[2\tilde{\bar{u}}-\tilde{a}\right]+|\tilde{\lambda}_2|\left[1-\frac{\gamma-1}{4\tilde{a}^2}\left(6\tilde{\bar{u}}^2+2\tilde{\bar{v}}^2\right)\right]+\tilde{\Lambda}_2\left[-\frac{(\gamma-1)}{\tilde{a}^2}\tilde{\bar{u}}\tilde{q}+\tilde{\bar{u}}\right] \\
&\quad +\tilde{\Lambda}_3\left[\frac{\gamma-1}{2\tilde{a}^2}\tilde{q}(\tilde{\bar{u}}+\tilde{a})-\frac{\tilde{\bar{u}}}{2\tilde{a}}(\tilde{\bar{u}}+\tilde{a})\right]+\tilde{\Lambda}_4\left[\frac{\gamma-1}{2\tilde{a}^2}\tilde{q}(\tilde{\bar{u}}-\tilde{a})+\frac{\tilde{\bar{u}}}{2\tilde{a}}(\tilde{\bar{u}}-\tilde{a})\right] \\
D_{212} &= \frac{\gamma-1}{2}\frac{\tilde{\bar{v}}}{\tilde{a}^2}\left[|\tilde{\lambda}_3|(\tilde{\bar{u}}+\tilde{a})+|\tilde{\lambda}_4|(\tilde{\bar{u}}-\tilde{a})-2|\tilde{\lambda}_2|\tilde{\bar{u}}\right]
\end{aligned}$$

$$
\begin{aligned}
D_{213} &= |\tilde{\lambda}_3|\left[\frac{\tilde{\bar{u}}^2}{2\tilde{a}^2}-\frac{(\gamma-1)}{2\tilde{a}^3}(\tilde{a}+2\tilde{\bar{u}})\,\tilde{q}\right]+|\tilde{\lambda}_4|\left[-\frac{\tilde{\bar{u}}^2}{2\tilde{a}^2}+\frac{(\gamma-1)}{2\tilde{a}^3}(\tilde{a}-2\tilde{\bar{u}})\,\tilde{q}\right]\\
&\quad+|\tilde{\lambda}_2|\left[\frac{(\gamma-1)}{\tilde{a}^3}\tilde{\bar{u}}(\tilde{\bar{u}}^2+\tilde{\bar{v}}^2)\right]+\tilde{\Lambda}_3(\tilde{\bar{u}}+\tilde{a})\left[-\frac{\tilde{\bar{u}}}{2\tilde{a}}+\frac{(\gamma-1)}{2\tilde{a}^2}\,\tilde{q}\right]\\
&\quad-\tilde{\Lambda}_4(\tilde{\bar{u}}-\tilde{a})\left[+\frac{\tilde{\bar{u}}}{2\tilde{a}}+\frac{(\gamma-1)}{2\tilde{a}^2}\,\tilde{q}\right]\\
D_{221} &= +|\tilde{\lambda}_2|\left[2(\gamma-1)\frac{\tilde{\bar{u}}}{\tilde{a}^2}\right]+|\tilde{\lambda}_3|\left[\frac{1}{2\tilde{a}}-\frac{(\gamma-1)}{2\tilde{a}^2}\,(2\tilde{\bar{u}}+\tilde{a})\right]-|\tilde{\lambda}_4|\left[\frac{1}{2\tilde{a}}+\frac{(\gamma-1)}{2\tilde{a}^2}\,(2\tilde{\bar{u}}-\tilde{a})\right]\\
&\quad+\tilde{\Lambda}_2\left[(\gamma-1)\frac{\tilde{\bar{u}}^2}{\tilde{a}^2}\right]+\tilde{\Lambda}_3(\tilde{\bar{u}}+\tilde{a})\left[\frac{1}{2\tilde{a}}-\frac{(\gamma-1)}{2}\frac{\tilde{\bar{u}}}{\tilde{a}^2}\right]-\tilde{\Lambda}_4(\tilde{\bar{u}}-\tilde{a})\left[\frac{1}{2\tilde{a}}+\frac{(\gamma-1)}{2}\frac{\tilde{\bar{u}}}{\tilde{a}^2}\right]\\
D_{222} &= 0\\
D_{223} &= -|\tilde{\lambda}_2|\left[2(\gamma-1)\frac{\tilde{\bar{u}}^2}{\tilde{a}^3}\right]+|\tilde{\lambda}_3|\left[(\gamma-1)\left(\frac{\tilde{\bar{u}}^2}{\tilde{a}^3}+\frac{\tilde{\bar{u}}}{2\tilde{a}^2}\right)-\frac{\tilde{\bar{u}}}{2\tilde{a}^2}\right]+\tilde{\Lambda}_3\frac{(\tilde{\bar{u}}+\tilde{a})}{2\tilde{a}}\left[1-(\gamma-1)\frac{\tilde{\bar{u}}}{\tilde{a}}\right]\\
&\quad+|\tilde{\lambda}_4|\left[(\gamma-1)\left(\frac{\tilde{\bar{u}}^2}{\tilde{a}^3}-\frac{\tilde{\bar{u}}}{2\tilde{a}^2}\right)+\frac{\tilde{\bar{u}}}{2\tilde{a}^2}\right]+\tilde{\Lambda}_4\frac{(\tilde{\bar{u}}-\tilde{a})}{2\tilde{a}}\left[1+(\gamma-1)\frac{\tilde{\bar{u}}}{\tilde{a}}\right]\\
D_{231} &= \frac{(\gamma-1)}{2}\frac{\tilde{\bar{v}}}{\tilde{a}^2}\left[2|\tilde{\lambda}_2|+2\tilde{\bar{u}}\tilde{\Lambda}_2-|\tilde{\lambda}_3|-(\tilde{\bar{u}}+\tilde{a})\tilde{\Lambda}_3-|\tilde{\lambda}_4|-(\tilde{\bar{u}}-\tilde{a})\tilde{\Lambda}_4\right]\\
D_{232} &= \frac{(\gamma-1)}{2\tilde{a}^2}\left[2\tilde{\bar{u}}|\tilde{\lambda}_2|-(\tilde{\bar{u}}+\tilde{a})|\tilde{\lambda}_3|-(\tilde{\bar{u}}-\tilde{a})|\tilde{\lambda}_4|\right]\\
D_{233} &= -2|\tilde{\lambda}_2|\left[(\gamma-1)\frac{\tilde{\bar{u}}\tilde{\bar{v}}}{\tilde{a}^3}\right]+|\tilde{\lambda}_3|\left[\frac{\gamma-1}{2}\frac{\tilde{\bar{v}}}{\tilde{a}^3}(2\tilde{\bar{u}}+\tilde{a})\right]+|\tilde{\lambda}_4|\left[\frac{\gamma-1}{2}\frac{\tilde{\bar{v}}}{\tilde{a}^3}(2\tilde{\bar{u}}-\tilde{a})\right]\\
&\quad-\tilde{\Lambda}_3\left[\frac{\gamma-1}{2}\frac{\tilde{\bar{v}}}{\tilde{a}^2}(\tilde{\bar{u}}+\tilde{a})\right]+\tilde{\Lambda}_4\left[\frac{\gamma-1}{2}\frac{\tilde{\bar{v}}}{\tilde{a}^2}(\tilde{\bar{u}}-\tilde{a})\right]\\
D_{241} &= \frac{\gamma-1}{2\tilde{a}^2}\left[|\tilde{\lambda}_3|+|\tilde{\lambda}_4|-2|\tilde{\lambda}_2|-2\tilde{\bar{u}}\tilde{\Lambda}_2(\tilde{\bar{u}}+\tilde{a})\tilde{\Lambda}_3+(\tilde{\bar{u}}-\tilde{a})\tilde{\Lambda}_4\right]\\
D_{242} &= 0\\
D_{243} &= -|\tilde{\lambda}_3|\left[\frac{\gamma-1}{2\tilde{a}^3}(2\tilde{\bar{u}}+\tilde{a})\right]+|\tilde{\lambda}_4|\left[\frac{\gamma-1}{2\tilde{a}^3}(-2\tilde{\bar{u}}+\tilde{a})\right]+|\tilde{\lambda}_2|\left[2(\gamma-1)\frac{\tilde{\bar{u}}}{\tilde{a}^3}\right]\\
&\quad+\tilde{\Lambda}_3\left[\frac{\gamma-1}{2\tilde{a}^2}(\tilde{\bar{u}}+\tilde{a})\right]-\tilde{\Lambda}_4\left[\frac{\gamma-1}{2\tilde{a}^2}(\tilde{\bar{u}}-\tilde{a})\right]\\
D_{311} &= \tilde{\bar{v}}(D_{111}-\tilde{\Lambda}_1)\\
D_{312} &= \frac{(\gamma-1)}{2\tilde{a}^2}\,\tilde{q}\left[|\tilde{\lambda}_3|+|\tilde{\lambda}_4|-2|\tilde{\lambda}_2|\right]+\frac{\tilde{\bar{u}}}{2\tilde{a}}\left[|\tilde{\lambda}_4|-|\tilde{\lambda}_3|\right]+\tilde{\bar{v}}D_{112}\\
D_{313} &= \tilde{\bar{v}}D_{113}\\
D_{321} &= \tilde{\bar{v}}D_{121}\\
D_{322} &= \frac{\gamma-1}{2}\frac{\tilde{\bar{u}}}{\tilde{a}^2}\left[2|\tilde{\lambda}_2|-|\tilde{\lambda}_3|-|\tilde{\lambda}_4|\right]+\frac{1}{2\tilde{a}}\left[|\tilde{\lambda}_3|-|\tilde{\lambda}_4|\right]+\tilde{\bar{v}}D_{122}\\
D_{323} &= \tilde{\bar{v}}D_{123}
\end{aligned}
$$

$$
\begin{aligned}
D_{331} &= \tilde{\Lambda}_1 + \tilde{\bar{v}} D_{131} \\
D_{332} &= \frac{\gamma-1}{2}\frac{\tilde{\bar{v}}}{\tilde{a}^2}\left[2|\tilde{\lambda}_2| - |\tilde{\lambda}_3| - |\tilde{\lambda}_4|\right] + \tilde{\bar{v}} D_{132} \\
D_{333} &= \tilde{\bar{v}} D_{133} \\
D_{341} &= \tilde{\bar{v}} D_{141} \\
D_{342} &= \frac{\gamma-1}{2\tilde{a}^2}\left[|\tilde{\lambda}_3| + |\tilde{\lambda}_4| - 2|\tilde{\lambda}_2|\right] + \tilde{\bar{v}} D_{142} \\
D_{343} &= \tilde{\bar{v}} D_{143} \\
D_{411} &= |\tilde{\lambda}_3|\left\{\frac{(\tilde{H} + \tilde{\bar{u}}\tilde{a})}{2\tilde{a}}\left[(\gamma-1)\frac{\tilde{\bar{u}}}{\tilde{a}} - 1\right] + \frac{(\tilde{\bar{u}} + \tilde{a})}{2\tilde{a}}\left[(\gamma-1)\frac{\tilde{q}}{\tilde{a}} - \tilde{\bar{u}}\right]\right\} \\
&\quad + |\tilde{\lambda}_4|\left\{\frac{(\tilde{H} - \tilde{\bar{u}}\tilde{a})}{2\tilde{a}}\left[(\gamma-1)\frac{\tilde{\bar{u}}}{\tilde{a}} + 1\right] + \frac{(\tilde{\bar{u}} - \tilde{a})}{2\tilde{a}}\left[(\gamma-1)\frac{\tilde{q}}{\tilde{a}} + \tilde{\bar{u}}\right]\right\} \\
&\quad + |\tilde{\lambda}_2|\tilde{\bar{u}}\left[1 - 2(\gamma-1)\frac{\tilde{q}}{\tilde{a}^2}\right] + \tilde{\Lambda}_3\frac{(\tilde{H} + \tilde{\bar{u}}\tilde{a})}{2\tilde{a}}\left[(\gamma-1)\frac{\tilde{q}}{\tilde{a}} - \tilde{\bar{u}}\right] \\
&\quad + \tilde{\Lambda}_4\frac{(\tilde{H} - \tilde{\bar{u}}\tilde{a})}{2\tilde{a}}\left[(\gamma-1)\frac{\tilde{q}}{\tilde{a}} + \tilde{\bar{u}}\right] + \tilde{\Lambda}_2\left[-(\gamma-1)\frac{\tilde{q}^2}{\tilde{a}^2} + \tilde{q} - \tilde{\bar{v}}^2\right] \\
D_{412} &= \frac{(\gamma-1)}{2}\frac{\tilde{\bar{v}}}{\tilde{a}^2}\left[(\tilde{H} + \tilde{\bar{u}}\tilde{a})|\tilde{\lambda}_3| - 2\tilde{q}|\tilde{\lambda}_2| + (\tilde{H} - \tilde{\bar{u}}\tilde{a})|\tilde{\lambda}_4|\right] \\
&\quad + \frac{(\gamma-1)}{2}\frac{\tilde{q}\tilde{\bar{v}}}{\tilde{a}^2}\left[|\tilde{\lambda}_3| + |\tilde{\lambda}_4| - 2|\tilde{\lambda}_2|\right] + \frac{\tilde{\bar{u}}\tilde{\bar{v}}}{2\tilde{a}}\left[|\tilde{\lambda}_4| - |\tilde{\lambda}_3|\right] - \tilde{\bar{v}}|\tilde{\lambda}_2| \\
D_{413} &= + |\tilde{\lambda}_3|\left\{\frac{(\tilde{H} + \tilde{\bar{u}}\tilde{a})}{\tilde{a}^2}\left[-(\gamma-1)\frac{\tilde{q}}{\tilde{a}} + \frac{\tilde{\bar{u}}}{2}\right] + \left(\frac{2\tilde{a}}{\gamma-1} + \tilde{\bar{u}}\right)\frac{1}{\tilde{a}}\left[\frac{(\gamma-1)}{2}\frac{\tilde{q}}{\tilde{a}} - \frac{\tilde{\bar{u}}}{2}\right]\right\} \\
&\quad + |\tilde{\lambda}_4|\left\{\frac{(\tilde{H} - \tilde{\bar{u}}\tilde{a})}{\tilde{a}^2}\left[-(\gamma-1)\frac{\tilde{q}}{\tilde{a}} - \frac{\tilde{\bar{u}}}{2}\right] + \left(\frac{2\tilde{a}}{\gamma-1} - \tilde{\bar{u}}\right)\frac{1}{\tilde{a}}\left[\frac{(\gamma-1)}{2}\frac{\tilde{q}}{\tilde{a}} + \frac{\tilde{\bar{u}}}{2}\right]\right\} \\
&\quad + \tilde{\Lambda}_3\left\{\frac{(\tilde{H} + \tilde{\bar{u}}\tilde{a})}{\tilde{a}}\left[\frac{(\gamma-1)}{2}\frac{\tilde{q}}{\tilde{a}} - \frac{\tilde{\bar{u}}}{2}\right]\right\} - \tilde{\Lambda}_4\left\{\frac{(\tilde{H} - \tilde{\bar{u}}\tilde{a})}{\tilde{a}}\left[\frac{(\gamma-1)}{2}\frac{\tilde{q}}{\tilde{a}} + \frac{\tilde{\bar{u}}}{2}\right]\right\} \\
&\quad + |\tilde{\lambda}_2|\left\{2(\gamma-1)\frac{\tilde{q}^2}{\tilde{a}^3}\right\} \\
D_{421} &= + |\tilde{\lambda}_3|\left\{-\frac{(\gamma-1)}{2}\frac{(\tilde{H} + \tilde{\bar{u}}\tilde{a})}{\tilde{a}^2} + \frac{(\tilde{\bar{u}} + \tilde{a})}{2\tilde{a}}\left[1 - (\gamma-1)\frac{\tilde{\bar{u}}}{\tilde{a}}\right]\right\} \\
&\quad - |\tilde{\lambda}_4|\left\{\frac{(\gamma-1)}{2}\frac{(\tilde{H} - \tilde{\bar{u}}\tilde{a})}{\tilde{a}^2} + \frac{(\tilde{\bar{u}} - \tilde{a})}{2\tilde{a}}\left[1 + (\gamma-1)\frac{\tilde{\bar{u}}}{\tilde{a}}\right]\right\} + |\tilde{\lambda}_2|\frac{(\gamma-1)}{\tilde{a}^2}\left(\tilde{q} + \tilde{\bar{u}}^2\right) \\
&\quad + \tilde{\Lambda}_3\frac{(\tilde{H} + \tilde{\bar{u}}\tilde{a})}{2\tilde{a}}\left[1 - (\gamma-1)\frac{\tilde{\bar{u}}}{\tilde{a}}\right] - \tilde{\Lambda}_4\frac{(\tilde{H} - \tilde{\bar{u}}\tilde{a})}{2\tilde{a}}\left[1 + (\gamma-1)\frac{\tilde{\bar{u}}}{\tilde{a}}\right] + \tilde{\Lambda}_2(\gamma-1)\frac{\tilde{\bar{u}}\tilde{q}}{\tilde{a}^2} \\
D_{422} &= \frac{\gamma-1}{2}\frac{\tilde{\bar{u}}\tilde{\bar{v}}}{\tilde{a}^2}\left[2|\tilde{\lambda}_2| - |\tilde{\lambda}_3| - |\tilde{\lambda}_4|\right] + \frac{\tilde{\bar{v}}}{2\tilde{a}}\left[|\tilde{\lambda}_3| - |\tilde{\lambda}_4|\right] \\
D_{423} &= + |\tilde{\lambda}_3|\left\{\frac{(\tilde{H} + \tilde{\bar{u}}\tilde{a})}{\tilde{a}^2}\left[(\gamma-1)\frac{\tilde{\bar{u}}}{\tilde{a}} - \frac{1}{2}\right] + \left[\frac{2\tilde{a}}{\gamma-1} + \tilde{\bar{u}}\right]\frac{1}{2\tilde{a}}\left[1 - (\gamma-1)\frac{\tilde{\bar{u}}}{\tilde{a}}\right]\right\}
\end{aligned}
$$

$$
\begin{aligned}
&+|\tilde{\lambda}_4|\left\{\frac{(\tilde{H}-\tilde{\bar{u}}\tilde{a})}{\tilde{a}^2}\left[(\gamma-1)\frac{\tilde{\bar{u}}}{\tilde{a}}+\frac{1}{2}\right]-\left[\frac{2\tilde{a}}{\gamma-1}-\tilde{\bar{u}}\right]\frac{1}{2\tilde{a}}\left[1+(\gamma-1)\frac{\tilde{\bar{u}}}{\tilde{a}}\right]\right\}\\
&+\tilde{\Lambda}_3\frac{(\tilde{H}+\tilde{\bar{u}}\tilde{a})}{2\tilde{a}}\left[1-(\gamma-1)\frac{\tilde{\bar{u}}}{\tilde{a}}\right]+\tilde{\Lambda}_4\frac{(\tilde{H}-\tilde{\bar{u}}\tilde{a})}{2\tilde{a}}\left[1+(\gamma-1)\frac{\tilde{\bar{u}}}{\tilde{a}}\right]\\
&-|\tilde{\lambda}_2|\left[2(\gamma-1)\frac{\tilde{\bar{u}}\tilde{q}}{\tilde{a}^3}\right]
\end{aligned}
$$

$$
\begin{aligned}
D_{431} &= \frac{(\gamma-1)}{2}\frac{\tilde{\bar{v}}}{\tilde{a}^2}\left[2\tilde{\bar{u}}|\tilde{\lambda}_2|+2\tilde{q}\tilde{\Lambda}_2-(\tilde{\bar{u}}+\tilde{a})|\tilde{\lambda}_3|-(\tilde{H}+\tilde{\bar{u}}\tilde{a})\tilde{\Lambda}_3-(\tilde{\bar{u}}-\tilde{a})|\tilde{\lambda}_4|-\right.\\
&\quad\left.(\tilde{H}-\tilde{\bar{u}}\tilde{a})\tilde{\Lambda}_4\right]+\tilde{\bar{v}}\tilde{\Lambda}_1\\
D_{432} &= -|\tilde{\lambda}_3|\frac{(\gamma-1)}{2\tilde{a}^2}\left[(\tilde{H}+\tilde{\bar{u}}\tilde{a})+\tilde{\bar{v}}^2\right]-|\tilde{\lambda}_4|\frac{(\gamma-1)}{2\tilde{a}^2}\left[(\tilde{H}-\tilde{\bar{u}}\tilde{a})+\tilde{\bar{v}}^2\right]\\
&\quad+|\tilde{\lambda}_2|\left[\frac{(\gamma-1)}{\tilde{a}^2}(\tilde{q}+\tilde{\bar{v}}^2)+1\right]\\
D_{433} &= +|\tilde{\lambda}_3|(\gamma-1)\frac{\tilde{\bar{v}}}{\tilde{a}^2}\left\{\frac{(\tilde{H}+\tilde{\bar{u}}\tilde{a})}{\tilde{a}}-\frac{1}{2}\left[\frac{2\tilde{a}}{\gamma-1}+\tilde{\bar{u}}\right]\right\}+|\tilde{\lambda}_4|(\gamma-1)\frac{\tilde{\bar{v}}}{\tilde{a}^2}\cdot\\
&\quad\left\{\frac{(\tilde{H}-\tilde{\bar{u}}\tilde{a})}{\tilde{a}}-\frac{1}{2}\left[\frac{2\tilde{a}}{\gamma-1}-\tilde{\bar{u}}\right]\right\}-2|\tilde{\lambda}_2|(\gamma-1)\frac{\tilde{\bar{v}}\tilde{q}}{\tilde{a}^3}\\
&\quad-\tilde{\Lambda}_3\left\{\frac{(\gamma-1)}{2}\frac{\tilde{\bar{v}}}{\tilde{a}^2}\left[\tilde{H}+\tilde{\bar{u}}\tilde{a}\right]\right\}+\tilde{\Lambda}_4\left\{\frac{(\gamma-1)}{2}\frac{\tilde{\bar{v}}}{\tilde{a}^2}\left[\tilde{H}-\tilde{\bar{u}}\tilde{a}\right]\right\}\\
D_{441} &= \frac{(\gamma-1)}{2\tilde{a}^2}\left[(\tilde{\bar{u}}+\tilde{a})|\tilde{\lambda}_3|+(\tilde{H}+\tilde{\bar{u}}\tilde{a})\tilde{\Lambda}_3+(\tilde{\bar{u}}-\tilde{a})|\tilde{\lambda}_4|+(\tilde{H}-\tilde{\bar{u}}\tilde{a})\tilde{\Lambda}_4-2\tilde{\bar{u}}|\tilde{\lambda}_2|-2\tilde{q}\tilde{\Lambda}_2\right]\\
D_{442} &= \frac{\gamma-1}{2}\frac{\tilde{\bar{v}}}{\tilde{a}^2}\left[|\tilde{\lambda}_3|+|\tilde{\lambda}_4|-2|\tilde{\lambda}_2|\right]\\
D_{443} &= +|\tilde{\lambda}_3|\frac{(\gamma-1)}{\tilde{a}^2}\left\{-\frac{(\tilde{H}+\tilde{\bar{u}}\tilde{a})}{\tilde{a}}+\frac{1}{2}\left[\frac{2\tilde{a}}{\gamma-1}+\tilde{\bar{u}}\right]\right\}+|\tilde{\lambda}_4|\frac{(\gamma-1)}{\tilde{a}^2}\cdot\\
&\quad\left\{-\frac{(\tilde{H}-\tilde{\bar{u}}\tilde{a})}{\tilde{a}}+\frac{1}{2}\left[\frac{2\tilde{a}}{\gamma-1}-\tilde{\bar{u}}\right]\right\}+|\tilde{\lambda}_2|(\gamma-1)\frac{2\tilde{q}}{\tilde{a}^3}+\tilde{\Lambda}_3\frac{(\gamma-1)}{2}\frac{(\tilde{H}+\tilde{\bar{u}}\tilde{a})}{\tilde{a}^2}\\
&\quad-\tilde{\Lambda}_4\frac{(\gamma-1)}{2}\frac{(\tilde{H}-\tilde{\bar{u}}\tilde{a})}{\tilde{a}^2}
\end{aligned}
$$

where

$$\tilde{q} = \tfrac{1}{2}\left(\tilde{\bar{u}}^2+\tilde{\bar{v}}^2\right)$$

The terms $\tilde{\Lambda}_j \equiv d \parallel \tilde{\lambda}_j \parallel / d\tilde{\lambda}_j$ are

$$\tilde{\Lambda}_j = \begin{cases} \text{sign}(\tilde{\lambda}_j) & \text{if } |\tilde{\lambda}_j| > \delta \\ \tilde{\lambda}_j/\delta & \text{if } |\tilde{\lambda}_j| \le \delta \end{cases}$$

The scalar quantities $\tilde{\Lambda}_j$, j = 1,2,3,4, should not be confused with the diagonal matrix $\tilde{\Lambda}$ in (75).

Define the arrays

$$E^l = \frac{\partial \tilde{Q}}{\partial Q_l} \text{ and } E^r = \frac{\partial \tilde{Q}}{\partial Q_r}$$

The matrices E^l and E^r have three rows and four columns.

$$\begin{aligned}
E^l_{11} &= -\frac{(\rho_r \bar{u}_r \sigma_r + \rho_l \bar{u}_l (1+\sigma_l))}{(\rho_l + \varrho)^2} \\
E^l_{12} &= \frac{1}{(\rho_l + \varrho)} \frac{\Delta y}{\Delta s} \\
E^l_{13} &= -\frac{1}{(\rho_l + \varrho)} \frac{\Delta x}{\Delta s} \\
E^l_{14} &= 0 \\
E^l_{21} &= -\frac{(\rho_r \bar{v}_r \sigma_r + \rho_l \bar{v}_l (1+\sigma_l))}{(\rho_l + \varrho)^2} \\
E^l_{22} &= \frac{1}{(\rho_l + \varrho)} \frac{\Delta x}{\Delta s} \\
E^l_{23} &= \frac{1}{(\rho_l + \varrho)} \frac{\Delta y}{\Delta s} \\
E^l_{24} &= 0 \\
E^l_{31} &= \frac{(\gamma-1)}{2\tilde{a}} \left\{ K^l_1 - \tilde{\bar{u}} E^l_{11} - \tilde{\bar{v}} E^l_{21} \right\} \\
E^l_{32} &= \frac{(\gamma-1)}{2\tilde{a}} \left\{ K^l_2 - \tilde{\bar{u}} E^l_{12} - \tilde{\bar{v}} E^l_{22} \right\} \\
E^l_{33} &= \frac{(\gamma-1)}{2\tilde{a}} \left\{ K^l_3 - \tilde{\bar{u}} E^l_{13} - \tilde{\bar{v}} E^l_{23} \right\} \\
E^l_{34} &= \frac{(\gamma-1)}{2\tilde{a}} \left\{ K^l_4 - \tilde{\bar{u}} E^l_{14} - \tilde{\bar{v}} E^l_{24} \right\} \\
E^r_{11} &= -\frac{(\rho_l \bar{u}_l \sigma_l + \rho_r \bar{u}_r (1+\sigma_r))}{(\rho_r + \varrho)^2} \\
E^r_{12} &= \frac{1}{(\rho_r + \varrho)} \frac{\Delta y}{\Delta s} \\
E^r_{13} &= -\frac{1}{(\rho_r + \varrho)} \frac{\Delta x}{\Delta s} \\
E^r_{14} &= 0 \\
E^r_{21} &= -\frac{(\rho_l \bar{v}_l \sigma_l + \rho_r \bar{v}_r (1+\sigma_r))}{(\rho_r + \varrho)^2} \\
E^r_{22} &= \frac{1}{(\rho_r + \varrho)} \frac{\Delta x}{\Delta s} \\
E^r_{23} &= \frac{1}{(\rho_r + \varrho)} \frac{\Delta y}{\Delta s} \\
E^r_{24} &= 0
\end{aligned}$$

$$
\begin{aligned}
E^r_{31} &= \frac{(\gamma-1)}{2\tilde{a}}\{K^r_1 - \tilde{\tilde{u}}E^r_{11} - \tilde{\tilde{v}}E^r_{21}\} \\
E^r_{32} &= \frac{(\gamma-1)}{2\tilde{a}}\{K^r_2 - \tilde{\tilde{u}}E^r_{12} - \tilde{\tilde{v}}E^r_{22}\} \\
E^r_{33} &= \frac{(\gamma-1)}{2\tilde{a}}\{K^r_3 - \tilde{\tilde{u}}E^r_{13} - \tilde{\tilde{v}}E^r_{23}\} \\
E^r_{34} &= \frac{(\gamma-1)}{2\tilde{a}}\{K^r_4 - \tilde{\tilde{u}}E^r_{14} - \tilde{\tilde{v}}E^r_{24}\}
\end{aligned}
$$

where

$$
\begin{aligned}
\sigma_l &= \frac{1}{2}\sqrt{\frac{\rho_r}{\rho_l}} \\
\sigma_r &= \frac{1}{2}\sqrt{\frac{\rho_l}{\rho_r}} \\
\varrho &= \sqrt{\rho_l \rho_r} \\
K^l_1 &= \frac{1}{\rho_l + \varrho}\left\{\frac{(\gamma-1)}{2}\left[u_l^2 + v_l^2\right] - \tfrac{1}{2}\left[\tilde{H} + H_l\right]\right\} \\
K^l_2 &= -\frac{(\gamma-1)u_l}{(\rho_l + \varrho)} \\
K^l_3 &= -\frac{(\gamma-1)v_l}{(\rho_l + \varrho)} \\
K^l_4 &= \frac{\gamma}{(\rho_l + \varrho)} \\
K^r_1 &= \frac{1}{\rho_r + \varrho}\left\{\frac{(\gamma-1)}{2}\left[u_r^2 + v_r^2\right] - \tfrac{1}{2}\left[\tilde{H} + H_r\right]\right\} \\
K^r_2 &= -\frac{(\gamma-1)u_r}{(\rho_r + \varrho)} \\
K^r_3 &= -\frac{(\gamma-1)v_r}{(\rho_r + \varrho)} \\
K^r_4 &= \frac{\gamma}{(\rho_r + \varrho)}
\end{aligned}
$$

The inviscid Jacobian is completed by specification of the matrices $\partial Q_l/\partial Q_j$ and $\partial Q_r/\partial Q_j$ in (90). These matrices follow directly from (77) and (78). Assuming linear reconstruction of the conservative variables (Fig. 9),

$$
\frac{\partial Q_l}{\partial Q_j} = \begin{cases} I & \text{if } j = i \\ \varsigma_a \Phi_Q & \text{if } j \text{ is point } a \\ \varsigma_b \Phi_Q & \text{if } j \text{ is point } b \\ \varsigma_c \Phi_Q & \text{if } j \text{ is point } c \end{cases}
$$

where I is the identity matrix and

$$\begin{aligned}
\varsigma_a &= \frac{1}{2V_{abc}}(\vec{n}_b + \vec{n}_c)\cdot\vec{r}ds \\
\varsigma_b &= \frac{1}{2V_{abc}}(\vec{n}_c + \vec{n}_a)\cdot\vec{r}ds \\
\varsigma_c &= \frac{1}{2V_{abc}}(\vec{n}_a + \vec{n}_b)\cdot\vec{r}ds
\end{aligned}$$

and

$$\Phi_Q = \mathrm{diag}(\Phi_\rho, \Phi_{\rho u}, \Phi_{\rho v}, \Phi_{\rho e})$$

The terms $\Phi_\rho, \Phi_{\rho u}, \Phi_{\rho v}$, and $\Phi_{\rho e}$ represent the limiter function Φ for the conservation of mass, $x-$ and $y-$ momentum, and energy, respectively.

A similar expression for $\partial Q_r/\partial Q_j$ may be obtained taking into account the location of the cells employed to form Q_r.

Special modifications are required for boundary cells, and are not presented herein.

D.2 Viscous Jacobian

The viscous Jacobian (92) may be expressed as

$$\frac{\partial N}{\partial Q_j} = \frac{\partial N}{\partial \hat{Q}_a}\frac{\partial \hat{Q}_a}{\partial Q_j} + \frac{\partial N}{\partial \hat{Q}_b}\frac{\partial \hat{Q}_b}{\partial Q_j} + \frac{\partial N}{\partial \hat{Q}_c}\frac{\partial \hat{Q}_c}{\partial Q_j} + \frac{\partial N}{\partial \hat{Q}_d}\frac{\partial \hat{Q}_d}{\partial Q_j}$$

where

$$\hat{Q} = (u, v, T)^T$$

and the subscripts a to d refer to the points shown in Fig. 3. Define

$$\hat{N}^a = \frac{\partial N}{\partial \hat{Q}_a}$$

and similarly for $\hat{N}^b, \hat{N}^c$, and $\hat{N}^d$. Then

$$\begin{aligned}
\hat{N}^a_{11} &= 0 \\
\hat{N}^a_{12} &= 0 \\
\hat{N}^a_{13} &= 0 \\
\hat{N}^a_{21} &= \Xi_\infty(-\tfrac{4}{3}\Delta y\Delta y_{41} - \Delta x\Delta x_{41}) \\
\hat{N}^a_{22} &= \Xi_\infty(-\tfrac{2}{3}\Delta y\Delta x_{41} + \Delta x\Delta y_{41})
\end{aligned}$$

$$
\begin{aligned}
\hat{N}^a_{23} &= 0 \\
\hat{N}^a_{31} &= \Xi_\infty(\Delta y \Delta x_{41} - \tfrac{2}{3}\Delta x \Delta y_{41}) \\
\hat{N}^a_{32} &= -\Xi_\infty(\Delta y \Delta y_{41} + \tfrac{4}{3}\Delta x \Delta x_{41}) \\
\hat{N}^a_{33} &= 0 \\
\hat{N}^a_{41} &= \tfrac{1}{2}(u_b + u_d)\hat{N}^a_{21} + \tfrac{1}{2}(v_b + v_d)\hat{N}^a_{31} \\
\hat{N}^a_{42} &= \tfrac{1}{2}(u_b + u_d)\hat{N}^a_{22} + \tfrac{1}{2}(v_b + v_d)\hat{N}^a_{32} \\
\hat{N}^a_{43} &= -\Xi_\infty \frac{1}{Pr(\gamma-1)}(\Delta y \Delta y_{41} + \Delta x \Delta x_{41}) \\
\hat{N}^b_{11} &= 0 \\
\hat{N}^b_{12} &= 0 \\
\hat{N}^b_{13} &= 0 \\
\hat{N}^b_{21} &= -\Xi_\infty(\tfrac{4}{3}\Delta y \Delta y_{12} + \Delta x \Delta x_{12}) \\
\hat{N}^b_{22} &= \Xi_\infty(-\tfrac{2}{3}\Delta y \Delta x_{12} + \Delta x \Delta y_{12}) \\
\hat{N}^b_{23} &= \frac{1}{2\mu}\frac{d\mu}{dT}N_2 \\
\hat{N}^b_{31} &= \Xi_\infty(\Delta y \Delta x_{12} - \tfrac{2}{3}\Delta x \Delta y_{12}) \\
\hat{N}^b_{32} &= -\Xi_\infty(\Delta y \Delta y_{12} + \tfrac{4}{3}\Delta x \Delta x_{12}) \\
\hat{N}^b_{33} &= \frac{1}{2\mu}\frac{d\mu}{dT}N_3 \\
\hat{N}^b_{41} &= \tfrac{1}{2}(u_b + u_d)\hat{N}^b_{21} + \tfrac{1}{2}(v_b + v_d)\hat{N}^b_{31} + \tfrac{1}{2}N_2 \\
\hat{N}^b_{42} &= \tfrac{1}{2}(u_b + u_d)\hat{N}^b_{22} + \tfrac{1}{2}(v_b + v_d)\hat{N}^b_{32} + \tfrac{1}{2}N_3 \\
\hat{N}^b_{43} &= \frac{1}{2\mu}\frac{d\mu}{dT}\left[N_4 - \tfrac{1}{2}N_2(u_b + u_d) - \tfrac{1}{2}N_3(v_b + v_d)\right] - \Xi_\infty \frac{1}{Pr(\gamma-1)}(\Delta y \Delta y_{12} + \Delta x \Delta x_{12}) \\
&\quad + \tfrac{1}{2}(u_b + u_d)\hat{N}^b_{23} + \tfrac{1}{2}(v_b + v_d)\hat{N}^b_{33} \\
\hat{N}^c_{11} &= 0 \\
\hat{N}^c_{12} &= 0 \\
\hat{N}^c_{13} &= 0 \\
\hat{N}^c_{21} &= -\Xi_\infty(\tfrac{4}{3}\Delta y \Delta y_{23} + \Delta x \Delta x_{23}) \\
\hat{N}^c_{22} &= \Xi_\infty(-\tfrac{2}{3}\Delta y \Delta x_{23} + \Delta x \Delta y_{23}) \\
\hat{N}^c_{23} &= 0 \\
\hat{N}^c_{31} &= \Xi_\infty(\Delta y \Delta x_{23} - \tfrac{2}{3}\Delta x \Delta y_{23})
\end{aligned}
$$

$$
\begin{aligned}
\hat{N}^c_{32} &= -\Xi_\infty(\Delta y\Delta y_{23} + \tfrac{4}{3}\Delta x\Delta x_{23}) \\
\hat{N}^c_{33} &= 0 \\
\hat{N}^c_{41} &= \tfrac{1}{2}(u_b+u_d)\hat{N}^c_{21} + \tfrac{1}{2}(v_b+v_d)\hat{N}^c_{31} \\
\hat{N}^c_{42} &= \tfrac{1}{2}(u_b+u_d)\hat{N}^c_{22} + \tfrac{1}{2}(v_b+v_d)\hat{N}^c_{32} \\
\hat{N}^c_{43} &= -\Xi_\infty \frac{1}{Pr(\gamma-1)}(\Delta y\Delta y_{23} + \Delta x\Delta x_{23}) + \tfrac{1}{2}(u_b+u_d)\hat{N}^c_{23} + \tfrac{1}{2}(v_b+v_d)\hat{N}^c_{33} \\
\hat{N}^d_{11} &= 0 \\
\hat{N}^d_{12} &= 0 \\
\hat{N}^d_{13} &= 0 \\
\hat{N}^d_{21} &= -\Xi_\infty(\tfrac{4}{3}\Delta y\Delta y_{34} + \Delta x\Delta x_{34}) \\
\hat{N}^d_{22} &= \Xi_\infty(-\tfrac{2}{3}\Delta y\Delta x_{34} + \Delta x\Delta y_{34}) \\
\hat{N}^d_{23} &= \frac{1}{2\mu}\frac{d\mu}{dT}N_2 \\
\hat{N}^d_{31} &= \Xi_\infty(\Delta y\Delta x_{34} - \tfrac{2}{3}\Delta x\Delta y_{34}) \\
\hat{N}^d_{32} &= -\Xi_\infty(\Delta y\Delta y_{34} + \tfrac{4}{3}\Delta x\Delta x_{34}) \\
\hat{N}^d_{33} &= \frac{1}{2\mu}\frac{d\mu}{dT}N_3 \\
\hat{N}^d_{41} &= \tfrac{1}{2}(u_b+u_d)\hat{N}^d_{21} + \tfrac{1}{2}(v_b+v_d)\hat{N}^d_{31} + \tfrac{1}{2}N_2 \\
\hat{N}^d_{42} &= \tfrac{1}{2}(u_b+u_d)\hat{N}^d_{22} + \tfrac{1}{2}(v_b+v_d)\hat{N}^d_{32} + \tfrac{1}{2}N_3 \\
\hat{N}^d_{43} &= \frac{1}{2\mu}\frac{d\mu}{dT}\left[N_4 - \tfrac{1}{2}N_2(u_b+u_d) - \tfrac{1}{2}N_3(v_b+v_d)\right] \\
&\quad -\Xi_\infty \frac{1}{Pr(\gamma-1)}(\Delta y\Delta y_{34} + \Delta x\Delta x_{34}) + \tfrac{1}{2}(u_b+u_d)\hat{N}^d_{23} + \tfrac{1}{2}(v_b+v_d)\hat{N}^d_{33}
\end{aligned}
$$

where

$$\Xi_\infty = \frac{M_\infty \mu}{2Re_\infty V_\mu}$$

and V_μ is the volume of the quadrilateral defined by point a, b, c, d in Fig. 3 and

$$\Delta x_1 = x_b - x_a$$

$$\Delta x_2 = x_c - x_b$$

$$\Delta x_3 = x_d - x_c$$

$$\Delta x_4 = x_a - x_d$$

$$\Delta y_1 = y_b - y_a$$

$$\Delta y_2 = y_c - y_b$$

$$\Delta y_3 = y_d - y_c$$

$$\Delta y_4 = y_a - y_d$$

while

$$\Delta x_{12} = \Delta x_1 + \Delta x_2$$

$$\Delta x_{23} = \Delta x_2 + \Delta x_3$$

$$\Delta x_{34} = \Delta x_3 + \Delta x_4$$

$$\Delta x_{41} = \Delta x_4 + \Delta x_1$$

and similarly for $\Delta y_{12}, \ldots$. Note that Δx and Δy refer to the $x-$ and $y-$ spacing on edge k.

The matrix $\partial \hat{Q}_a / \partial Q_j$ may be expanded as

$$\frac{\partial \hat{Q}_a}{\partial Q_j} = \frac{\partial \hat{Q}_a}{\partial Q_a} \frac{\partial Q_a}{\partial Q_j}$$

Define $\check{Q} = \partial \hat{Q}_\bullet / \partial Q_\bullet$ where the subscript $\bullet$ implies points a, b, c or d. Then,

$$\begin{aligned}
\check{Q}_{11} &= -\frac{u}{\rho} \\
\check{Q}_{12} &= \frac{1}{\rho} \\
\check{Q}_{13} &= 0 \\
\check{Q}_{14} &= 0 \\
\check{Q}_{21} &= -\frac{v}{\rho} \\
\check{Q}_{22} &= 0 \\
\check{Q}_{23} &= \frac{1}{\rho} \\
\check{Q}_{24} &= 0 \\
\check{Q}_{31} &= \frac{\gamma(\gamma-1)}{\rho^2}\left(-\rho e + \rho u^2 + \rho v^2\right) \\
\check{Q}_{32} &= -\gamma(\gamma-1)\frac{u}{\rho} \\
\check{Q}_{33} &= -\gamma(\gamma-1)\frac{v}{\rho} \\
\check{Q}_{34} &= \frac{\gamma(\gamma-1)}{\rho}
\end{aligned}$$

where the terms are evaluated at the respective point. The remaining matrix is

$$\frac{\partial Q_\bullet}{\partial Q_j} = \begin{cases} I & \text{if } \bullet \text{ and } j \text{ correspond} \\ & \text{to the same centroid} \\ \Omega_j I & \text{if } \bullet \text{ corresponds to a node} \end{cases}$$

where I is the identity matrix and

$$\Omega_j = \frac{w|_{\text{for cell j}}}{\sum_{cells} w_i}$$

Special modifications are required for boundary cells, and are not presented herein.

D.3 Roe Flux

For completeness, the elements of the Roe flux term $\tilde{S}|\tilde{\Lambda}|\tilde{S}^{-1}\Delta R$ in (75) are provided.

$$\begin{aligned}
\tilde{S}_{11} &= 0 \\
\tilde{S}_{12} &= 1 \\
\tilde{S}_{13} &= 1 \\
\tilde{S}_{14} &= 1 \\
\tilde{S}_{21} &= 0 \\
\tilde{S}_{22} &= \tilde{\tilde{u}} \\
\tilde{S}_{23} &= \tilde{\tilde{u}} + \tilde{a} \\
\tilde{S}_{24} &= \tilde{\tilde{u}} - \tilde{a} \\
\tilde{S}_{31} &= \tilde{\tilde{v}} \\
\tilde{S}_{32} &= \tilde{\tilde{v}} \\
\tilde{S}_{33} &= \tilde{\tilde{v}} \\
\tilde{S}_{34} &= \tilde{\tilde{v}} \\
\tilde{S}_{41} &= \tilde{\tilde{v}}^2 \\
\tilde{S}_{42} &= \tilde{q} \\
\tilde{S}_{43} &= \tilde{H} + \tilde{\tilde{u}}\tilde{a} \\
\tilde{S}_{44} &= \tilde{H} - \tilde{\tilde{u}}\tilde{a}
\end{aligned}$$

$$
\begin{aligned}
\tilde{S}_{11}^{-1} &= -1 \\
\tilde{S}_{12}^{-1} &= 0 \\
\tilde{S}_{13}^{-1} &= \tilde{\bar{v}}^{-1} \\
\tilde{S}_{14}^{-1} &= 0 \\
\tilde{S}_{21}^{-1} &= 1 - \frac{(\gamma-1)}{\tilde{a}^2}\tilde{q} \\
\tilde{S}_{22}^{-1} &= (\gamma-1)\frac{\tilde{\bar{u}}}{\tilde{a}^2} \\
\tilde{S}_{23}^{-1} &= (\gamma-1)\frac{\tilde{\bar{v}}}{\tilde{a}^2} \\
\tilde{S}_{24}^{-1} &= -\frac{\gamma-1}{\tilde{a}^2} \\
\tilde{S}_{31}^{-1} &= \frac{(\gamma-1)}{2\tilde{a}^2}\tilde{q} - \frac{\tilde{\bar{u}}}{2\tilde{a}} \\
\tilde{S}_{32}^{-1} &= -\frac{(\gamma-1)}{2}\frac{\tilde{\bar{u}}}{\tilde{a}^2} + \frac{1}{2\tilde{a}} \\
\tilde{S}_{33}^{-1} &= -\frac{(\gamma-1)}{2}\frac{\tilde{\bar{v}}}{\tilde{a}^2} \\
\tilde{S}_{34}^{-1} &= \frac{\gamma-1}{2\tilde{a}^2} \\
\tilde{S}_{41}^{-1} &= \frac{(\gamma-1)}{2\tilde{a}^2}\tilde{q} + \frac{\tilde{\bar{u}}}{2\tilde{a}} \\
\tilde{S}_{42}^{-1} &= -\frac{(\gamma-1)}{2}\frac{\tilde{\bar{u}}}{\tilde{a}^2} - \frac{1}{2\tilde{a}} \\
\tilde{S}_{43}^{-1} &= -\frac{(\gamma-1)}{2}\frac{\tilde{\bar{v}}}{\tilde{a}^2} \\
\tilde{S}_{44}^{-1} &= \frac{\gamma-1}{2\tilde{a}^2} \\
|\tilde{\Lambda}| &= \mathrm{diag}(|\tilde{\lambda}_1|, |\tilde{\lambda}_2|, |\tilde{\lambda}_3|, |\tilde{\lambda}_4|)
\end{aligned}
$$

The vector $\Delta R = R_l - R_r$ where

$$R = (\rho, \rho\bar{u}, \rho\bar{v}, \rho e)^T$$

E Stability Analysis

This appendix formulates the equations for a linear hydrodynamic stability analysis. The non-parallel Orr-Sommerfeld equation has been derived in a rotating frame of reference assuming incompressible flow and constant pitch-rate. The boundary conditions have also been derived for a constant rate pitching airfoil.

E.1 Governing Equation for Stability Analysis

The non-dimensional continuity and momentum equations for an incompressible flow in a reference frame attached to the airfoil pitching at a constant pitch rate Ω can be written as

$$\frac{\partial u}{\partial x} + \frac{\partial v}{\partial y} = 0 \tag{179}$$

$$\frac{\partial u}{\partial t} + u\frac{\partial u}{\partial x} + v\frac{\partial u}{\partial y} - 2\Omega v = -\frac{1}{\rho}\frac{\partial p}{\partial x} + \frac{1}{Re}\left(\frac{\partial^2 u}{\partial x^2} + \frac{\partial^2 u}{\partial y^2}\right) \tag{180}$$

$$\frac{\partial v}{\partial t} + u\frac{\partial v}{\partial x} + v\frac{\partial v}{\partial y} + 2\Omega u = -\frac{1}{\rho}\frac{\partial p}{\partial y} + \frac{1}{Re}\left(\frac{\partial^2 v}{\partial x^2} + \frac{\partial^2 v}{\partial y^2}\right) \tag{181}$$

A small disturbance is introduced into the base flow an the development of the flow field in time is monitored to determine whether the flow is stable or unstable. The velocities and pressure are written as follows

$$u = U + u' \tag{182}$$

$$v = V + v' \tag{183}$$

$$p = P + p' \tag{184}$$

These expressions are substituted into equations (179), (180), and (181) and then linearized to give the following equations

$$\frac{\partial u'}{\partial x} + \frac{\partial v'}{\partial y} = 0 \tag{185}$$

$$\frac{\partial u'}{\partial t} + u'\frac{\partial U}{\partial x} + v'\frac{\partial U}{\partial y} + U\frac{\partial u'}{\partial x} + V\frac{\partial u'}{\partial y} - 2\Omega v' = -\frac{1}{\rho}\frac{\partial p'}{\partial x} + \frac{1}{Re}\left(\frac{\partial^2 u'}{\partial x^2} + \frac{\partial^2 u'}{\partial y^2}\right) \quad (186)$$

$$\frac{\partial v'}{\partial t} + u'\frac{\partial V}{\partial x} + v'\frac{\partial V}{\partial y} + U\frac{\partial v'}{\partial x} + V\frac{\partial v'}{\partial y} + 2\Omega u' = -\frac{1}{\rho}\frac{\partial p'}{\partial y} + \frac{1}{Re}\left(\frac{\partial^2 v'}{\partial x^2} + \frac{\partial^2 v'}{\partial y^2}\right) \quad (187)$$

The velocity and pressure perturbations may be expressed as

$$u'(x,y,t) = \hat{u}(y)\exp\{i(kx - \omega t)\} \quad (188)$$

$$v'(x,y,t) = \hat{v}(y)\exp\{i(kx - \omega t)\} \quad (189)$$

$$p'(x,y,t) = \hat{p}(y)\exp\{i(kx - \omega t)\} \quad (190)$$

where k and ω are the complex wavenumber and frequency respectively, and $\hat{u}(y)$, $\hat{v}(y)$ and $\hat{p}(y)$ are the complex complex amplitude functions for the velocities and pressure. Substituting equations 188, 189, and 190 in equations 185, 186, and 187, we get

$$ik\hat{u} + D\hat{v} = 0 \quad (191)$$

$$-\hat{u}\omega i + \hat{u}\frac{\partial U}{\partial x} + \hat{v}\frac{\partial U}{\partial y} + U\hat{u}ki + V\hat{u} - 2\Omega\hat{v} = -\hat{p}ki + \frac{1}{Re}(-\hat{u}k^2 + D^2\hat{u}) \quad (192)$$

$$-\hat{v}\omega i + \hat{u}\frac{\partial V}{\partial x} + \hat{v}\frac{\partial V}{\partial y} + U\hat{v}ki + V\hat{v} + 2\Omega\hat{u} = -D\hat{p} + \frac{1}{Re}(-\hat{v}k^2 + D^2\hat{u}) \quad (193)$$

where "D" denotes differentiation with respect to y. The velocity perturbations can be expressed in terms of complex streamfunction perturbation

$$u' = \frac{\partial \psi'}{\partial y}; \qquad v' = -\frac{\partial \psi'}{\partial x} \quad (194)$$

where

$$\psi'(x,y,t) = \varphi(y)\exp\{i(kx - \omega t)\} \quad (195)$$

$\varphi(y)$ is the complex amplitude function. Utilization of equations 194 and 195 eliminates equation 191. From equations 192 and 193 we get

$$\left(-i\omega D + \frac{\partial U}{\partial x}D + iUkD + VD^2 - i\frac{\partial U}{\partial y}k + 2ik\Omega\right)\varphi = -ik\hat{p} + \frac{1}{Re}(-k^2D + D^3)\varphi \quad (196)$$

$$\left(-k\omega - ik\frac{\partial V}{\partial y} + k^2U - ikVD + \frac{\partial V}{\partial x}D + 2\Omega D\right)\varphi = -D\hat{p} + \frac{1}{Re}(ik^3 - ikD^2)\varphi \quad (197)$$

From equation 196

$$\hat{p} = \left(\frac{\omega D}{k} + i\frac{\partial U}{\partial x}\frac{D}{k} - UD + i\frac{VD^2}{k} + i\frac{kD}{Re} - i\frac{D^3}{kRe} + \frac{\partial U}{\partial y} - 2\Omega\right)\varphi \quad (198)$$

Substituting equation 198 in equation 197 gives

$$\left[\frac{i}{kRe}(D^2-k^2)^2+U(D^2-k^2)-\frac{\partial^2 U}{\partial y^2}-\frac{iV}{k}(D^2-k^2)D-\frac{\partial V}{\partial x}D\right.$$
$$\left.+ik\frac{\partial V}{\partial y}-\frac{i}{Re}\frac{\partial^2 U}{\partial y\partial x}D\right]\varphi-\frac{\omega}{k}(D^2-k^2)\varphi=0 \qquad (199)$$

The above equation is the Orr-Sommerfeld equation for a non-parallel flow. It is a fourth order complex differential equation which requires 2 boundary conditions at each of the two boundaries to solve the eigenvalue problem. The following subsection presents the appropriate boundary conditions for a constant rate pitching airfoil.

E.2 Boundary Condition for Stability Analysis

Suitable boundary conditions need to be specified at the two boundaries to solve the eigen value problem. The configuration of the airfoil pitching at a constant rate Ω about its quarter chord point is shown in figure 82. X-Y is the reference frame attached to the airfoil at the quarter chord point and aligned along the chord. X_1-Y_1 is the reference frame attached to the airfoil surface at (x_o, y_o) and aligned along the surface. Boundary conditions need to be determined at points A and B on the Y_1 axis. A is a point on the airfoil surface, while B is a point on the Y_1 axis at a large distance from the airfoil. The no-slip condition can be applied at the 'A' boundary, which is written as

$$u_1 = v_1 = 0 \;\; at \;\; Y_1 = 0 \qquad (200)$$

u_1 and v_1 are the velocities in the X_1-Y_1 frame of reference. Therefore the boundary condition applied at 'A' is

$$\varphi(y_1) = D\varphi(y_1) = 0 \;\; at \;\; Y_1 = 0 \qquad (201)$$

To determine the boundary condition at point 'B'[4] on the Y_1 axis, let us consider the velocities in the X_1-Y_1 frame at that point

$$u_1 = U_\infty \cos\theta - \Omega y \cos\theta + \Omega x \sin\theta \qquad (202)$$

$$v_1 = -U_\infty \sin\theta + \Omega y \sin\theta + \Omega x \cos\theta \qquad (203)$$

[4]B corresponds to a point where $Y_1 = \infty$

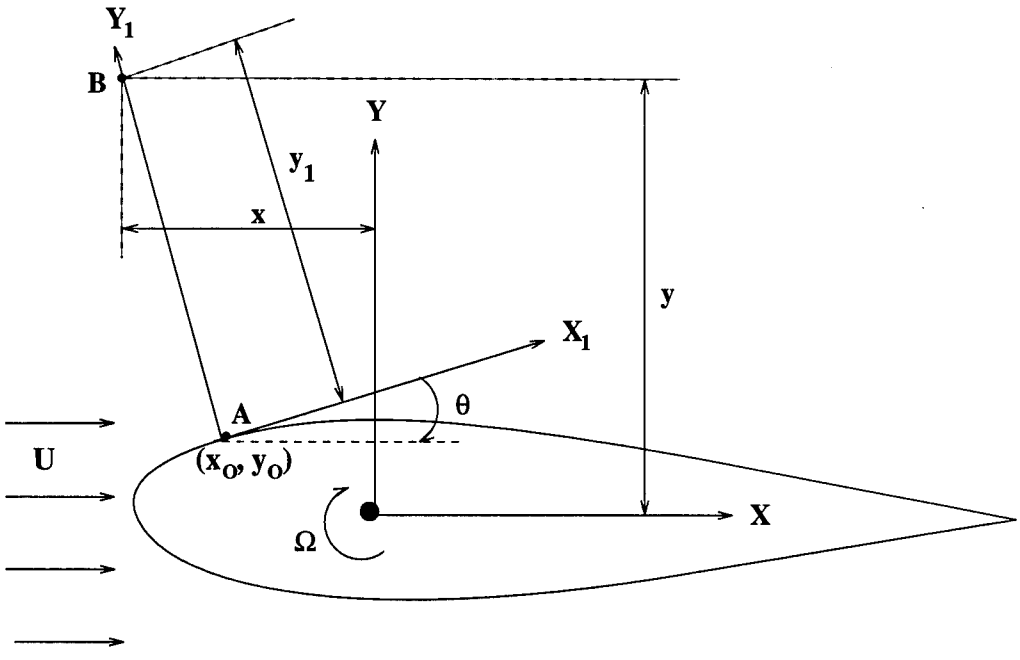

Figure 82: Configuration of the airfoil

But

$$y = y_o + y_1 \cos\theta \quad and \quad x = x_o - y_1 \sin\theta \tag{204}$$

Therefore equations 202 and 204 become

$$\begin{aligned} u_1 &= U_\infty \cos\theta - \Omega \cos\theta(y_o + y_1 \cos\theta) + \Omega \sin\theta(x_o - y_1 \sin\theta) \\ &= U_\infty \cos\theta - \Omega y_o \cos\theta + \Omega x_o \sin\theta - \Omega y_1 \end{aligned} \tag{205}$$

$$\begin{aligned} v_1 &= -U_\infty \sin\theta + \Omega \sin\theta(y_o + y_1 \cos\theta) + \Omega \cos\theta(x_o - y_1 \sin\theta) \\ &= -U_\infty \sin\theta + \Omega y_o \sin\theta + \Omega x_o \cos\theta \end{aligned} \tag{206}$$

Therefore

$$\frac{d^2 u_1}{dy_1^2} = \frac{dv_1}{dy_1} = 0 \quad or, \tag{207}$$

$$D\varphi(y_1) = D^3\varphi(y_1) = 0 \ \ at \ \ Y_1 = \infty \tag{208}$$

To summarize, the boundary conditions applied at the two boundaries are

$$\varphi(y_1) = D\varphi(y_1) = 0 \ \ at \ \ y_1 = 0 \quad and \tag{209}$$

$$D\varphi(y_1) = D^3\varphi(y_1) = 0 \ \ at \ \ y_1 = \infty \tag{210}$$

F Results using Implicit Unstructured Navier-Stokes Code

During the period of the no-cost extension (30 March 1995 - 30 March 1996), the research effort focused on the development and implementation of a preconditioner for the implicit unstructured Navier-Stokes algorithm, and the application of the algorithm to the simulation of flow past a pitching airfoil. Two cases were considered. The first case ($Re_c = 10^4$, $M_\infty = 0.2$, $\Omega_o^+ = 0.2$) is identical to Case 1 (see Sections 9.1 and 9.2), and thus provides a validation of the implicit unstructured Navier-Stokes algorithm. The second case ($Re_c = 2 \times 10^4$, $M_\infty = 0.2$, $\Omega_o^+ = 0.2$) represents a configuration not previously simulated, and provides new insight into the effects of Reynolds number on incipient separation for pitching airfoils. Specifically, the primary recirculation region appears at $\alpha = 14.5°$ for $Re_c = 2 \times 10^4$, compared to $\alpha = 14.99°$ for $Re_c = 10^4$. Furthermore, the primary recirculation region appears closer to the leading edge for $Re_c = 2 \times 10^4$. These effects of increasing Re_c are similar to those obtained at $M_\infty = 0.5$ for $Re_c = 10^4$ and 10^5 at $\Omega_o^+ = 0.2$ (*i.e.*, Cases 4 and 7 in Sections 9.5 and 9.8, respectively).

F.1 Numerical Algorithm

The implicit algorithm for the Navier-Stokes equations using an unstructured grid of triangles is described in Section 5. The method is second-order accurate in space, and either first-order or second-order accurate in time, depending on the choice of the temporal integration parameters. For these computations, the first-order time accurate Euler method is used with the time step Δt chosen to be the same as employed for the structured grid computation (see Section 9.1). Additionally, the Jacobian is updated every 20 time steps to reduce the CPU time. Thus, the overall algorithm is first-order accurate in time. Nonetheless, the results described herein indicate that a highly accurate solution is achieved, despite the use of the first-order time accuracy, due to the small value of the time step Δt.

Preconditioning was developed for, and implemented in, the BiCGSTAB algorithm (Section 5.7) using an incomplete LU factorization of the Jacobian matrix as the preconditioner. An LU factorization of the Jacobian is performed, but at each stage of the factorization the fill elements are ignored. Thus the incomplete LU factorization, to be used as the preconditioner, has the same sparsity structure as the original Jacobian matrix. This incomplete factorization is known as the ILU(0) factorization, since no fill-in is allowed. The preconditioning matrix in its LU form is then used to solve systems of equations as required in BiCGSTAB.

F.2 Details of Computations

An unstructured grid based on 13319 points used by Choudhuri [4], and having 26278 triangular cells was used. There were 180 points on the airfoil surfaces. The grid for $Re_c = 2 \times 10^4$ was derived from the grid for $Re_c = 10^4$ by moving the points $1/\sqrt{2}$ closer to the airfoil. Details of the computational grid can be found in Table 1 and Figs. 1 and 2. All distances are normalized by the airfoil chord c. The grid is attached to the airfoil.

Table 1: Details of Computational Grid

	Reynolds Number	
	10^4	2×10^4
Number of cells	26278	26278
Minimum Δs	3.17×10^{-3}	3.17×10^{-3}
Maximum Δs	2.65×10^{-2}	2.65×10^{-2}
Minimum Δn	1.06×10^{-3}	7.50×10^{-4}
Maximum Δn	1.26×10^{-3}	8.89×10^{-4}
N_{BL}	10	10
$A_{max} \div A_{min}$	3.73×10^5	5.94×10^5

Δs	Distance along airfoil
Δn	Distance normal to airfoil
N_{BL}	Number of points in boundary layer at mid-chord
A_{max}, A_{min}	Maximum, minimum area

Results were obtained for laminar flow over a pitching NACA 0012 airfoil at a Mach number of 0.2, pitching rate Ω_0^+ of 0.2 and Reynolds numbers of 10^4 and 2×10^4. The Jacobian was updated every 20 timesteps, with a timestep of 5×10^{-3}. Computations were performed on a CRAY C90 supercomputer. As described previously, the grid is attached to the airfoil, and therefore rotates with the airfoil. The velocity is computed

in the inertial frame; for analysis, the rotational motion of the airfoil is removed and the velocities computed in the airfoil frame. The streamlines are then plotted using the velocity components in the airfoil frame.

F.3 Results for $Re_c = 10^4$

The $Re_c = 10^4$ case is identical to Case 1 (see Sections 9.1 and 9.2), and provides a validation of the implicit unstructured grid algorithm for unsteady flows.

The computed lift, drag and moment coefficients, shown in Fig. 3 are in close agreement with the previous computations using both the explicit unstructured grid and implicit structured grid Navier-Stokes algorithms (see [4], Fig. 3).

In Figs. 4 to 11, 13 and 14, the instantaneous streamline plots are shown for both the explicit unstructured grid and implicit unstructured grid computations at 14.5°, 16.5°, 19.5°, 21.5° and 22.5°. The implicit and explicit algorithms are in excellent agreement. It was previously shown [4] that the explicit unstructured and implicit structured grid algorithms displayed excellent agreement for this case.

The algorithm required 14.6 hours of CPU time on the CRAY C90 to pitch the airfoil up to 22.5 degrees. The CPU time per timestep was about 350 seconds for a step with an update of the Jacobian and the preconditioner, and 7 seconds for a step without the update. Five iterations were required for convergence of BiCGSTAB at each timestep.

F.4 Results for $Re_c = 2 \times 10^4$

The $Re_c = 2 \times 10^4$ represents a new case. The flow development is similar to $Re_c = 10^4$, with a few major differences. As shown in Fig. 12, the lift and drag coefficient generally increase with the angle of attack; the moment coefficient is somewhat constant. Compared to $Re_c = 10^4$, the lift is slightly increased and drag is slightly decreased. The variation of lift and drag coefficients with angle of attack is not as monotonic at the higher Reynolds number. These differences are illustrated in Fig. 15.

The flow development is qualitatively similar to $Re_c = 10^4$: the appearance of the primary recirculating region at 14.5° (Fig. 16), its growth at 16.5° (Fig. 17), the appearance of a secondary recirculating region by 19.5° (Fig. 18), the formation of a tertiary recirculating region by 22.5° (Fig. 19), and the appearance of a fourth recirculating region by 23.5° (Fig. 20).

An examination of the angles at which the primary recirculating region forms shows that increasing Re_c accelerates the onset of flow separation, with the recirculation region appearing at a lower angle of attack for the higher Re_c. The recirculation region also appears to be closer to the leading edge. These trends are in agreement with published results [3] at $M_\infty = 0.5$ and $\Omega_o^+ = 0.2$. At this higher Mach number, an increase in Re_c from 10^4 to 10^5 accelerates the formation of the primary recirculation region from 18.8° to 14.9° and moves it forward.

The algorithm required 15.7 hours of CPU time on the CRAY C90 to pitch the airfoil up to 22.5 degrees. The CPU time per timestep was about 350 seconds for a step with an update of the Jacobian and the preconditioner, and 8 seconds for a step without the update. At each timestep, six BiCGSTAB iterations were required for convergence of the iterative solution of the matrix equations.

References

[1] O. Axelsson. *Iterative Solution Methods*, chapter 7. Cambridge University Press, 1994.

[2] R. Barrett, M. Berry, et al. *Templates for the Solution of Linear Systems: Building Blocks for Iterative Methods*, pages 40–41. Society for Industrial and Applied Mathematics (SIAM), 1994.

[3] P.G. Choudhuri and D. D. Knight. Effects of Compressibility, Pitch Rate, and Reynolds Number on Unsteady Incipient Leading-Edge Boundary Layer Separation over a Pitching Airfoil. *Journal of Fluid Mechanics*, 308:195–217, 1996.

[4] P.G. Choudhuri, D. D. Knight, and M.R. Visbal. Two-Dimensional Unsteady Leading Edge Separation on a Pitching Airfoil. *AIAA Journal*, 32(4):673–681, April 1994.

[5] F. Jacon and D. D. Knight. A Navier-Stokes Algorithm for Turbulent Flows Using an Unstructured Grid and Flux Difference Splitting. *AIAA 94-2292*, 1994.

[6] D. D. Knight. A Fully Implicit Navier-Stokes Algorithm using an Unstructured Grid and Flux Difference Splitting. *Applied Numerical Mathematics*, 16:101–128, 1994.

[7] H. A. van der Vorst. BI-CGSTAB: A Fast and Smoothly Converging Variant of BI-CG for the Solution of Non-symmetric Linear Systems. *SIAM Journal on Scientific and Statistical Computing*, 13(2):631–644, March 1992.

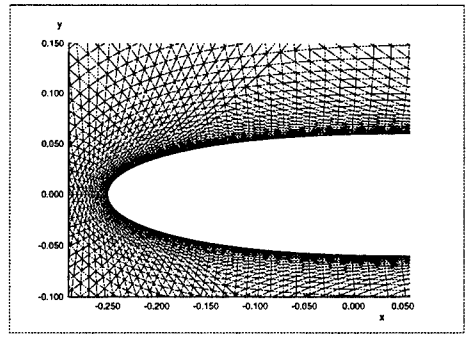

Figure 1: NACA0012 Airfoil Mesh $Re_c = 10^4$

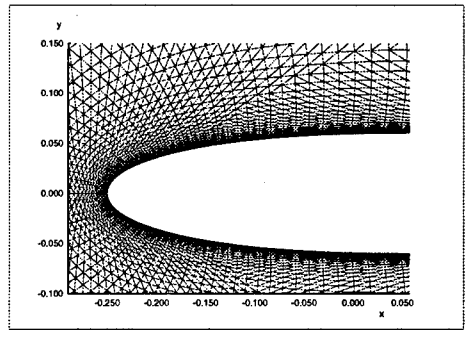

Figure 2: NACA0012 Airfoil Mesh $Re_c = 2 \times 10^4$

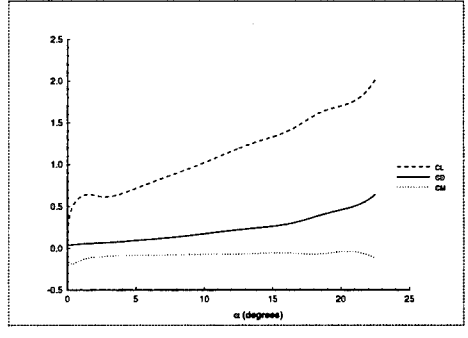

Figure 3: NACA0012 Pitching Airfoil $Re_c = 10^4$, Lift,Drag and Moment Coefficients

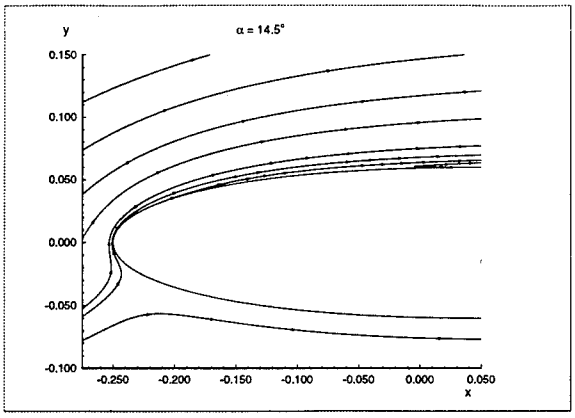

Figure 4: NACA0012 Pitching Airfoil, Implicit Computation, $Re_c = 10^4$, Streamlines, $\alpha = 14.5°$

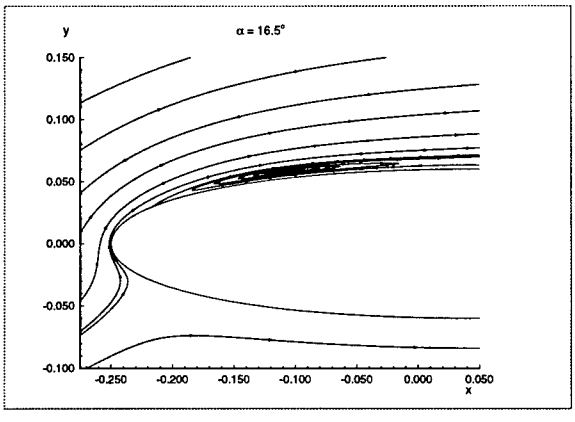

Figure 5: NACA0012 Pitching Airfoil, Implicit Computation, $Re_c = 10^4$, Streamlines, $\alpha = 16.5°$

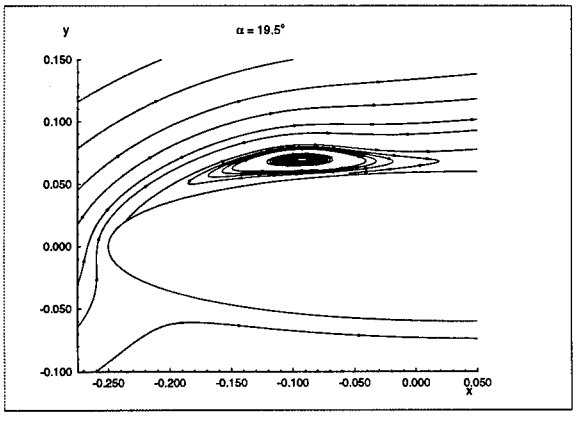

Figure 6: NACA0012 Pitching Airfoil, Implicit Computation, $Re_c = 10^4$, Streamlines, $\alpha = 19.5°$

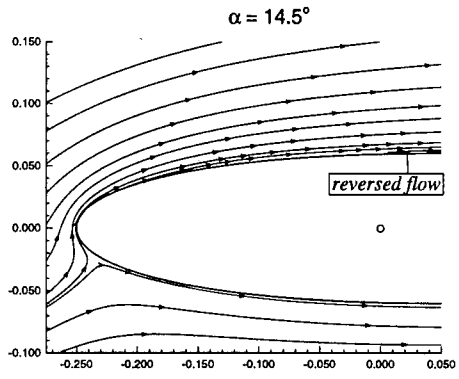

Figure 7: NACA0012 Pitching Airfoil, Explicit Computation, $Re_c = 10^4$, Streamlines, $\alpha = 14.5°$

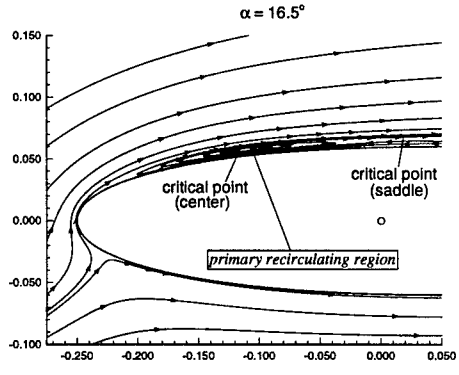

Figure 8: NACA0012 Pitching Airfoil, Explicit Computation, $Re_c = 10^4$, Streamlines, $\alpha = 16.5°$

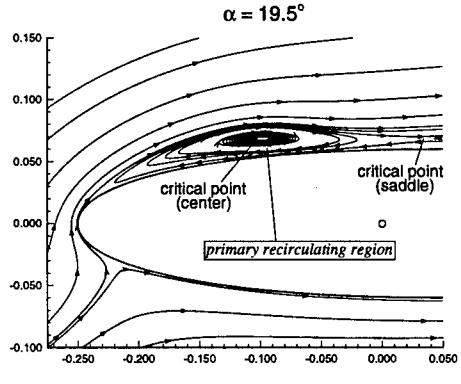

Figure 9: NACA0012 Pitching Airfoil, Explicit Computation, $Re_c = 10^4$, Streamlines, $\alpha = 19.5°$

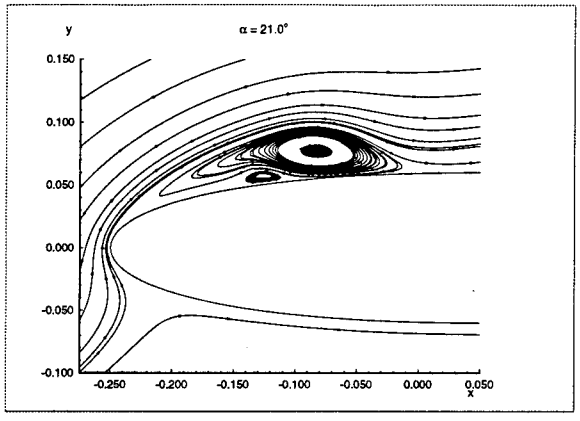

Figure 10: NACA0012 Pitching Airfoil, Implicit Computation, $Re_c = 10^4$, Streamlines, $\alpha = 21.5°$

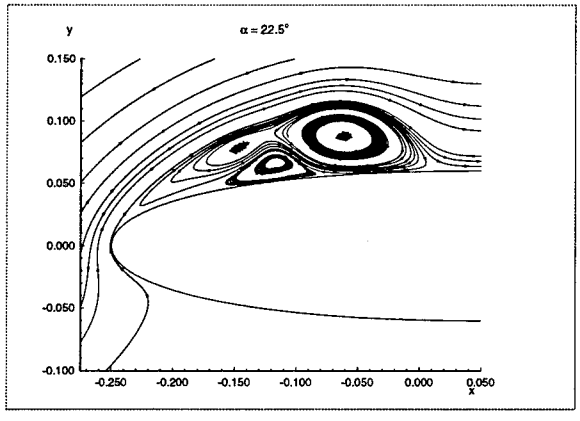

Figure 11: NACA0012 Pitching Airfoil, Implicit Computation, $Re_c = 10^4$, Streamlines, $\alpha = 22.5°$

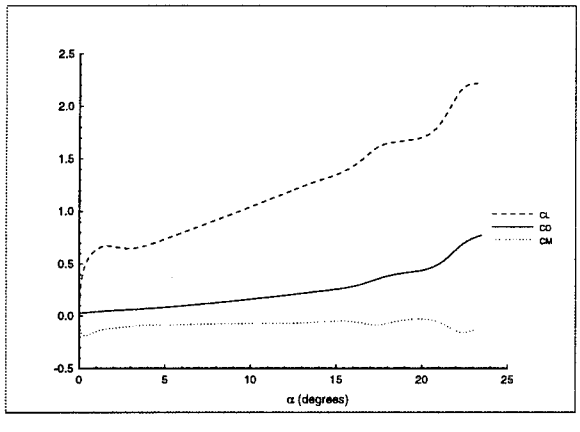

Figure 12: NACA0012 Pitching Airfoil, Explicit Computation, $Re_c = 2 \times 10^4$, Lift, Drag and Moment Coefficients

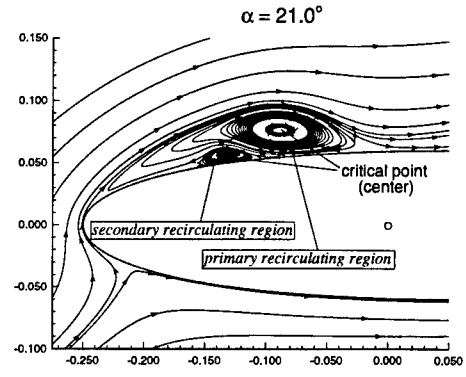

Figure 13: NACA0012 Pitching Airfoil, Explicit Computation, $Re_c = 10^4$, Streamlines, $\alpha = 21.5°$

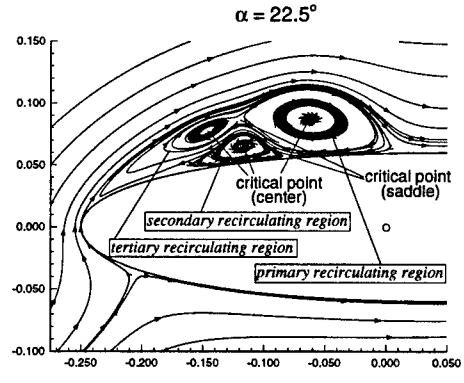

Figure 14: NACA0012 Pitching Airfoil, Explicit Computation, $Re_c = 10^4$, Streamlines, $\alpha = 22.5°$

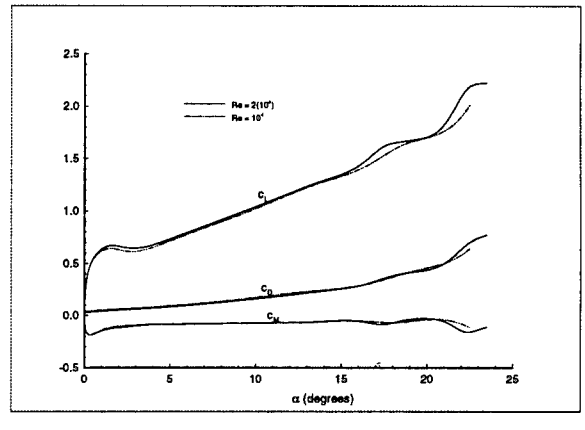

Figure 15: NACA0012 Pitching Airfoil Comparison of Lift, Drag and Moment Coefficients at $Re_c = 10^4$ and 2×10^4

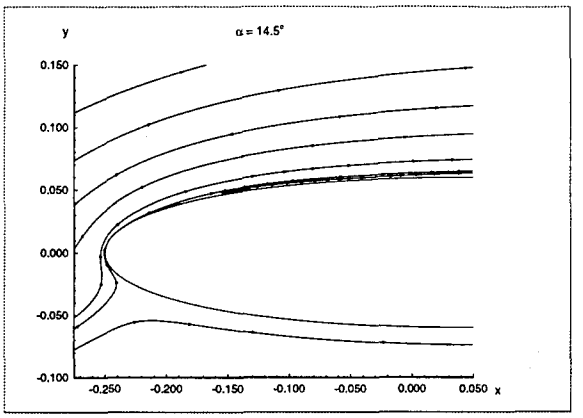

Figure 16: NACA0012 Pitching Airfoil, Implicit Computation, $Re_c = 2 \times 10^4$, Streamlines, $\alpha = 14.5°$

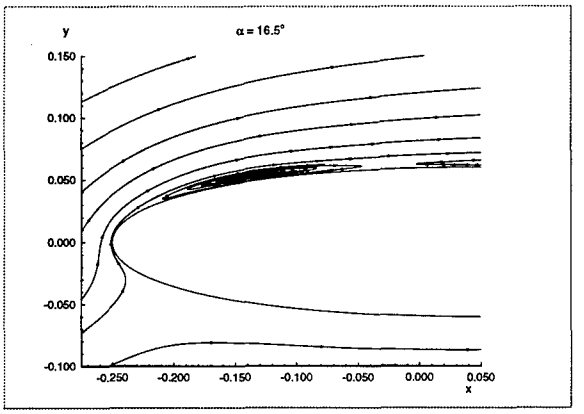

Figure 17: NACA0012 Pitching Airfoil, Implicit Computation, $Re_c = 2 \times 10^4$, Streamlines, $\alpha = 16.5°$

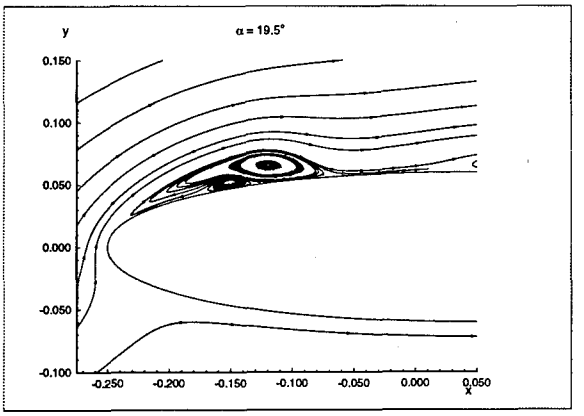

Figure 18: NACA0012 Pitching Airfoil, Implicit Computation, $Re_c = 2 \times 10^4$, Streamlines, $\alpha = 19.5°$

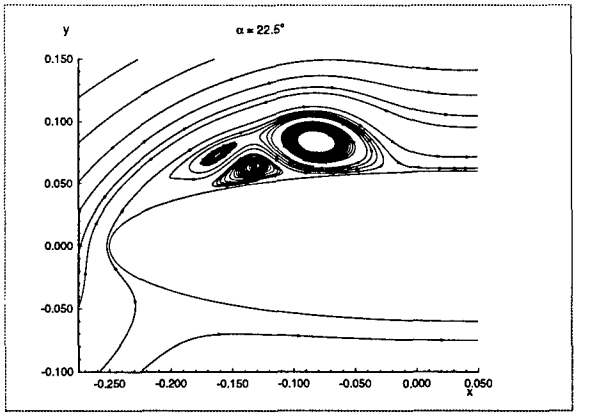

Figure 19: NACA0012 Pitching Airfoil, Implicit Computation, $Re_c = 2 \times 10^4$, Streamlines, $\alpha = 22.5°$

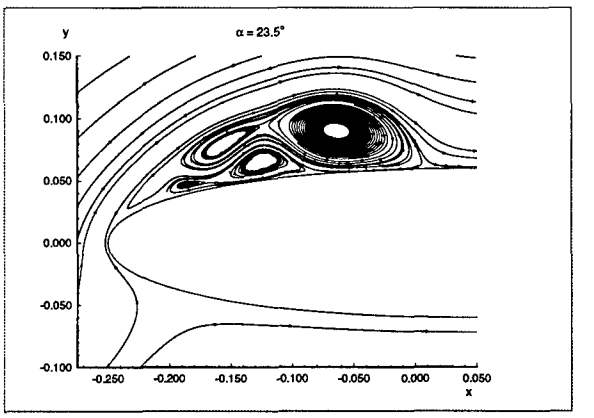

Figure 20: NACA0012 Pitching Airfoil, Implicit Computation, $Re_c = 2 \times 10^4$, Streamlines, $\alpha = 23.5°$